

DEVELOPMENT OF A FLUORESCENCE
CORRELATION SPECTROSCOPY METHOD FOR
THE STUDY OF BIOMOLECULAR INTERACTIONS

HWANG LING CHIN

(B.Sc.(Hons), NUS)

A THESIS SUBMITTED FOR THE DEGREE OF
DOCTOR OF PHILOSOPHY
DEPARTMENT OF CHEMISTRY
NATIONAL UNIVERSITY OF SINGAPORE

2006

This work was performed in the Department of Chemistry at the National University of Singapore (NUS), under the supervision of Dr. Thorsten Wohland, between July 2002 and August 2006, and in the Laboratoire d'Optique Biomédicale at the Ecole Polytechnique Fédérale de Lausanne (EPFL) under the supervision of Prof. Theo Lasser, between April 2004 and April 2005.

The results have been partly published in:

Hwang, L. C., and T. Wohland. 2004. Dual-color Fluorescence Cross-correlation Spectroscopy Using Single Laser Wavelength Excitation. *Chem. Phys. Chem.* 5:549–551.

Hwang, L. C., and T. Wohland. 2005. Single Wavelength Excitation Fluorescence Cross-correlation Spectroscopy with Spectrally Similar Fluorophores: Resolution for Binding Studies. *J. Chem. Phys.* 122: 114708 (1–11).

Hwang, L. C., M. Leutenegger, M. Gosch, T. Lasser, P. Rigler, W. Meier, and T. Wohland. 2006. Prism-based Multicolor Fluorescence Correlation Spectrometer. *Opt. Lett.* 31:1310–1312.

Hwang, L. C., M. Gösch, T. Lasser and T. Wohland. 2006. Simultaneous Multicolor Fluorescence Cross-Correlation Spectroscopy to Detect Higher Order Molecular Interactions Using Single Wavelength Laser Excitation. *Biophys. J.* 91:715-727

Acknowledgements

A doctoral thesis like this would not have been possible without the help of many people. I would like to acknowledge thanks to individuals who have contributed in one way or another in helping me complete this work.

I would like to thank my supervisor Dr. Thorsten Wohland for offering me this interesting project and supporting me throughout this research. His incredible patience, invaluable guidance and encouragement have greatly benefited me and this work. I am also thankful to Prof. Theo Lasser who supported me during the time I was a visiting PhD student in his laboratory. His discussions and suggestions relating to optics were of great help to my work.

I am grateful to all my colleagues from the Biophysical Fluorescence Laboratory in NUS. In particular, Yu Lanlan and Liu Ping who have provided me with assistance and comments relating to chemistry and biology. I am also grateful to my colleagues from the LOB, Michael Gösch for guidance and assistance in getting the optical components for this project; Marcel Leutenegger for his scientific discussions and proposals that have contributed to the prism setup; Per Rigler for his nanocontainers and discussions on FCS and chemistry; Ramachandra Rao, Kai Hassler and Jelena Mitic for their friendship and support; Adrian Bachmann, Antonio Lopez and Alexandre Serov for technical help; and Judith Chaubert for administrative support in Switzerland.

Last but not least, I would like to thank my parents and siblings for their love and concern; and my boyfriend Kang Yong for his understanding and support that have been indispensable over these years.

Table of Contents

Acknowledgements	ii
Summary	vi
List of Tables	viii
List of Figures	ix
List of Symbols	xi
1 Introduction	1
2 Theory and Setup	11
2.1 Fluorescence Correlation Spectroscopy	11
2.1.1 The autocorrelation function	11
2.1.2 Translational Diffusion	17
2.2 Fluorescence Cross-correlation Spectroscopy	19
2.2.1 The cross-correlation function	19
2.2.2 Fitting of models to the correlation data	24
2.2.3 Geometry of detection volumes	24
2.2.4 SW-FCCS Setup	25
3 Dual-color SW-FCCS	28
3.1 Introduction	28
3.2 Theory	29
3.3 Materials and Methods	31
3.4 Results and Discussion	32
3.4.1 Characterization of fluorophores	32
3.4.2 SW-FCCS experiments of streptavidin-biotin binding	37
3.5 Conclusion	42
4 Resolution of SW-FCCS	43
4.1 Introduction	43
4.2 Theory	44
4.2.1 Receptor-ligand complexes	44
4.2.2 The Cross-correlation function	48
4.2.3 The streptavidin-biotin receptor-ligand system	50
4.2.4 Calculations of SW-FCCS limits	52
4.3 Materials and Methods	53

4.4	Results and Discussion	54
4.4.1	Influence of the dissociation constant on SW-FCCS	55
4.4.2	Influence of impurities on SW-FCCS	55
4.4.3	Influence of cross-talk and quenching on SW-FCCS	57
4.4.4	Influence of receptor labeling on SW-FCCS	59
4.4.5	SW-FCCS with spectrally similar fluorophores on the streptavidin-biotin system	61
4.4.6	Comparison of sensitivities of different fluorophore pair systems	64
4.4.7	Possible fluorophore pairs for SW-FCCS	65
4.4.8	A comparison between FCS and SW-FCCS	66
4.5	Conclusion	67
5	Multicolor SW-FCCS	69
5.1	Introduction	69
5.2	Theory	70
5.2.1	Cross-correlation of triple species	70
5.2.2	Case 1: $R + L_g + L_y \rightarrow RL_g + L_y$	74
5.2.3	Case 2: $R + L_g + L_y \rightarrow RL_y + L_g$	75
5.2.4	Application of theory to streptavidin-biotin binding system	75
5.3	Materials and Methods	76
5.3.1	Optical setup	76
5.3.2	Chemistry	78
5.4	Results and Discussions	78
5.4.1	Characterization of fluorophores for SW-FCCS	78
5.4.2	Calibration experiments	83
5.4.3	Experimental results of streptavidin-biotin binding	84
5.4.4	Correlations of triple-color complexes	84
5.4.5	Fitting analysis of triple-color complexes	85
5.4.6	Correlations of complexes with alternate ligand binding	89
5.4.7	Fitting analysis of complexes with alternate ligand binding	92
5.4.8	Limitations of SW-FCCS	94
5.4.9	Simulations of cross-correlation amplitudes for different reaction models	95
5.4.10	Applications of multicolor SW-FCCS	104
5.5	Conclusion	108
6	Prism-based Fluorescence Correlation Spectrometer	110
6.1	Introduction	110
6.2	Materials and Methods	112
6.2.1	Prism spectrometer	112
6.2.2	Calibration with a single optic fiber	116
6.2.3	Calibration with an optic fiber array	117
6.2.4	Correlation experiments with fiber array	121
6.3	Results and Discussion	122
6.3.1	Correlation experiments	122
6.3.2	Design of prism spectrometer	123
6.4	Conclusions	125

6.5 Appendix: Zemax simulations	127
7 Conclusions and Outlook	129
Bibliography	135

Summary

The objective of this thesis was to develop a single laser wavelength fluorescence cross-correlation spectroscopy method (SW-FCCS) for the excitation of two or more fluorescent probes. The development and testing of the method was performed in different stages. The first part of the thesis, from chapters 2 to 4, describes the theory and optical setup of SW-FCCS. The experimental implementation was demonstrated with the receptor-ligand model of streptavidin-biotin. Different fluorophore assays including quantum dots, tandem dyes and organic dyes were tested on the system. The resolution limit of the SW-FCCS was evaluated with spectrally similar fluorophores. The second part of the thesis in chapters 5 and 6 extended the method to multicolor cross-correlation analysis with three detection channels. This was demonstrated first with conventional optical filter cascades and then with a dispersive prism for spectral separation. The SW-FCCS method simplifies the setup considerably without the need for aligning two laser beams or expensive laser systems for two-photon excitation.

Chapter 1 provides a literature review on single molecule fluorescence techniques relating to its applications in biomolecular interactions. The fluorophores and the receptor-ligand binding system used in this thesis were also reviewed.

Chapter 2 describes the theory and the experimental setup of FCS and dual-color SW-FCCS.

Chapter 3 investigates the feasibility of performing FCCS with a single laser excitation wavelength. Long Stokes shift fluorophores such as tandem dyes, quantum red and quantum dots were tested on the setup and the streptavidin-biotin

binding system was used as a proof-of-principle. Experimental cross-correlation functions were obtained and their amplitudes fitted with a bimolecular binding model. The fluorophore pair of quantum red/fluorescein produced a dissociation constant similar to the literature value whilst QD655/fluorescein had large errors due to aggregation problems.

Chapter 4 examines the limitations of the method for measuring dissociation constants with respect to various parameters such as cross-talk, quenching and sample impurities. A fluorophore pair consisting of common organic dyes, tetramethylrhodamine/fluorescein, having similar excitation and emission spectra, was experimented with the binding of streptavidin and biotin. Despite the lower signal-to-noise ratio compared with spectrally distinct fluorophore pairs, the method was able to determine the dissociation constant and stoichiometry of reaction.

Chapter 5 extends the SW-FCCS methodology to multicolor detection of three interacting molecular species. Three fluorescent probes fluorescein or R-phycoerythrin labeled biotin emits in the green or yellow channels respectively; Alexa 647-R-phycoerythrin labeled streptavidin (AXSA) emits in the red channel. Triple pair-wise cross-correlations between the three-color channels were performed and binding constants and stoichiometry of binding could be derived. Multicolor SW-FCCS delivers the possibility of detecting higher order molecular interactions and molecular assemblies using a single laser line.

Chapter 6 challenges the conventional FCCS setup by implementing a dispersive element in the detection path to chromatically disperse the emission light. The prism-based FCSpectrometer was first calibrated with fluorescein and AXSA with a single optic fiber and then tested for cross-correlations with biotinylated rhodamine green nanocontainers and AXSA using an optic fiber array. This novel wavelength tunable filter-free prism-based FCSpectrometer achieves simultaneous auto/cross-correlations and could be applied for multicolor detection.

List of Tables

3.1	Table of fluorescence yields of QR, QD655 and BF	34
4.1	Table of fluorescence intensities and yields of fluorescent molecules .	64
4.2	Maximum K_d/R_t values with corresponding L_t/R_t where the de- tection threshold $R = 1$	65
5.1	Molar extinction coefficients and fluorescence yields of BF, BPE and AXSA	79
5.2	Possible fluorophores and filter sets for SW-FCCS	82
5.3	Table of best fit values and limits of V_{eff} and K_d	89
6.1	Table of dispersion constants of prism material N-BK7 from Schott Catalog	115

List of Figures

2.1	The autocorrelation function and its changes with diffusion time and sample concentration	17
2.2	A typical fluorescence correlation spectroscopy optical setup	18
2.3	Foci geometry of two overlapping detection volumes	26
2.4	The dual-color single wavelength fluorescence cross-correlation spectroscopy setup	27
3.1	(A) Fluorescence emission spectra of QR, QD655 and BF. (B) Quenching of BF	33
3.2	Change of diffusion time and number of particles of QR with laser power	35
3.3	Schematic drawing of fluorescence intensity signal from the green and red detection volumes	36
3.4	Average count rate and intensity ratio of QR with varying laser power	37
3.5	Change of diffusion time and number of particles of QD655 and fluorescein with laser power	38
3.6	Cross-correlation function decrease in amplitude with increasing BF/QR concentration ratio	38
3.7	Plots of cross-correlation amplitude and number of particles versus BF/QR concentration ratio	40
3.8	Fitting of QR-BF binding curve and simulations of various K_d s	41
3.9	Fitting of QD655-BF binding curve and simulations of various K_d s	41
4.1	Binding experiments of BF to TMRSA	56
4.2	Influence of K_d on the cross-correlation amplitude	56
4.3	Influence of impurities on the cross-correlation amplitude	58
4.4	Influence of cross-talk on the cross-correlation amplitude	59
4.5	Sensitivity of SW-FCCS depending on cross-talk	60
4.6	Influence of receptor labeling on the cross-correlation amplitude	62
5.1	Multicolor SWFCCS optical setup	77
5.2	Absorbance, emission spectra and ACFs of BF, BPE and AXSA	80
5.3	Cross-correlation functions of binding between AXSA, BF and BPE	86
5.4	Triple pair-wise CCF amplitudes of the positive and negative controls of BF, BPE and AXSA binding	87
5.5	CCF amplitudes of with alternate binding of ligands BF, BPE to AXSA	91
5.6	Simulations of K_d influence on pair-wise CCF amplitudes	93

5.7	Simulations of $g \times y$ CCF amplitudes of positive and negative controls of BF, BPE and AXSA binding at different stoichiometries . . .	97
5.8	Simulations of triple pair-wise CCF amplitudes of the binding of 1 ligand A and 1 ligand B per receptor R	100
5.9	Simulations of $A \times B$ CCF amplitudes of ligands A and B binding per receptor R at different K_{ds} combinations	101
5.10	Simulations of $A \times B$ CCF amplitudes at different K_{ds} of RAB binding	102
5.11	Simulations of triple pair-wise CCF amplitudes of the binding of 2 ligands A and 1 ligand B per receptor R	105
5.12	Simulations of $A \times B$ CCF amplitudes of 2 ligands A and 1 ligand B binding per receptor R at different K_{ds} combinations	106
5.13	Simulations of $A \times B$ CCF amplitudes at different K_{ds} of RA_2B binding	107
6.1	Optical setup of the prism-based FCSpectrometer	113
6.2	Deviation of a ray through a prism	114
6.3	Dependence of angular dispersion and lateral displacement on wavelengths	116
6.4	Emission spectra of BF, RPE and AXSA and their ACFs measured on the FCSpectrometer	118
6.5	Schematic drawing of spots of different wavelengths imaged onto an optic fiber core	120
6.6	Calculated normalized transmission of optic fibers versus wavelength	122
6.7	ACFs and CCFs of the binding of biotinylated RhG nanocontainers and AXSA	124
6.8	Zemax software configurations for the design of the prism-based fluorescence correlation spectrometer.	127
6.9	Zemax simulation of the detection path of the prism-based FCSpectrometer	127
6.10	Zemax simulations of spot images produced by the prism-based FCSpectrometer	128
6.11	Wavelength input data for the Zemax simulations	128

List of Symbols

α	apex angle of prism
α_i	relative fluorescence yield
χ^2	Chi squared to describe goodness-of-fit
$\Delta\theta(\lambda)$	angular dispersion as a function of wavelength
$\delta C(\vec{r}, t)$	function of concentration fluctuations at positions \vec{r} and time t
$\Delta y(\lambda)$	lateral displacement as a function of wavelength
η	fluorescence yield of a molecule, product of Q and κ
η_{s}^{ij}	fluorescence yield of species s where $s = L, L_g, L_y, R, RL$ in detection channels ij where $i = j$ for ACF or $i \neq j$ for CCF
κ	detection efficiency of the optical instrument
λ_{ref}	reference wavelength
λ_{em}	emission wavelength
ρ	density of molecule
σ_i	standard deviation of data point i
τ	correlation time
τ_d	diffusion time
τ_{trip}	triplet lifetime
θ	deflection angle of light ray passing through prism
$C, \langle C \rangle$	concentration, average concentration
C_L, C_R, C_{RL}	time-dependent average concentrations of ligand, receptor and complex
$CEF(\vec{r})$	collection efficiency function
D	diffusion coefficient
f	focal length of optical lens

$f(r, r', \tau)$	concentration correlation function
$F_i(t), F_j(t), \delta F$	fluorescence signals in detector channels i and j as a function of time, fluorescence intensity fluctuations
f_{L_g}, f_{L_y}	probability of binding of green, yellow ligand
F_{trip}	fraction of molecules in triplet state
$G(\tau), G(0)$	correlation function, correlation function amplitude
$G_{\times}^+(0), G_{\times}^-(0)$	cross-correlation amplitude of the positive control, negative control, where \times can be $g \times r, y \times r$ or $g \times y$
$G_{\times}^-(0)$	cross-correlation function amplitude of the negative control
$I(\vec{r})$	intensity distribution function
J_1	Bessel function of the first kind of order 1
K	geometric ratio of axial to radial dimensions of the observation volume
k	Boltzmann's constant
$K_d, K_d^{max}, K_d^{min}$	dissociation constant, maximum and minimum dissociation constant
L, L_g, L_y	ligand, green ligand, yellow ligand
M	magnification of optical system
M	molecular mass
$MDF(\vec{r}), MDF$	molecule detection function
N, N_t	number of molecules, total number of molecules
n, n_t, n^*	number of binding ligands, total number of binding sites per receptor, number of bright ligands
N_A	Avogadro's number
n_g, n_y	number of green, yellow ligands
P	laser power
$p_L(u), p_R(v)$	probability of ligand or receptor to have u or v number of fluorophores, respectively
Q	product of the absorption coefficient and the molecular quantum yield of a fluorescent species
q_L, q_R	quenching factor of ligand or receptor
R	detection threshold

R	receptor
r, r', \vec{r}	radial coordinate, coordinate vector
RL, RL_n	receptor-ligand complex
$T(\lambda)$	transmission intensity as a function of wavelength
u, U	number of fluorophores attached to ligand, number of labeling sites on ligand
V	volume of spherical molecule
v, V	number of fluorophores attached to receptor, number of labeling sites on receptor
V_{eff}	effective observation volume
w_o	beam waist radius of laser beam
Y_i	mole fraction of molecular species i
z_o	distance along optical axis where the laser intensity has dropped to $1/e^2$ of its maximum
${}^*p_L, {}^\circ p_L, {}^*p_R, {}^\circ p_R$	probability of binding a bright (*) / dark (o) ligand or receptor
ACF	autocorrelation function
APC	allophycocyanine
APD	avalanche photodiodes
AXSA	Alexa Fluor 647-R-phycoerythrin-streptavidin
BF	biotin-fluorescein or biotin-4-fluorescein
BPE	R-phycoerythrin biotin-XX conjugate
CCD	charge-coupled device
CCF	cross-correlation function
CdSe	Cadmium Selenide
CHO	chinese hamster ovary
CLSM	confocal laser scanning microscopy
CMOS	charged metal-oxide semiconductor
cpm	count rates per molecule or counts per molecule and second
cw	continuous wave
Cy2, 5, 7	cyanine dye 2, 5 7

DNA	deoxyribonucleic acid
EGFR	epidermal growth factor receptor
FCCS	fluorescence cross-correlation spectroscopy
FCS	fluorescence correlation spectroscopy
FFS	fluorescence fluctuation spectroscopy
FIDA	fluorescence intensity distribution analysis
FILDA	fluorescence intensity lifetime distribution analysis
FIMDA	Fluorescence intensity multiple distribution analysis
FLIM	fluorescence lifetime imaging microscopy
FP	fluorescent protein
FRET	Förster resonance energy transfer
FWHM	full width half maximum
GFP	green fluorescent protein
HeLa	HeLa cell is an immortalized cell line. These are human epithelial cells from a fatal cervical carcinoma
Her2	Human epidermal growth factor receptor 2
ICCS	image cross-correlation spectroscopy
ICS	image correlation spectroscopy
mRFP	monomeric red fluorescent protein
NA	numerical aperture
NMR	nuclear magnetic resonance
PAID	photon arrival-time intensity distribution analysis
PBS	phosphate buffer solution
PCH	photon counting histogram
PCR	polymerase chain reaction
PE	phycoerythrin
PMT	photomultiplier tubes
PSF	point spread function
QD, QD655	quantum dots, quantum dot 655

QR	quantum red
RhG	rhodamine green
RICS	raster image correlation spectroscopy
RPE	R-phycoerythrin
SMD	single molecule detection
SPT	single particle tracking
SW-FCCS	single wavelength fluorescence cross-correlation spectroscopy
T	temperature
TIRF	total-internal-reflection fluorescence
TMR, TMRSA	tetramethylrhodamine dye, tetramethylrhodamine-labeled streptavidin
ZnS	Zinc Sulphide

Chapter 1

Introduction

Life is based on molecular processes that are essential for the structure and function of all living organisms. Biomolecular interactions between proteins, nucleic acids and small molecules are responsible for complex biological processes. By studying these biomolecular interactions, life scientists hope to better understand and predict cellular mechanisms and functions. Biochemists have made huge advances in protein sequencing and genomic analyses of living organisms, painting a network of interactions in a cell. But to resolve the underlying interactions involved in complex biological processes, it requires more than the identification with biochemical methods. With recent advances in single molecule techniques, it becomes possible to investigate the biomolecular interactions that give rise to higher order biological phenomena. This empowers biologists and biophysicists to study the mechanisms and functions in biological processes such as immune response, neurophysiological process and signal transduction.

Conventional ensemble techniques used for investigating biomolecular interactions include yeast two-hybrid screenings, immunoprecipitation and mass spectrometry. Structure determination methods such as X-ray crystallography and NMR provide additional information on binding sites and molecular conformation. However, these techniques used for analyzing nucleic acids and protein molecules require relatively large amounts and concentrations of sample. In addition, exper-

iments have to be performed occasionally under non-physiological conditions. In recent decades, the advancement of instrumentation have led to the emergence of biophysical techniques capable of probing single molecules on surfaces and solutions in real-time. By focusing on an individual molecule in space and time, such analyses provide quantitative information of force properties, conformational dynamics, molecular interactions and temporal changes with its microenvironment that could otherwise be hidden in ensemble experiments. Molecular dynamics can be studied without having to bring the ensemble population into a non-equilibrium state. Furthermore, because of the small measurement volume needed for sample assays, the high spatial resolution of single-molecule methods enables them to sort and examine rare molecular events or subpopulations that exist only in highly localized regions in the cell.

One type of approach to single molecule detection (SMD) techniques is the optical method based on fluorescence detection. Fluorescence techniques are non-invasive and non-destructive to samples. They can be performed in real-time at ambient or physiological temperatures. Their versatility with the molecular environment implies that they be applied *in vitro* or *in vivo*. By labeling the object of interest with a fluorophore and illuminating a small observation volume with a focused laser beam coupled with interference filters and sensitive detectors such as cooled charge-coupled device (CCD) cameras, photomultiplier tubes (PMT) or avalanche photodiodes (APD), the signal-to-noise ratio can be greatly increased over background scattering and cellular autofluorescence. Fluorescence microscopy techniques include epi-illumination wide-field imaging that has been applied in single particle tracking (SPT), confocal laser scanning microscopy (CLSM), total-internal-reflection fluorescence (TIRF), Förster resonance energy transfer (FRET) and fluorescence lifetime imaging microscopy (FLIM). Besides being able to visualize and monitor intracellular and membrane dynamics with precise spatial localization, protein-protein and protein-nucleic acid interactions can also be probed. Various SMD methods and its applications, in particular molecular interactions,

have been described in several reviews [1–7].

A widely used SMD method for measuring molecular interactions are FRET and FRET-based techniques such as FLIM. FRET process involves the resonance energy transfer between a single pair of donor and acceptor fluorophore with overlapping emission and excitation spectra respectively [8]. FRET efficiency depends on dipole-dipole interactions and molecular distance (inverse sixth power) and is used as a spectroscopic ruler on a scale of 1-10 nm [9]. Combining FRET and TIRF imaging, the dimerization and activation of EGFR on cell membranes were revealed [10]. Alternating laser excitation was used to improve signal-to-background ratio and to study the transcription mechanism by RNA polymerase [11, 12]. FLIM, on the other hand, measures the characteristic lifetime of a fluorophore (nanosecond range) [13, 14]. FRET-FLIM imaging observes the reduction of donor fluorescence lifetime as shown in the association of EGFR in live cells [15, 16]. However, a major disadvantage of FRET is the sensitivity to dye orientation, which may induce artefacts that may cause misinterpretations in molecular interactions.

Another group of fluorescence methods monitor the fluorescence intensity fluctuations of single molecules moving in and out of a confined illuminated volume. These methods known as fluorescence fluctuation spectroscopy (FFS) provide information that lie hidden in the fluctuating signal such as dynamic processes, chemical kinetics or molecular interactions [17]. Conventionally, correlation functions of the intensity fluctuations are calculated to give the number of particles and the average residence time spent in the detection volume. Recently, other methods have been developed based on the distribution of fluorescence intensity to extract information not measurable with correlation functions. Photon counting histogram (PCH) or fluorescence intensity distribution analysis (FIDA) have emerged at the same time from independent research groups to determine the fluorescence brightness parameter and distinguish different species according to their molecular brightness [18, 19]. FIDA has been applied in high throughput

screening to measure binding assays [20–22], and PCH has been used to probe ligand-protein binding [23] and protein oligomerization in live cells [24]. Extensions to PCH/FIDA include 2D-FIDA [25] and dual-color PCH [26] where two detectors monitor different emission polarization or emission wavelengths. Fluorescence intensity multiple distribution analysis (FIMDA) [27] and fluorescence intensity lifetime distribution analysis (FILDA) [28] combines the measurement of molecular brightness and diffusion time or fluorescence lifetime respectively. A multidimensional method known as photon arrival-time intensity distribution analysis (PAID) measures the photon arrival time intervals instead of counting photons at fixed time intervals. It was introduced to simultaneously extract diffusion time, molecular brightness and occupancy in multiple detection channels [29].

One of the first FFS methods to be introduced by Elson, Magde and Webb in the 1970s was fluorescence correlation spectroscopy (FCS) [30]. The theory was established to use intensity fluctuations of fluorescent particles diffusing through a focused laser beam, to characterize translational diffusion coefficients and chemical rate constants [31–34]. The improvement of this technique to single-molecule sensitivity was achieved by using a confocal microscope system with a high numerical aperture objective and single photon counting avalanche photodiodes as detectors [35, 36]. Since then, it has become an increasingly popular technique for the study of dynamics at thermodynamic equilibrium. Besides the ability to determine the concentration, diffusion characteristics [37], rotational diffusion [38–41] and various processes such as flow [42] and chemical reactions [43, 44], FCS has also been used to measure receptor-ligand interactions in solution and on cell membranes [45–47] and enzymatic turnovers [48]. Photodynamic properties of chemical dyes [49] and fluorescent proteins (FPs) [50, 51] have been studied and applied in the detection of pH changes in cells [52].

The concept of FCS is based on the correlation analysis of fluorescence fluctuations in a confined observation volume. The sensitivity of this technique to

detect binding of two or more components depends on the relative change in mass upon binding. For a multi-component system consisting of reactants and products labeled with the same fluorescent dye, the only way of differentiating the product from the reactant is when the product has a molecular mass that differs from the reactants by at least a factor of 4 [53]. This in turn shifts the correlation curve to higher diffusion times by at least a factor of 1.6 given by the Stokes-Einstein equation for spherical diffusing particles [54]. By separately labeling the reactants with differently emitting fluorophores, the labels can be simultaneously excited with two different laser lines and detected in separate channels. The signals from both detector channels are cross-correlated and the doubly labeled products can be easily distinguished from the singly labeled reactants independent of their mass. Earlier cross-correlation systems have made use of light scattering or a combination with fluorescence to measure their cross-correlation functions and determine rotational diffusion and association-dissociation kinetics [55, 56]. In dual-beam fluorescence cross-correlation spectroscopy, the setup consisting of two spatially separated focal points has been applied to characterize flow systems [57]. Although the concept of dual-color fluorescence cross-correlation spectroscopy (FCCS) has been proposed for biotechnological applications [58], it was first experimentally realized by Schwille et al. to measure nucleic acid hybridizations [59, 60]. The potential of this technique to effectively measure biomolecular interactions has expanded its applications to detecting PCR complexes [61, 62], monitoring enzyme kinetics [63, 64] and measuring protein-DNA interactions [65]. FCCS has been applied in live cell measurements (for reviews, see [66, 67]) to probe the endocytic pathway of bacterial cholera toxin labeled with Cy2 and Cy5 dyes on different subunits of the same holotoxin [68]. FP-based cross-correlation analysis in live cells have been recently reported where green fluorescent protein (GFP) was fused to monomeric red fluorescent protein (mRFP) with a caspase-3 recognition linker. Caspase-3 activation was detected through the decrease of the cross-correlation amplitude when the cells undergo apoptosis and protease cleavage [69]. Another *in vivo*

application of FCCS is the study of protein-protein interactions of transcription factors Fos and Jun fused with FPs [70]. ICS/ICCS is a variation of FCS/FCCS that rapidly captures a time-series of images with CLSM to determine the distribution and co-localization of biomolecules in live cells or cell membranes [71–73]. It is a very useful method to investigate motility of larger structures such as protein clusters. However, its temporal resolution is limited by the image acquisition time of the microscope [74, 75]. Raster image correlation spectroscopy (RICS) achieves the temporal resolution of FCS by rapidly measuring many focal points in the cell during the raster-scan mode of the CLSM [76].

The first dual-color fluorescence cross-correlation experiments on a single molecule level were performed with two lasers at different wavelengths [59]. Although this approach improves the detection sensitivity of interacting particles compared to FCS, the requirement of matching two laser beams to the same focal spot makes it experimentally challenging. The mismatch of laser excitation volumes also led others to develop new methods of aligning two laser beams to the same excitation volume using a prism [77] and alternative excitation methods using a multiline laser [78]. Two-photon excitation laser sources have been used to overcome the difficulty of aligning two laser beams to the same excitation volume and has recently found several applications in solution measurements of proteolytic cleavage [63]. Increased axial resolution from a more confined focal spot reduces background fluorescence and photobleaching making it suitable for *in vivo* studies [79, 80] such as intracellular calmodulin and calmodulin-kinase II binding [81, 82]. Recently, two-photon excitation has achieved the excitation of up to three dyes simultaneously to perform triple-color coincidence analysis [83]. However, the high cost of a high power femtosecond laser source and relatively lower emission rates, thus lower signal-to-noise ratio, limit its potential applications. Pulsed interleaved laser excitation [84] that is faster than the timescale of diffusion has been implemented to eliminate cross-talk for spectrally similar fluorescent proteins, e.g. CFP- and YFP-connexin fusion proteins in the membranes of live HeLa cells [85]. A less

expensive and simpler optical setup has been suggested. This involves a system of two or more fluorophores excited at the same wavelength but emit at distinctly separate emission wavelengths. However, till date, no adequate system has been proposed [64, 86]. With increasing demand for multiplex detection, the detection setup will become increasingly complex with more optical components integrated. Hence, a grating-based detection unit has been developed to replace the series of dichroic mirrors and bandpass filters, offering a wavelength tunable setup with multicolor detection [87]. Although commercial laser scanning microscopes can now be combined with FC(C)S for cell imaging and spectroscopy [88], the ability of the setup to perform multicolor cross-correlations will depend on the stability of alignment of several lasers to the same focal spot.

Fluorescent probes play an important role in distinguishing the target molecule from the background light such as scattering or autofluorescence. With the recent advent of long Stokes shift fluorophores such as quantum dots, tandem dyes and MegaStokes dyes [89], multicolor imaging using a single laser wavelength for excitation has been achieved with quantum dots [90]. Quantum dots are semiconductor nanocrystals made of Cadmium Selenide (CdSe) which has been coated with an additional semiconductor shell of Zinc Sulphide (ZnS) to improve the optical properties of the material. This core-shell material is further coated with a polymer shell [91] or other ligands [92] that allow the materials to be conjugated to biological molecules. Quantum dots have the unique optical property of size-dependent emission wavelengths [93]. Other benefits of quantum dots include long-term photostability, high quantum yield, multiple labeling with several colors, and single wavelength excitation for all colors. Quantum dot conjugates have found recent applications in live cell imaging of membrane receptors, Her2 and other cellular targets [94] and imaging in live animals [95]. Single molecule studies have also revealed blinking characteristics [96], longer fluorescence lifetimes [97], brightness and size properties [98]. Because of its long Stokes shift, multicolor FCS experiments have been performed to detect heterogeneities in lipid bilayer

membranes [99], combined with submicrometer fluidic channels for isolation and detection [100] and used to measure the binding constants of quantum dot-labeled streptavidin-biotin with two-photon excitation [101]. For extensive reviews of quantum dots on biological applications, see [102–104].

Phycobiliprotein-based tandem dyes have also been used for multicolor detection with single laser wavelength and were first applied in flow cytometry and cell sorting in fluorescence immunoassays [105]. As most clinical flow cytometers use only single laser excitation, there is a constant need for more fluorophores that can be simultaneously used to measure more than two parameters in a single cell. Phycobiliproteins, a class of light-harvesting proteins that enhances the efficiency of photosynthesis are found in many species of algae [106]. Phycobiliproteins have high extinction coefficients and quantum yields. The molecular sizes can be large, with R-phycoerythrin (RPE) at 240 kDa containing 34 bilin fluorophores but this does not seem to interfere with its experimental applications [105]. With its high molar absorption coefficient at a broad range of absorbance wavelengths between 470 and 550 nm, phycoerythrin (PE) can be coupled as an energy donor to a range of potential acceptor molecules, including Allophycocyanine (APC, $\lambda_{em} = 660$ nm) [106, 107], Cyanine dyes (Cy5, $\lambda_{em} = 670$ nm or Cy7, $\lambda_{em} = 767$ nm) [108] and Alexa Fluor dyes (Alexa Fluor 647, $\lambda_{em} = 667$ nm) [109]. When excited at an excitation wavelength of 488 nm, energy transfer of the tandem dyes produces large Stokes shifts with emission wavelengths that can be easily resolved from PE ($\lambda_{em} = 575$ nm) or fluorescein emission ($\lambda_{em} = 518$ nm) [110]. Three-color immunofluorescence analysis of cells was performed with flow cytometry [111] and this has since advanced to the capability of measuring up to 12 different colors [112]. The development of the tandem dyes has significantly enhanced the capabilities of single-laser excitation flow cytometers for performing multiparametric analysis and higher throughput screening, and can be extended to other single molecule applications, including multicolor fluorescence microscopy and spectroscopic techniques [113] such as FCS/FCCS.

The aim of this work is to develop a FCCS technique that uses only a single laser line for the excitation of multiple fluorescent probes. This method is called single wavelength fluorescence cross-correlation spectroscopy (SW-FCCS). Fluorophore assays including small organic dyes, quantum dots and tandem dyes are tested on the setup. As a proof-of-principle, model receptor-ligand binding system streptavidin-biotin is investigated for molecular interactions. Avidin is a tetrameric protein found in egg white and streptavidin is a similar protein (*Streptomyces avidinii*) isolated from a bacterium. The precise function of these proteins are still uncertain. However, the (strept)avidin-biotin binding complex is known to have the highest affinity interaction between a protein and ligand (dissociation constant $K_d = 10^{-15}$ M) [114, 115]. Streptavidin consists of four identical subunits, each arranged as a structure of eight-stranded, sequentially connected, antiparallel β sheets as determined by X-ray crystallography. A single vitamin biotin molecule binds in pockets at the ends of each of the β barrels, thus having a stoichiometry of streptavidin:biotin as 1:4. In the absence of biotin, the binding pocket contains five water molecules to maintain a defined structure. Upon binding of biotin, the bound water molecules are displaced by biotin and binding is induced by hydrogen bonding and van der Waals interactions and the ordering of two surface loops [116]. These structural and biochemical factors produce a high affinity binding and high activation energy for dissociation for the almost irreversible interaction of streptavidin-biotin [117]. The applications of the (strept)avidin-biotin system has been well-established in the life sciences in immunoassay and DNA probes [118, 119]. Recently, it has been extended to medical applications for localization and imaging of cancer cells, and biophysics where it has shown to be a standard model to test new techniques designed to study molecular interactions [120, 121]. Fluorimetric assays have been previously conducted for the quantification of avidin and streptavidin with biotin-fluorescein and biotin-4-fluorescein conjugates [122]. Binding of biotin-4-fluorescein to streptavidin was reported to be comparable to D-biotin in terms of high affinity, fast association and non-cooperative interaction

[123, 124]. Thus, streptavidin-biotin is an ideal candidate as a proof-of-principle for SW-FCCS to test for molecular interactions *in vitro* and whether this method is applicable to protein studies *in vivo*.

This thesis is structured into three sections:

Chapter 2 explains the theory and experimental setup of FCS and FCCS. The autocorrelation function is defined for a 3-dimensional Gaussian observation volume and for translational diffusion. The cross-correlation function is defined for interacting molecules under different conditions and the detection volumes described. The experimental setup for dual-color SW-FCCS is presented.

Chapters 3 and 4 describe the theory and experimental realization of dual-color SW-FCCS. As a proof-of-principle, the binding of biotin to streptavidin is tested and the resolution of binding is explored with different fluorophore assays. Chapter 3 presents SW-FCCS binding experiments on biotin and streptavidin labeled with fluorophores with widely separated emission wavelengths using long Stokes shift dyes, tandem dyes and quantum dots. In Chapter 4, the method is tested on standard organic dyes with similar emission wavelengths, fluorescein and tetramethylrhodamine. The resolution of SW-FCCS is determined and various factors such as binding constants, impurities, cross-talk and labeling ratios affecting the resolution are discussed.

Chapters 5 and 6 extend SW-FCCS to multicolor detection. Chapter 5 demonstrates the experimental setup of triple color detection using dichroic mirrors to separate the detection pathway into three different wavelength regions. In Chapter 6, a prism-based detection pathway coupled to an optic fiber array is demonstrated, achieving a filter-free and wavelength tunable fluorescence correlation spectrometer.

Finally, chapter 7 concludes and offers an outlook for future research of SW-FCCS. Related techniques that could potentially work on molecular interactions in live cells are also discussed.

Chapter 2

Theory and Setup

2.1 Fluorescence Correlation Spectroscopy

2.1.1 The autocorrelation function

In a FCS experiment, the fluorescence intensity is measured from an open probe volume in a sample which contains fluorescent particles of interest. The probe volume is usually given by a confocal arrangement that is defined by the focal volume of a focused laser beam and a pinhole. The pinhole spatially filters the emitted fluorescence light to ensure that only light from the focus is detected. A typical FCS setup for measurement of various molecular processes is depicted in Fig. 2.2. The fluorescence intensity shows characteristic fluctuations caused by molecular processes, thus containing information on their nature. The fluctuations might be due to processes that change the fluorescence quantum yield or absorption coefficient of the particles. For example, a molecule undergoing intersystem crossing into a triplet state or a cis-trans conformational change that renders the fluorophore non-fluorescent as long as it resides in this state [49, 125, 126]. They can also be produced by molecular motions such as translational diffusion that induce fluctuations in the number of fluorescent particles [37]. Fluctuations can also be caused by rotational diffusion where the alignment of molecular excitation and emission dipoles in respect to the excitation and the emission polarized detec-

tion is measured [38, 39, 41]. In order to obtain information about the underlying molecular processes, these fluctuations can be analyzed in terms of a fluorescence intensity correlation function that is given by Eq. 2.1 [30–32]. Fluorescence signals $F_i(t)$ and $F_j(t)$ in detector channels i and j are correlated according to the normalized correlation function as a function of time

$$G_{ij}(\tau) = \frac{\langle F_i(t) F_j(t + \tau) \rangle}{\langle F_i(t) \rangle \langle F_j(t) \rangle} \quad (2.1)$$

$$\begin{aligned} &= \frac{\langle F_i(0) F_j(\tau) \rangle}{\langle F_i \rangle \langle F_j \rangle} \\ &= \frac{\langle (\langle F_i \rangle + \delta F_i(0)) (\langle F_j \rangle + \delta F_j(\tau)) \rangle}{\langle F_i \rangle \langle F_j \rangle} \\ &= \frac{\langle \delta F_i(0) \delta F_j(\tau) \rangle}{\langle F_i \rangle \langle F_j \rangle} + 1 \end{aligned} \quad (2.2)$$

where $i = j$ for autocorrelation of a single detector channel and $i \neq j$ for cross-correlation of two channels. δF denotes fluorescence fluctuations about the average value $\langle F \rangle$ where τ is the correlation time and the angular brackets $\langle \rangle$ indicate averaging over time. The transition from the first line of the right hand side in Eq. 2.1 to the second line is possible because it is assumed that the observed processes are stationary and ergodic, which means that their statistical properties and thermodynamic ensemble are time-invariant. It can be shown that the intensity correlation function (Eq. 2.1) and the fluctuation correlation function (Eq. 2.2) differs by a constant of 1. In this thesis, only the intensity correlation function will be used as the intensity signal can be directly measured to calculate the autocorrelation function (ACF) or the cross-correlation function (CCF). On the other hand, the fluctuation correlation function requires the calculation of the intensity time average before calculating the correlation functions.

The fluorescence intensity fluctuation from a small illuminated probe volume can be written as

$$\delta F(t) = \kappa Q \int I(\vec{r}) CEF(\vec{r}) \delta C(\vec{r}, t) d\vec{r} \quad (2.3)$$

Here, Q is the product of the absorption coefficient and the molecular quantum yield of the fluorescent species. κ is the detection efficiency of the instrument including the detector. $I(\vec{r})$ is the spatial intensity profile of the excitation light and $CEF(\vec{r})$ is the collection efficiency function that characterizes the spatial filtering effect of the pinhole on the point spread function (PSF). The PSF of the optical system describes the intensity distribution of the image of a point emitter [35, 36]. $\delta C(\vec{r}, t)$ is the fluctuation of molecule concentrations at positions \vec{r} and time t due to Brownian motion. The product of $I(\vec{r})$ and $CEF(\vec{r})$ gives the molecule detection function $MDF(\vec{r})$ that determines the spatial distribution of the effective sample volume. The MDF depends on the intensity distribution of the focused laser illumination and the efficiency of photons detected from a fluorescent molecule. The factors κ and Q can be combined to a fluorescence yield parameter η that is determined by the photon counts per molecule and second. Eq. 2.3 and $\langle F \rangle$ can then be rewritten as

$$\delta F(t) = \int \eta MDF(\vec{r}) \delta C(\vec{r}, t) d\vec{r} \quad (2.4)$$

$$\langle F \rangle = \eta \langle C \rangle \int MDF(\vec{r}) d\vec{r} \quad (2.5)$$

Using Eqs. 2.4 and 2.5 in Eq. 2.2, the normalized fluctuation correlation function of one species is given by the following equation where the constant 1 is excluded

$$G(\tau) = \frac{\int \int \eta^2 MDF(\vec{r}) MDF(\vec{r}') f(r, r', \tau) d\vec{r} d\vec{r}'}{(\langle C \rangle \int \eta MDF(\vec{r}) d\vec{r})^2} \quad (2.6)$$

$\langle C \rangle$ is the mean concentration of molecules and $f(r, r', \tau)$ is the concentration correlation function assuming that the sample is stationary.

$$f(r, r', \tau) = \delta C(\vec{r}, 0) \delta C(\vec{r}', \tau) \quad (2.7)$$

When $\tau = 0$, the concentration fluctuations are correlated at the same time and position for non-interacting fluorescent molecules. The concentration correlation

function can then be described by the product of a Dirac delta function, $\delta ()$ and the mean square fluctuation of C (Poisson statistics of mean square fluctuation of C is $\langle C \rangle$)

$$f(r, r', 0) = \langle C \rangle \delta(r - r') \quad (2.8)$$

Substituting Eq. 2.8 in Eq. 2.6 gives

$$G(0) = \frac{1}{\langle C \rangle} \frac{\int MDF(\vec{r})^2 d\vec{r}}{(\int MDF(\vec{r}) d\vec{r})^2} \quad (2.9)$$

where the effective observation volume V_{eff} is defined as

$$V_{eff} = \frac{(\int MDF(\vec{r}) d\vec{r})^2}{\int MDF(\vec{r})^2 d\vec{r}} \quad (2.10)$$

In a confocal setup with diffraction-limited illumination and detection, the PSF is described by Bessel functions while for an underfilled objective back aperture, it is approximated as a Gaussian-Gaussian-Lorentzian (x, y, z) intensity profile. The PSF of a microscope objective is then convoluted with the circular pinhole function to give $MDF(\vec{r}) = I(\vec{r}) CEF(\vec{r})$, and the MDF is approximated to be a 3D-Gaussian illumination intensity profile

$$MDF(\vec{r}) = I_o \exp(-2r^2/w_o^2) \exp(-z^2/z_o^2) \quad (2.11)$$

$I_o = 2P/(\pi w_o^2)$ is the excitation intensity at the center of the laser beam waist with laser power P . z is the distance along the axial direction from the focal plane and z_o is where the intensity has dropped to $1/e^2$ from its highest intensity in the center of focus. w_o is the diffraction-limited beam waist radius at $z = 0$ given by [127]

$$w_o = \frac{0.61\lambda}{NA} \quad (2.12)$$

where NA is the numerical aperture of the microscope objective and λ is the excitation wavelength. The effective observation volume in Eq. 2.10 is then integrated

over the whole space to give $V_{eff} = \pi^{3/2} w_0^2 z_0$. At $\tau = 0$, the amplitude of the correlation function is equal to the inverse of the average number of molecules in the observation volume

$$G(0) = \frac{1}{V_{eff} \langle C \rangle} = \frac{1}{\langle N \rangle} \quad (2.13)$$

The number of photons fluctuates according to Poisson statistics, where the variance equals the average number of molecules $\langle \delta N^2 \rangle = \langle N \rangle$.

For translational diffusion, the concentration correlation function with diffusion coefficient D is derived to give the following expression [32, 34, 128]

$$f(r, r', \tau) = \frac{1}{(4\pi D\tau)^{3/2}} \exp\left(-\frac{|\vec{r} - \vec{r}'|^2}{4D\tau}\right) \quad (2.14)$$

It describes the probability of finding a diffusing molecule inside the observation volume at position r' and time τ when it was at position r at time 0. Inserting Eq. 2.14 back into Eq. 2.6 and using Eq. 2.10 for the observation volume, the ACF for 3D translational diffusion of a single species is

$$G(\tau) = \frac{1}{\langle N \rangle} \left(1 + \frac{\tau}{\tau_d}\right)^{-1} \left(1 + \frac{\tau}{K^2 \tau_d}\right)^{-1/2} \quad (2.15)$$

$$\tau_d = \frac{w_0^2}{4D} \quad (2.16)$$

τ_d from the first term defines the diffusion time of the molecular species in xy-direction. The second term represents the diffusion in z-direction where $K = z_0/w_0$ is the geometric ratio of axial to radial dimensions of the observation volume. If translational diffusion occurs only in 2D such as on surfaces or cell membranes, Eq. 2.15 will have only the first term of diffusion.

Fluorescence emission is proportional to the laser excitation at low laser intensities. At high intensities, the fluorescence emission reaches optical saturation and enlarges the MDF [129]. Saturation of the dye is due to the limitation of emitting 1 photon per excited state being populated. Given that the lifetime of the excited singlet state is in the range of few nanoseconds, the maximum photon count rate

is 10^8 Hz. Thus, under high laser excitation intensities, the excited singlet state becomes highly populated and there is a higher probability for the transition from the excited singlet state to the lowest triplet state. This is followed by relaxation into the ground state. This non-radiative and slower transition has a triplet lifetime $\tau_{trip} \sim \mu\text{s}$ and can be distinguished from the diffusion times of dye molecules τ_d from tens of μs to ms. This triplet state kinetics when inserted into Eq. 2.15 gives [125, 126]

$$G(\tau) = \frac{1}{\langle N \rangle} [1 - F_{trip} + F_{trip} \exp(-\tau/\tau_{trip})] \left(1 + \frac{\tau}{\tau_d}\right)^{-1} \left(1 + \frac{\tau}{K^2\tau_d}\right)^{-1/2} \quad (2.17)$$

where F_{trip} is the fraction of particles in the triplet state and $\langle N \rangle$ is the number of particles in the singlet state. To determine directly the total number of particles N_t in the singlet and triplet states, $\langle N \rangle$ has to be replaced with $N_t(1 - F_{trip})$. If multiple species are present, Eqs. 2.15 or 2.17 has to be extended to include different quantum yields [37]

$$G(\tau) = \frac{\sum_i \alpha_i^2 Y_i \langle N_i \rangle}{[\sum_i \alpha_i Y_i \langle N_i \rangle]^2} \left(1 + \frac{\tau}{\tau_{di}}\right)^{-1} \left(1 + \frac{\tau}{K^2\tau_{di}}\right)^{-1/2} \quad (2.18)$$

Here $\alpha_i = \eta_i/\eta_1$ is the relative fluorescence yield and Y_i is the mole fraction of molecular species i . Fig. 2.1 shows simulations of a 1-component diffusion ACF with triplet-state and ACFs with different diffusion coefficients and sample concentrations. The ACFs are shown to converge to a value of $G(\tau) = 1$ toward long correlation times, indicating that the initial and current signal is no longer correlated.

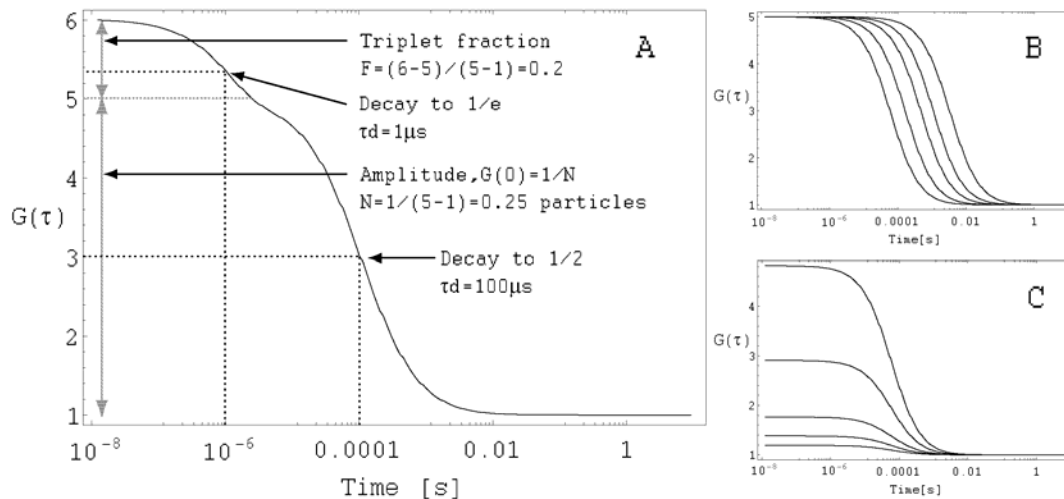


Figure 2.1: (A) Autocorrelation function of one-component diffusion with triplet state dynamics. Explanation of parameters are shown in graph. (B) Autocorrelation functions for different diffusion coefficients. The curves shift towards longer times with smaller diffusion coefficients. From left to right: 2.8×10^{-6} , 1×10^{-6} , 3.5×10^{-7} , 1.5×10^{-7} , $5 \times 10^{-8} \text{ cm}^2/\text{s}$. (C) Autocorrelation functions for different sample concentrations corresponding to number of particles. Amplitudes of functions are inversely related to number of particles in the observation volume. From top to bottom: 1, 2, 5, 10, 20 nM, equivalent to the number of particles: 0.26, 0.52, 1.31, 2.62, 5.24.

2.1.2 Translational Diffusion

The translational diffusion of a molecule in a viscous medium is defined by Brownian motion, given by the Stokes-Einstein equation [54]

$$D = \frac{kT}{f} \quad (2.19)$$

where the diffusion coefficient of the molecule D depends on Boltzmann's constant k , the absolute temperature T and the friction coefficient f . For the case of a spherical molecule,

$$f = 6\pi\eta r \quad (2.20)$$

where η is the viscosity of the solvent, and r is the radius of the sphere. r is related to the mass of a sphere given by the product of the density ρ and volume V .

$$M = \rho V = \rho \frac{4}{3} \pi r^3 \quad (2.21)$$

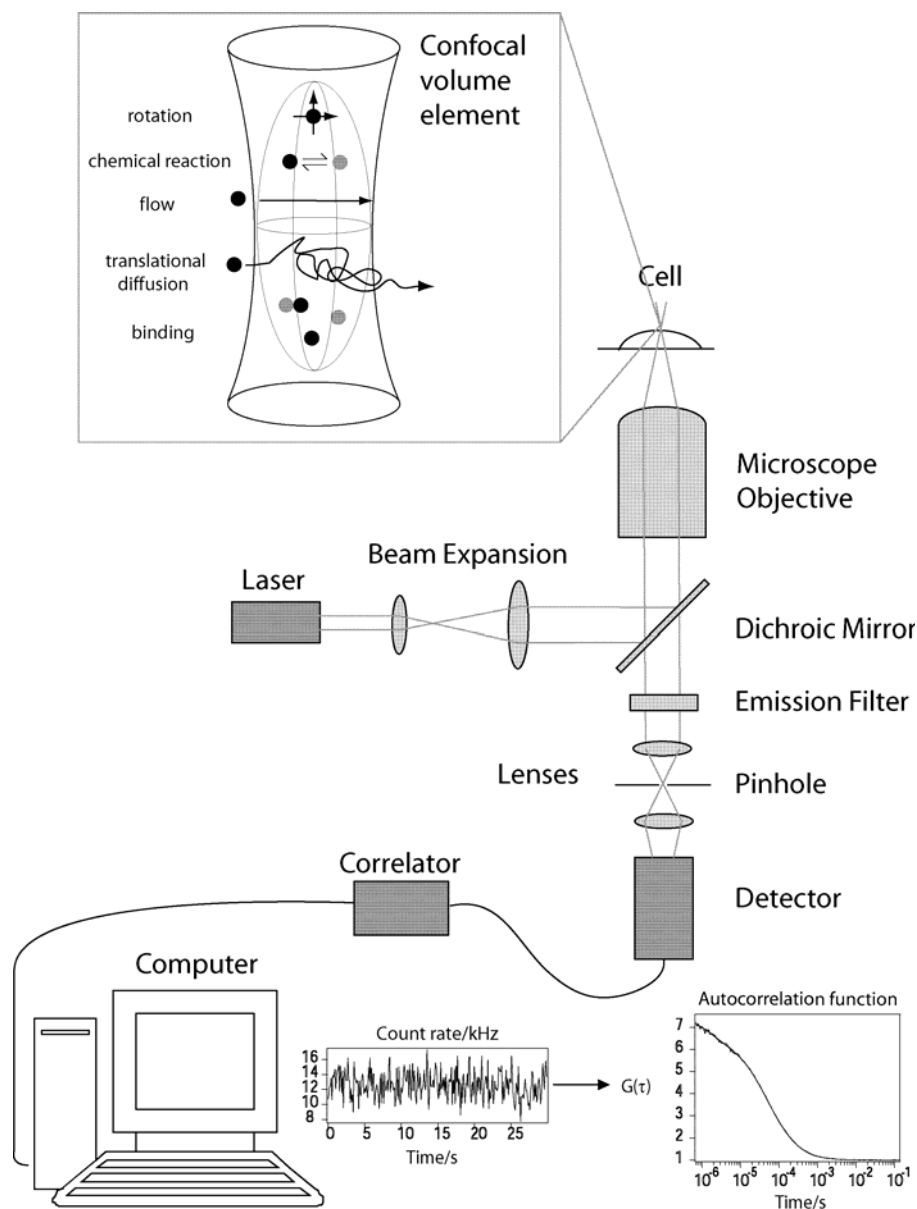


Figure 2.2: A typical optical setup of FCS is shown. A laser beam is expanded and focused by a microscope objective and into a fluorescent sample. The emitted fluorescence light coming from the small detection volume is separated from excitation light by a dichroic mirror. Out-of-focus light is spatially filtered by a pinhole at the conjugate plane. The emission light is focused by a lens onto a detector e.g. avalanche photodiode (APD). The APD counts the incoming photons and sends a TTL pulse for each photon to the hardware correlator. The correlator counts the photons in increasing time lags and calculates the autocorrelation function online in a semilogarithmic time scale that is displayed on a computer. The autocorrelation function reveals processes that cause the fluorescence fluctuations as the molecule diffuses through the confocal volume element. Examples of such processes are rotational diffusion, chemical reactions, flow and translational diffusion and binding or molecular interactions (inset).

Therefore, the diffusion coefficient is inversely proportional to the cube root of the molecular mass M of the species

$$D \sim \frac{1}{\sqrt[3]{M}} \quad (2.22)$$

$$\tau_d \sim \sqrt[3]{M} \quad (2.23)$$

Using a reference fluorophore sample for calibration with a known diffusion coefficient such as Rhodamine 6G ($D_{Rho} = 2.8 \times 10^{-6} \text{ cm}^2/\text{s}$) [36], the D_i values of all other fluorescent dyes can be determined from Eq. 2.16 by

$$D_i = \frac{\tau_{Rho}}{\tau_{di}} D_{Rho} \quad (2.24)$$

The capability of FCS to detect binding of two or more components depends on the relative change in mass upon binding. For a multi-component system consisting of reactants and products labeled with the same fluorescent dye, the only way of differentiating the product from the reactant is when the product has a molecular mass that differs from the reactants by a factor of at least 4–8. This in turn shifts the correlation curve to longer diffusion times by at least a factor of 1.6–2 (see Eq. 2.19) for spherical diffusing particles [53]. Therefore, FCS is not able to resolve binding molecules with similar masses. But by separately labeling the reactants with fluorophores of different emission characteristics, two labeled molecules can be simultaneously excited with two different laser lines and detected in separate channels for cross-correlation analysis.

2.2 Fluorescence Cross-correlation Spectroscopy

2.2.1 The cross-correlation function

The first experimental realization of dual-color fluorescence cross-correlation with spectrally different dyes was demonstrated by Schwille et al. [59]. It was per-

formed on Cy5 and Rhodamine green (RhG)-labeled complementary DNA oligonucleotides that hybridize irreversibly. The double-stranded hybrid produces positive cross-correlation signals while the ACF of each color contains signals from both the hybrid and the single strands. Two different wavelength laser beams that emit at the dyes' absorbance maxima were aligned to the same illumination focal volume for excitation. When the concentrations of reactants are constant, the amplitude of the CCF is then directly proportional to the concentration of the dual-color complexes formed. This easily distinguishes the products from the free reactants via the amplitude of the CCF, as compared to the weak dependence of the ACF with the mass of the complexes. Assuming that there is no cross-talk between both detectors, the general theory of CCF is shown below in Case 1.

In this thesis, a single laser line is used for the excitation of two to three differently labeled molecules. This is possible by using fluorophores that have spectrally distinct emission but similar excitation wavelengths. Examples of such dyes include organic dyes, quantum dots, tandem dyes and MegaStokes dyes [89] (see chapter 5, Table 5.2). The percentage of emission cross-talk in other detector channels depends on the laser excitation intensity, emission spectra of the dyes and the emission bandpass filters. In the experiments of Schwille and co-workers, they had to take into account the detector cross-talk of different dyes excited by both lasers. Here, because there is only one laser used for the simultaneous excitation of different dyes, Case 2 describes the theory with detector cross-talk induced by the same laser.

Experimentally, fluorescence fluctuations can arise from other processes besides diffusion. Photodynamic processes such as single-triplet state transition, cis-trans isomerization or protonation of fluorescent proteins. These photophysical processes create additional exponential decays in the ACF. However, because the fluctuation signals of these processes in different channels are not correlated, they do not appear in the CCF except when it is due to cross-talk. Here, the assumption is made that there is no attractive or repulsive interactions between

particles and no internal dynamic processes take place. The only fluctuation correlation terms are $\langle \delta C_i(\vec{r}, 0) \delta C_j(\vec{r}', \tau) \rangle$, i.e. the diffusional process for pair-wise interacting molecules.

Case 1: For an interacting system of two molecular species 1 and 2, with ideally separated detection signals.

The two detector signals are

$$\delta F_1(t) = \int MDF_1(\vec{r}) \eta_1 [\delta C_1(\vec{r}, t) + \delta C_{12}(\vec{r}, t)] \delta \vec{r} \quad (2.25)$$

$$\delta F_2(t) = \int MDF_2(\vec{r}) \eta_2 [\delta C_2(\vec{r}, t) + \delta C_{12}(\vec{r}, t)] \delta \vec{r} \quad (2.26)$$

Let the 3D diffusional component be

$$g(\tau) = \left(1 + \frac{\tau}{\tau_d}\right)^{-1} \left(1 + \frac{\tau}{K^2 \tau_d}\right)^{-1/2} \quad (2.27)$$

Inserting Eqs. 2.25 and 2.26 into Eq. 2.2 with $i = 1, 2$ and assuming a 3D Gaussian distribution for V_{eff} , the ACF and the CCF become

$$G_i(\tau) = \frac{1}{V_{eff,i}} \frac{(\langle C_i \rangle g_i(\tau) + \langle C_{12} \rangle g_{12}(\tau))}{(\langle C_i \rangle + \langle C_{12} \rangle)^2} \quad (2.28)$$

$$G_{12}(\tau) = \frac{1}{V_{eff,12}} \frac{\langle C_{12} \rangle g_{12}(\tau)}{(\langle C_1 \rangle + \langle C_{12} \rangle)(\langle C_2 \rangle + \langle C_{12} \rangle)} \quad (2.29)$$

From the above equations, it is clear that the complex species 12 can be distinguished from the rest of the free molecules by cross-correlation. $G(\tau \rightarrow 0)$ gives the amplitudes of ACF and CCF when $g(0) = 1$. The total number of molecular species 1 or 2 is then the inverse of $G_i(0)$. The amplitudes of the ACF and CCF are given by

$$G_i(0) = \frac{1}{V_{eff,i}} \frac{1}{\langle C_i \rangle + \langle C_{12} \rangle} \quad (2.30)$$

$$G_{12}(0) = \frac{1}{V_{eff,12}} \frac{\langle C_{12} \rangle}{(\langle C_1 \rangle + \langle C_{12} \rangle)(\langle C_2 \rangle + \langle C_{12} \rangle)} \quad (2.31)$$

In slow kinetic binding studies of fluorescent molecules 1 and 2, the denominator of Eq. 2.31 remains the same, as the sum of all reacting species remain constant in time. $G_{12}(0)$ is then directly proportional to the numerator. By using $G_1(0)$ and $G_2(0)$ from Eq. 2.30 and putting them in Eq. 2.31, the concentration of the complex is derived as [59]

$$\langle C_{12} \rangle = \frac{V_{eff,12} G_{12}(0)}{V_{eff,1} G_1(0) V_{eff,2} G_2(0)} \quad (2.32)$$

However, in the case where the binding assay is measured at binding equilibrium, different concentrations of the reactants are used to determine the dissociation constant. From Eq. 2.31, the CCF amplitude is inversely proportional to the concentration of reactants while the complex contributes to the numerator. Thus, $G_{12}(0)$ will no longer be directly proportional to the concentration of the complex but will depend on the amount of reactants and complexes both present in the sample mixture. For cross-correlation analysis of a system measured at binding equilibrium, see chapters 3–5.

Case 2: For an interacting system of two molecular species 1 and 2, with detector cross-talk.

Species 1 or 2 has the maximum fluorescence emission in detector 1 or 2 respectively. Since there is only one laser line used for the excitation of two different species, all possible cross-talk of reactant and product species in the two detectors is taken into account. The fluorescence signal in detector i is

$$\delta F_i(t) = \int MDF_i(\vec{r}) [\eta_{1i} \delta C_1(\vec{r}, t) + \eta_{2i} \delta C_2(\vec{r}, t) + (\eta_{1i} + \eta_{2i}) \delta C_{12}(\vec{r}, t)] \delta \vec{r} \quad (2.33)$$

Inserting the signal from both detectors into Eq. 2.2 and focusing only on their amplitudes, the ACF and CCF become

$$G_i(0) = \frac{1}{V_{eff,i}} \frac{\eta_{1i}^2 \langle C_1 \rangle + \eta_{2i}^2 \langle C_2 \rangle + (\eta_{1i} + \eta_{2i})^2 \langle C_{12} \rangle}{(\eta_{1i} \langle C_1 \rangle + \eta_{2i} \langle C_2 \rangle + (\eta_{1i} + \eta_{2i}) \langle C_{12} \rangle)^2} \quad (2.34)$$

$$G_{12}(0) = \frac{1}{V_{eff,12}} \frac{\eta_{11}\eta_{12}\langle C_1 \rangle + \eta_{21}\eta_{22}\langle C_2 \rangle + (\eta_{11} + \eta_{21})(\eta_{12} + \eta_{22})\langle C_{12} \rangle}{\left[\begin{array}{l} (\eta_{11}\langle C_1 \rangle + \eta_{21}\langle C_2 \rangle + (\eta_{11} + \eta_{21})\langle C_{12} \rangle) \times \\ (\eta_{12}\langle C_1 \rangle + \eta_{22}\langle C_2 \rangle + (\eta_{12} + \eta_{22})\langle C_{12} \rangle) \end{array} \right]} \quad (2.35)$$

η_{12} is the fluorescence yield of molecular species 1 emitting in detector channel 2. From Eq. 2.35, it can be seen that $G_{12}(0)$ is now also dependent on the product of the fluorescence yields of the species in each channel. Therefore, to yield an improvement of dual-color cross-correlation over autocorrelation, where both species are labeled with the same color and the product is double the fluorescence yield, the ratio of dual-color complex to single-color complex has to be bigger than 4 [59]. This means that the dual-color complex is contributing to the CCF 4 times more than the single-color complex to the ACF. This is due to the square dependence of the ACF on η shown in the numerator of the above equations.

$$\frac{(\eta_{11} + \eta_{21})(\eta_{12} + \eta_{22})}{\eta_{11}\eta_{12}} = \frac{\eta_{C1}\eta_{C2}}{\eta_{11}\eta_{12}} > 4 \quad (2.36)$$

Case 3: For an interacting system of two molecular species 1 and 2, with detector cross-talk and change in fluorescence yield.

The change in fluorescence yield η may be caused by photophysical processes such as photobleaching, quenching, shifting of emission wavelengths or Förster resonance energy transfer (FRET). The quantum yield of a fluorophore is sometimes changed in the bound state due to altered local chemical environments. Quenching refers to any process that causes a reduction in the quantum yield of a given fluorescence process. Quenching can be either static or collisional [130] and can occur through molecular rearrangement of the labeled molecules. In the case of FRET, there is a loss of fluorescence intensity for the donor fluorophore but an increase in intensity in the acceptor fluorophore. The changes in fluorescence yields upon binding can be taken into account by including a factor q in the correlation function amplitudes

$$\eta'_{Ci} = q_1\eta_{1i} + q_2\eta_{2i} \quad (2.37)$$

$$G_i(0) = \frac{1}{V_{eff,i}} \frac{\eta_{1i}^2 \langle C_1 \rangle + \eta_{2i}^2 \langle C_2 \rangle + \eta_{Ci}^2 \langle C_{12} \rangle}{(\eta_{1i} \langle C_1 \rangle + \eta_{2i} \langle C_2 \rangle + \eta'_{Ci} \langle C_{12} \rangle)^2} \quad (2.38)$$

$$G_{12}(0) = \frac{1}{V_{eff,12}} \frac{\eta_{11}\eta_{12} \langle C_1 \rangle + \eta_{21}\eta_{22} \langle C_2 \rangle + \eta'_{C1}\eta'_{C2} \langle C_{12} \rangle}{\left[\begin{array}{l} (\eta_{11} \langle C_1 \rangle + \eta_{21} \langle C_2 \rangle + \eta'_{C1} \langle C_{12} \rangle) \times \\ (\eta_{12} \langle C_1 \rangle + \eta_{22} \langle C_2 \rangle + \eta'_{C2} \langle C_{12} \rangle) \end{array} \right]} \quad (2.39)$$

2.2.2 Fitting of models to the correlation data

Correlation data analysis was performed by fitting the raw data points with a defined correlation function model such as a 1-component, 3D-diffusion model (Eq. 2.15) or a 1-component, 3D-diffusion with triplet model (Eq. 2.17). The raw data was fitted using the software program Igor Pro (Wavemetrics, Portland, OR) that performs an iterative procedure by the Levenberg-Marquardt algorithm to minimize the χ^2 . The χ^2 measures the summation of all differences between the fitted function y against the raw data y_i and is weighted by its standard deviation, σ_i [131]

$$\chi^2 = \sum \left[\frac{(y - y_i)}{\sigma_i} \right]^2 \quad (2.40)$$

For fittings of cross-correlation amplitudes (in chapters 3–5), the software package Mathematica 5.0 (Wolfram Research Inc., Champaign, IL) was used to model the changes of CCF amplitudes with ligand/receptor concentration ratio to obtain the minimum χ^2 .

2.2.3 Geometry of detection volumes

The theory so far assumes that the observation volumes match exactly $MDF_1 = MDF_2$. In a two-laser setup, small mismatches in laser alignment can cause the excitation volumes to be spatially displaced and not completely overlapped (Fig. 2.3). This reduces the effective observation volume for the cross-correlation and in turn lowers the CCF amplitude relative to the ACF amplitudes (for a more in-depth explanation and correction to non-overlapping observation volumes, see [60]). In a single-laser setup, although there is no mismatch of laser alignment,

additional aspects affecting the detection volume have to be considered. First, the size of the detection volume is dependent on the emission wavelengths of the dyes. Given two emission peak wavelengths of a green and red dye to be 520 nm and 670 nm, respectively, their effective observation volume would differ by a factor of 2.14 (Eq. 2.12). Second, the centers of the respective foci could be displaced in axial directions due to chromatic aberrations of the microscope objective and the optical system in the detection path. This leads to a modified correlation function

$$G_{12}(\tau) = \frac{1}{CV_{eff,12}} \left(1 + \frac{4D\tau}{w_{o,12}^2}\right)^{-1} \left(1 + \frac{4D\tau}{z_{o,12}^2}\right)^{-1/2} \quad (2.41)$$

$$\exp\left(-\frac{d_x^2 + d_y^2}{4D\tau + w_{o,12}^2} - \frac{d_z^2}{4D\tau + z_{o,12}^2}\right) \quad (2.42)$$

$$w_{o,12}^2 = \frac{1}{2}(w_{o,1}^2 + w_{o,2}^2) \quad (2.43)$$

$$z_{o,12}^2 = \frac{1}{2}(z_{o,1}^2 + z_{o,2}^2) \quad (2.44)$$

$$V_{eff,12} = \pi^{3/2} w_{o,12}^2 z_{o,12} \quad (2.45)$$

d is the displacement vector between the centers of the two foci and Eqs. 2.41 and 2.44 define the $1/e^2$ radii of the Gaussian distributions MDF_1 and MDF_2 . A displacement of the detection volumes will lead to a reduction of the amplitude and a shift of the CCF toward longer diffusion times [132].

2.2.4 SW-FCCS Setup

Fig. 2.4 shows the dual-color fluorescence cross-correlation setup using only a single laser line for excitation. It is similar to a typical FCS setup except that the emission beam is separated with a dichroic mirror into two different detection channels. The excitation beam (488 nm) from an Argon-Krypton laser (Melles Griot, Singapore) is expanded by two achromats $f = 20$ mm and $f = 80$ mm (Linos, Heidelberg, Germany) and reflected by a dichroic mirror 505DRLP (Omega Optical, Brattleboro, USA) into a water immersion Objective C-Apochromat 63x/1.2 NA that is chromatically corrected (Carl Zeiss, Singapore). The fluorescence light is

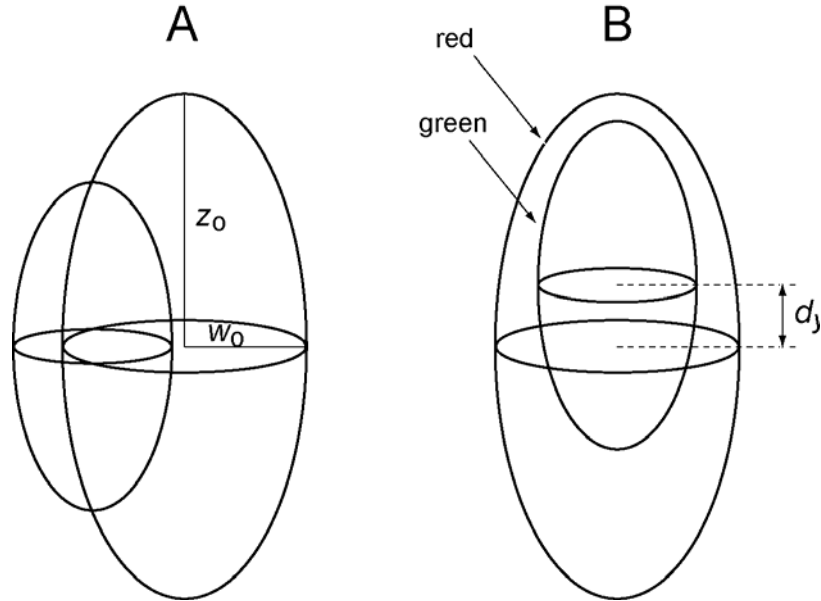


Figure 2.3: Foci geometry of two overlapping detection volumes differing in size for different emission wavelengths. (A) Geometry of detection volume is described by 3D Gaussian functions where w_0 and z_0 is the $1/e^2$ of the radius and axial axis respectively. The lateral shift in the detection volumes is induced by the misalignment of two laser beams. (B) Axial shift of detection volumes by d_y is possible with a single laser beam. This is because of chromatic displacements from aberrations in optics.

focused by a tube lens with focal length 164.5 mm onto a 50 μm pinhole (Linos) placed at the image plane. The emission light is split by a second dichroic mirror 560DRLP (Omega) and refocused by achromat lenses (L4 and L5) with a 1:1 image onto the two avalanche photodiodes (SPCM-AQR-14, Pacer Components, Berkshire, UK). Emission bandpass filters 510AF23 and 695AF55 (Omega) are placed in front of the two APDs. Correlations are performed by an external hardware correlator (Flex02-12D, correlator.com, Zhejiang, China). The correlation curves are fitted with the Levenberg-Marquardt algorithm using Igor Pro software (Wavemetrics) on a computer. Since the microscope objective used in this setup is chromatically corrected, the difference in the wavelength-dependent detection volumes could be corrected using two pinholes with different sizes.

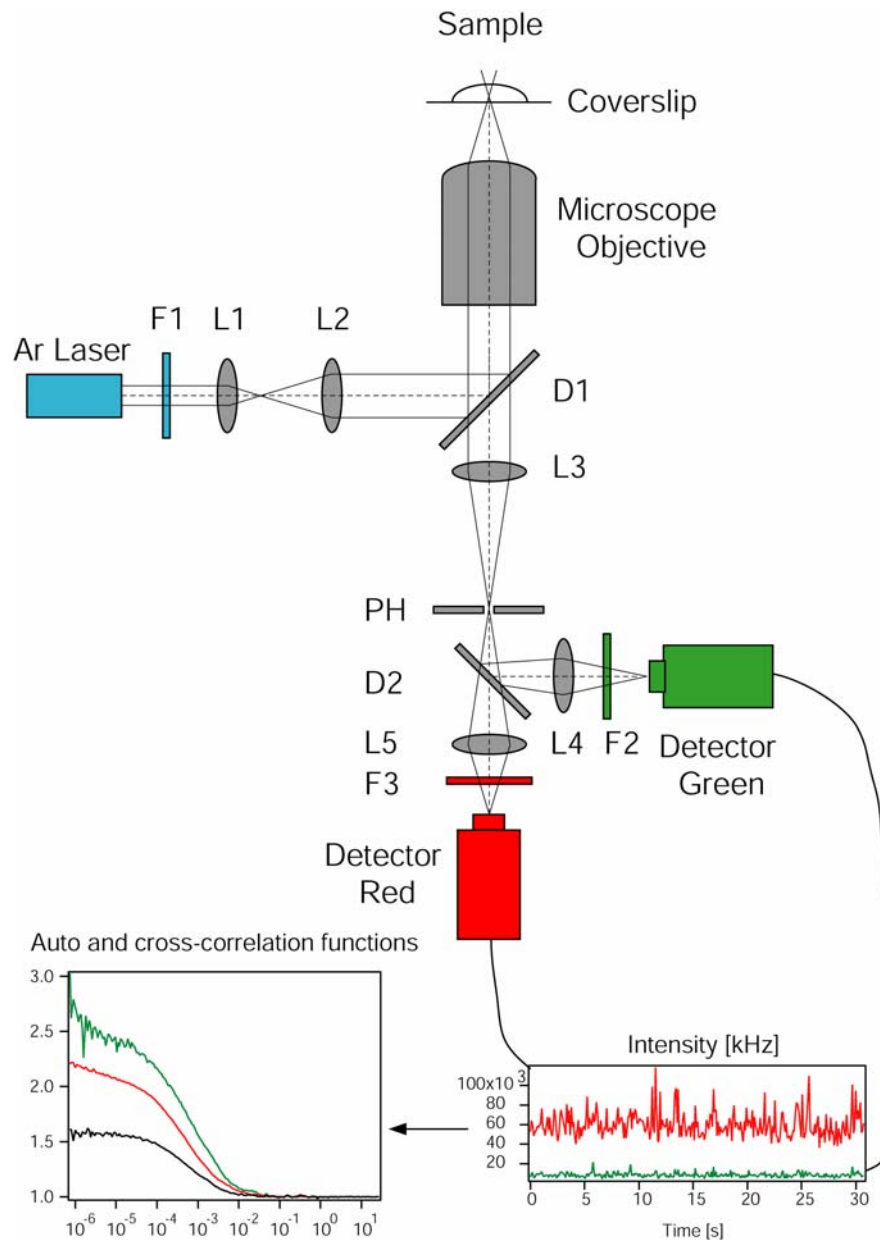


Figure 2.4: The dual-color SW-FCCS setup consists of a single laser beam expanded and collimated by lenses L1 and L2. The microscope objective focuses the beam into the sample. The fluorescence light emitted is focused by the tube lens L3 and split two-ways into different wavelength regions via dichroic mirror D2. Lenses L4 and L5 focus the emission beams onto the green and red detectors respectively. The intensity signals from green and red wavelengths (bottom right) are autocorrelated to give individual autocorrelation functions (bottom left) and cross-correlated to give the cross-correlation function (black curve). F1: excitation filter; F2 and F3: emission bandpass filters; L1-L5: lenses; D1 and D2: dichroic mirrors.

Chapter 3

Dual-color SW-FCCS

3.1 Introduction

Dual-color FCCS setups typically consist of a confocal system in which two lasers are focused at the same spot. The difficulty in the alignment of two lasers prevented the wide-spread use of FCCS [133] and led other reserach groups to alternative excitation methods using multi-line laser [78] and two-photon excitation [86]. It has been suggested that a system of two fluorophores excited at the same wavelength but with different Stokes shifts can be used but until now, no adequate system has been proposed [64, 86].

This chapter describes the methodology of single wavelength FCCS (SW-FCCS) using only one laser beam to excite a combination of labels with largely different Stokes shifts. For this purpose fluorescent probes, tandem dyes [106] and quantum dots [93] are used. The theory for FCCS applied to equilibrium binding of bimolecules is formulated and the optical setup presented earlier in chapter 2 is utilized for the experiments described in this chapter. As a model system for receptor-ligand interactions, fluorescein-labeled biotin (BF) and streptavidin labeled with quantum red (QR) or quantum dot 655 (QD655) are investigated to determine the dissociation constant and stoichiometry of binding. The theoretical framework and methodology presented here acts as a basis that can be extended

to higher order molecular interactions (see chapters 4 and 5). This approach to perform FCCS circumvents the need to align and overlap two laser beams. Thus, avoiding problems and artefacts that are produced from the mismatch in excitation volumes.

3.2 Theory

Fluorescence correlation spectroscopy involves the statistical analysis of fluorescence fluctuations coming from an illuminated observation volume. These fluctuations may arise from fluorescence labeled molecules undergoing different processes such as Brownian motion, fast transition between singlet and triplet states and receptor-ligand interactions. Fluorescence signals $F_i(t)$ and $F_j(t)$ in detector channels i and j are correlated according to the normalized correlation function $G_{ij}(t)$ shown in chapter 2, theory section.

Assuming equilibrium binding of ligand to receptor at 1:1 stoichiometry (for further discussion of receptor ligand interactions see Hulme, 1992 [134]), the bimolecular reaction is described by the following scheme



R represents the receptor, L the ligand and RL the receptor-ligand complex. The dissociation constant of the reaction K_d is defined by the law of mass action: ratio of the concentrations of the free receptor $[R]$ and the free ligand $[L]$, to the concentration of the complex $[RL]$. The concentrations of the free components are then given by the total concentration of receptor $[R]_t$ or ligand $[L]_t$ minus the concentration of receptor-ligand complexes.

$$\begin{aligned}
 K_d &= \frac{[R][L]}{[RL]} \\
 &= \frac{([R]_t - [RL])([L]_t - [RL])}{[RL]} \\
 &= \frac{[R]_t [L]_t - [R]_t [RL] - [L]_t [RL] + [RL]^2}{[RL]} \quad (3.2)
 \end{aligned}$$

Eq. 3.2 is transformed into a quadratic equation and solved for $[RL]$. Only one solution was considered to give physically correct results shown in Eq. 3.4.

$$0 = [RL]^2 - [RL](K_d + [R]_t + [L]_t) + [R]_t [L]_t \quad (3.3)$$

$$[RL] = \frac{(K_d + [R]_t + [L]_t)}{2} - \sqrt{\frac{(K_d + [R]_t + [L]_t)^2}{4} - [R]_t [L]_t} \quad (3.4)$$

The time dependent total fluorescence signal $F_i(t)$ in detection channel i is the sum of all fluorescent species ($s = L, R, RL$) contributing to the signal. It is determined by their fluorescence yields, η_L^i and η_R^i (often expressed as photon counts per molecule per second), and the time dependent number of particles $N_A V_{eff} C_s(t)$ in the effective observation volume V_{eff} . $N_A = 6.023 \times 10^{23} \text{ mol}^{-1}$ is the Avogadro's number and $C_s(t)$ represents the time dependent values of the averages C_{RL} , C_L and C_R . All possible species that contribute via cross-talk into the detection channels are taken into account as shown by

$$\begin{aligned}
 F_i(t) &= F_L^i(t) + F_R^i(t) + F_{RL}^i(t) \\
 &= N_A V_{eff} [\eta_L^i C_L + \eta_R^i C_R + \eta_{RL}^i C_{RL}] \quad (3.5)
 \end{aligned}$$

Assuming a 3D Gaussian illumination intensity profile and keeping only factors that contribute to the cross-correlation, Eq. 3.5 is substituted into Eq. 2.1 to obtain the cross-correlation between green g and red r channels. The cross-

correlation amplitude of the positive control at $\tau = 0$ is

$$G_{\times}^{+}(0) = \frac{\eta_L^g \eta_L^r C_L + \eta_R^g \eta_R^r C_R + (q_L \eta_L^g + q_R \eta_R^g) (q_L \eta_L^r + q_R \eta_R^r) C_{RL}}{N_A V_{eff} \left[\begin{array}{l} (\eta_L^g C_L + \eta_R^g C_R + (q_L \eta_L^g + q_R \eta_R^g) C_{RL}) \times \\ (\eta_L^r C_L + \eta_R^r C_R + (q_L \eta_L^r + q_R \eta_R^r) C_{RL}) \end{array} \right]} \quad (3.6)$$

The changes in fluorescence yields upon binding for ligand and receptor are described by q_L and q_R . In accordance with experiments, the changes in fluorescence yields are assumed to be equal in both detection channels. For an unequal change that may arise from FRET or emission wavelength shifts, different factors will have to be considered for both channels. Given that

$$\eta_{RL}^g = q_L \eta_L^g + q_R \eta_R^g \quad (3.7)$$

$$\eta_{RL}^r = q_L \eta_L^r + q_R \eta_R^r \quad (3.8)$$

Eq. 3.6 is simplified to

$$G_{\times}^{+}(0) = \frac{\eta_L^g \eta_L^r C_L + \eta_R^g \eta_R^r C_R + \eta_{RL}^g \eta_{RL}^r C_{RL}}{N_A V_{eff} (\eta_L^g C_L + \eta_R^g C_R + \eta_{RL}^g C_{RL}) (\eta_L^r C_L + \eta_R^r C_R + \eta_{RL}^r C_{RL})} \quad (3.9)$$

From Eq. 3.9 it is clear that the contribution of the different particles depends solely on the product of their fluorescence yields in the two detectors. Because there are no complexes formed for the negative control, the cross-correlation amplitude of the negative control includes only contribution from the cross-talk of the free components.

$$G_{\times}^{-}(0) = \frac{\eta_L^g \eta_L^r C_L + \eta_R^g \eta_R^r C_R}{N_A V_{eff} (\eta_L^g C_L + \eta_R^g C_R) (\eta_L^r C_L + \eta_R^r C_R)} \quad (3.10)$$

3.3 Materials and Methods

The SW-FCCS setup and configuration have been shown earlier in chapter 2. Quantum red streptavidin conjugate (5 nM, Sigma-Aldrich, Singapore) was in-

cubated with biotin-fluorescein (0–50 nM, Molecular Probes, Eugene, USA) for at least 1/2 hour. Negative controls were prepared with excess D-biotin (1 μ M, Amersham Biosciences Ltd, Singapore). QD655 were purchased from Quantum Dot Corp., Hayward, USA. Negative controls were prepared with free fluorescein (Molecular Probes). All solutions were prepared in phosphate buffer solution (PBS) at pH 7.4 (Sigma-Aldrich). Correlation times were 20–30 s.

3.4 Results and Discussion

3.4.1 Characterization of fluorophores

The fluorophores used for SW-FCCS have to be selected based on several criteria. First, they are required to have largely different Stokes shifts for minimal emission spectral cross-talk in the detection channels. Second, the fluorophores need to have similar excitation characteristics where they can be optimally excited at the same laser wavelength and power with negligible photobleaching. A suitable set of dichroics and emission filters has to be chosen to match the maximum emission wavelengths of the fluorophores while reducing cross-talk.

In this chapter, the fluorophore pairs BF/QR and BF/QD655 were chosen due to their large differences in Stokes shifts. This is so that detector cross-talk can be effectively suppressed (emission spectra shown in Fig. 3.1 A). Tandem dyes consist of yellow emitting phycobiliproteins linked to 3–6 molecules of red emitting dyes e.g. Cy5 or Alexa Fluor 647. In this case, QR consists of a R-phycoerythrin (RPE) donor molecule conjugated to \sim 4 Cy5 acceptor molecules. The emission spectrum of RPE overlaps with the excitation spectrum of the conjugated Cy5 molecules. When excited at 488 nm, non-radiative resonance energy transfer [8] occurs from RPE to Cy5 and fluorescence emission is shifted to the red wavelengths. However, there is still a low fluorescence signal emitting from the RPE molecule at 575 nm. This contributes to most of the cross-talk into the green detector and even with QD655, cross-talk cannot be completely suppressed.

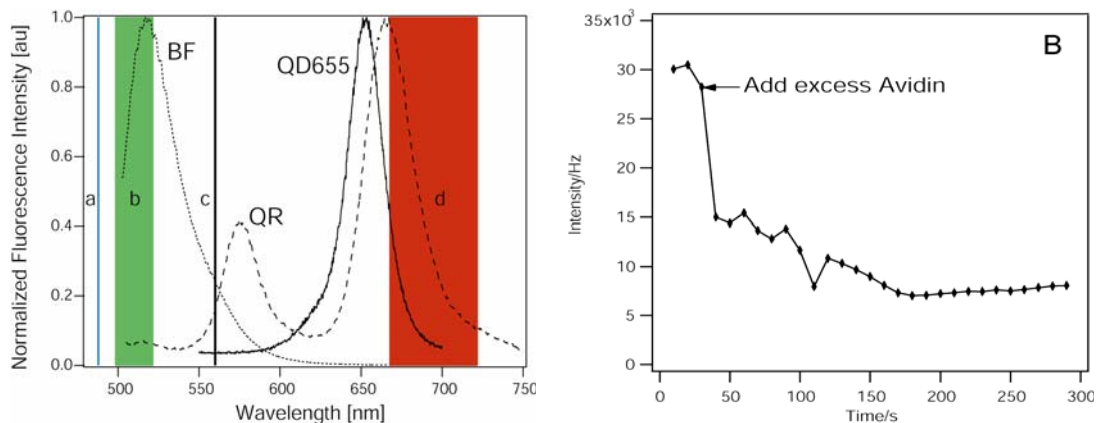


Figure 3.1: (A) Normalized fluorescence emission spectra for BF (dotted curve), QR (dashed curve) and QD655 (solid curve). Indicated are (a) the laser excitation wavelength at 488nm, (b) the emission filter transmission range for green detector, (c) the dichroic mirror center wavelength for the separation of the emission light into both detectors, and (d) the emission filter transmission range for red detector. (B) Intensity trace of BF shows the quenching of fluorescence upon addition of excess unlabeled avidin. Fluorescence intensity reduced by $\sim 75\%$. Each data point represents an average of 10 s intensity measurement

The system was calibrated with a reference fluorescein dye of 1 nM at a laser power of 100 μW for 10 correlations, each at 30 s. The ACFs were fitted to obtain the parameters $\tau_d = 55.9 \mu\text{s}$ and $K = 2$, which was fixed for all future fits. The previously reported diffusion coefficient of fluorescein at $D = 3.0 \times 10^{-6} \text{ cm}^2/\text{s}$ [37] was used to determine a beam waist $w_o = 259 \text{ nm}$ and $V_{eff} = 0.19 \text{ fl}$. The fluorescence yields η in each channel were measured and calculated from the photon counts per second divided by the number of molecules N (Table 3.1). N was determined from the amplitudes of the ACF fits. BF was quenched by $\sim 75\%$ ($q_{BF} = 0.25$) upon binding to streptavidin in accordance with the literature values of 77 – 84% [123] (Fig. 3.1 B), while the fluorescence yields of QR and QD655 remained unperturbed upon binding biotin ligands (q_{QR} and $q_{QD655} = 1.0$). Therefore, the contribution to the CCF of the bound complexes was larger than the contributions of the unbound species by a factor of 2 and 5 for QR and QD655, respectively (Eq. 3.9). It is this fact that allows the determination of binding by SW-FCCS.

The ACFs and CCFs of QR were measured on the SW-FCCS setup (D2:

Units in Hz	η^g	η^r	q_s
BF	34,300	200	0.25
QR	7,000	75,700	1.0
QD655	2,000	121,000	1.0
Units in kHz ²	$\eta_L^g \eta_L^r$	$\eta_R^g \eta_R^r$	$\eta_{RL}^g \eta_{RL}^r$
QR-BF	6.86	530	1180
QD655-BF	6.86	242	1280

Table 3.1: Photon counts per particle determined by SW-FCCS. η^i represents the fluorescence yields in i channels, where i is green or red. q_s is the fluorescence quenching factor for species, s . The fluorescence yield products determine the weighting factor for the cross-correlation function. All photon count rates per particle were measured at a laser power of 100 μ W

560DRLP, F2: 510AF23, F3: 695AF55) at various laser powers. The CCFs were measured for green \times red ($g \times r$) and red \times green ($r \times g$) and fitted with a one-component diffusion model. The diffusion times obtained from the fits were longer for $r \times g$ as compared to $g \times r$ and the difference increases toward higher laser intensities (Fig. 3.2, A and C). Fig. 3.2 A shows at higher laser power, τ_d for $g \times r$ decreased by $\sim 60\%$ while τ_d for $r \times g$ remains almost constant. This could be attributed to Cy5 acceptor photobleaching. For photostable dye molecules traversing through the red and green detection volumes, the intensity signal fluctuates at a shorter timescale in the green channel than in the red channel due to its different volumes (Fig 3.3 A), but the τ_d s of $g \times r$ and $r \times g$ CCFs are the same. However, Fig. 3.3 B shows that when the Cy5 molecules of a QR molecule photobleaches as it diffuses through the confocal volume, the apparent τ_d spent within the confocal volume as a bright molecule becomes shorter. Therefore, for the same QR molecule, both green and red intensity signals will rise concomitantly as it enters the confocal volume. But upon photobleaching of the Cy5 molecules, the red signal will drop back to the level of the background signal faster than the green signal. This causes the width of the red intensity signals to be narrower compared with the green intensity signals. Thus, the $g \times r$ CCF will have a shorter decay time when cross-correlating the green intensity signal and the red intensity signal i.e. $F_g(0)F_r(\tau)$ (Eq. 2.1). At higher laser powers, τ_d of $g \times r$ CCF becomes even smaller due to stronger acceptor photobleaching. Since the RPE molecules

do not photobleach, τ_d of $r \times g$ CCF remains almost constant as the normalized $F_r(0)F_g(\tau)$ remains unchanged with different laser intensities.

Fig. 3.2 B shows the number of particles increasing with laser power. This is most likely due to the increase in the MDF of both green and red channels with increasing laser intensity [129]. Since there is almost no difference between N of $g \times r$ and $r \times g$, either one of the CCF amplitudes could be used for data analysis. Here, τ_d was not taken into account for binding analysis, thus, data from $g \times r$ was used for all analyses.

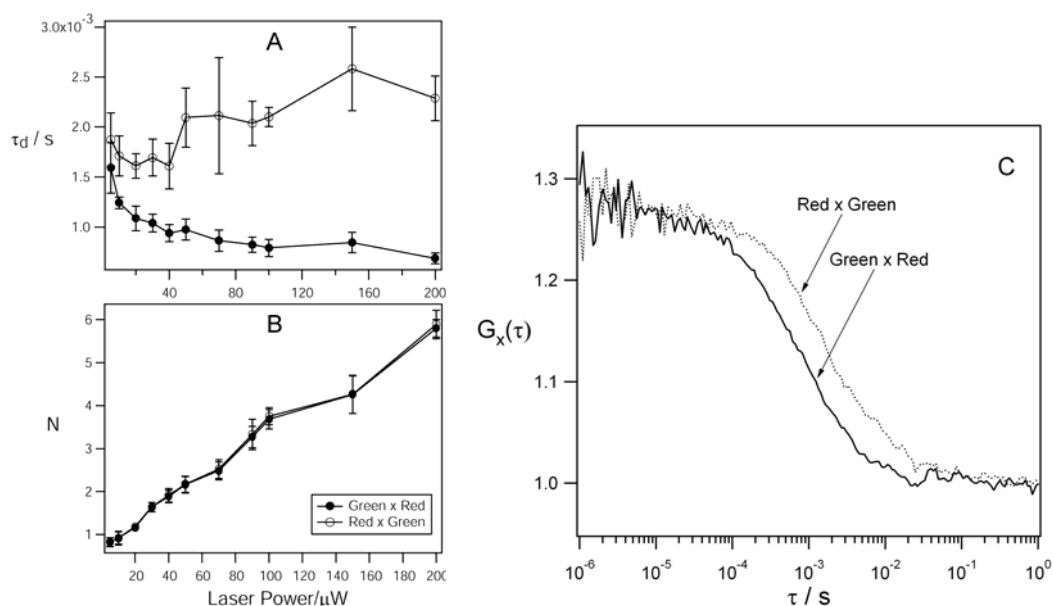


Figure 3.2: (A) Diffusion times and (B) number of particles of QR obtained from the fits of the cross-correlation functions between detection channels $g \times r$ and $r \times g$ at varying laser power. (C) The shift in the cross-correlation curve towards longer diffusion times for $r \times g$ is due to conjugated Cy5 acceptor photobleaching. Cross-correlation functions are measured at laser power $100\mu\text{W}$.

Fig 3.4 A shows the change of green and red average fluorescence intensities and count rates per molecule (cpm) of QR with increasing laser power. This was performed with a filter set (D2: 595DRLP, F2: 545AF75, F3: 670DF40) that permits maximum intensity rates at the emission maxima of 575 nm and 670 nm. The increase in intensity in the red channel saturates above 40 μW and the cpm decreases beyond 40 μW . On the other hand, the green intensity increases above 40 μW , albeit at a slower rate and the green cpm remains almost constant. This

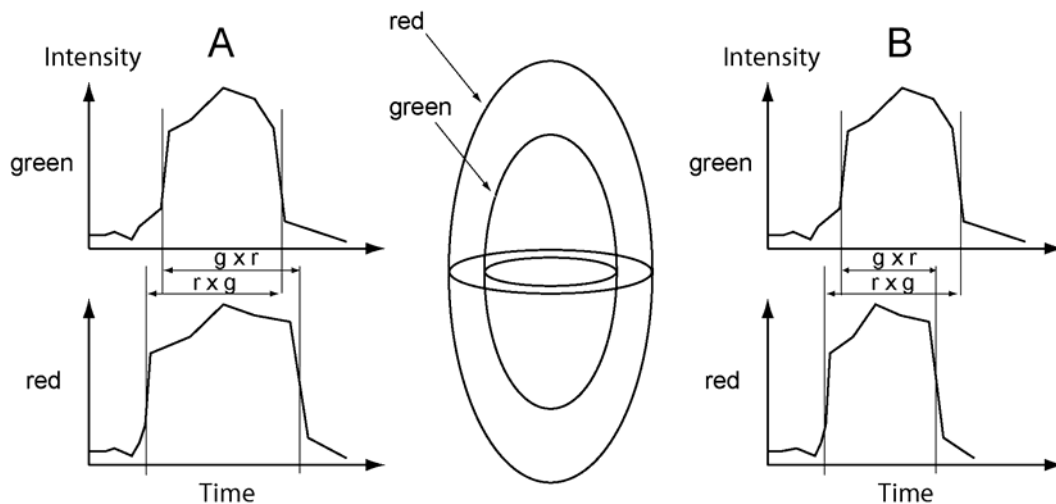


Figure 3.3: Schematic drawing of fluorescence intensity signal in the green and red detection channels and their wavelength-dependent detection volumes (center). (A) The different widths of the intensity signals from the fluorescing molecules are due to the different sizes of detection volumes. For a bound green-red molecule diffusing simultaneously through the observation volume, the cross-correlation functions between green \times red ($g \times r$) and red \times green ($r \times g$) have the same diffusion times. (B) When a QR molecule diffuses through the observation volume, the conjugated Cy5 molecules photobleaches, producing a narrower red intensity signal. The diffusion times from cross-correlation functions of $g \times r$ becomes shorter than that for $r \times g$.

substantiates the explanation of Fig. 3.2 that acceptor (Cy5) photobleaching of QR molecules occurs and becomes more pronounced above the excitation power of $40 \mu\text{W}$. The ratio of red intensity to green intensity in Fig. 3.4 B shows that the green intensity increases at a faster rate than the red intensity. From $\sim 60 \mu\text{W}$ onwards, green intensity rises above red intensity and the ratio drops below unity.

To further verify that the difference in cross-correlation times between both detector channels are due to acceptor photobleaching of QR, QD565 and fluorescein were calibrated at different laser powers (D2: 560DRLP, F2: 510AF23, F3: 595AF60). The τ_{dS} of $g \times r$ and $r \times g$ CCFs were compared in Fig. 3.5 A and C. There shows no difference in the τ_{dS} for both cross-correlations measured and the τ_{dS} do not change (i.e. remain within its standard deviations) at higher laser power. The green and red intensities and the intensity ratios are shown in Fig. 3.5, B and D. For QD565 and fluorescein, the intensity ratio increases linearly with in-

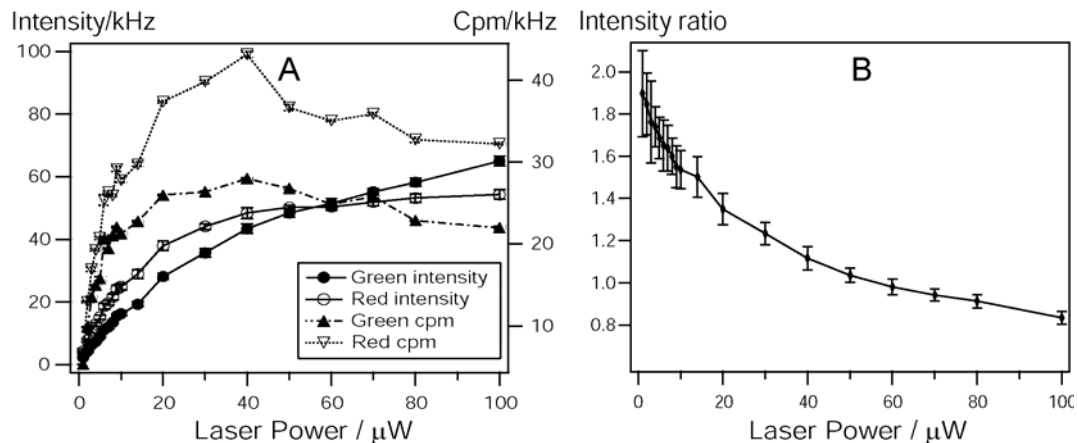


Figure 3.4: (A) The average photon count rate of QR from the green and red detection channels with varying laser power. The red intensity becomes saturated and the red count rates per molecule (cpm) decreases beyond $40 \mu\text{W}$. This indicates acceptor photobleaching of QR dye. Each point represents an average of 10 correlations at 10 s for each run. (B) Intensity ratio of red to green intensity illustrates the green intensity increasing at a faster rate than the red intensity.

creasing laser power. From the results, the dyes did not appear to photobleach at high laser intensities. This corroborates the evidence of acceptor photobleaching of QR.

3.4.2 SW-FCCS experiments of streptavidin-biotin binding

In Fig. 3.6, CCFs for binding and inhibition conditions of BF/QR are depicted. The amplitudes of the CCF for constant QR concentration and varying BF concentrations are shown in Fig. 3.7 and at least three different regions exist:

(1) A concentration ratio of $[\text{BF}]/[\text{QR}] \leq 1$ where the amplitude decreases steadily because the number of QR-BF complexes rises with increasing BF concentrations.

(2) At $1 < [\text{BF}]/[\text{QR}] \leq 3-4$, the amplitude decreases more slowly (compared to inhibition case) and more than one BF ligand is bound to QR. Although the number of QR-BF complexes remain constant, the amplitude will continue to decrease albeit with a smaller slope. Theoretically in the region where there are 0-4 BF molecules binding per QR receptor, there should be an increase in

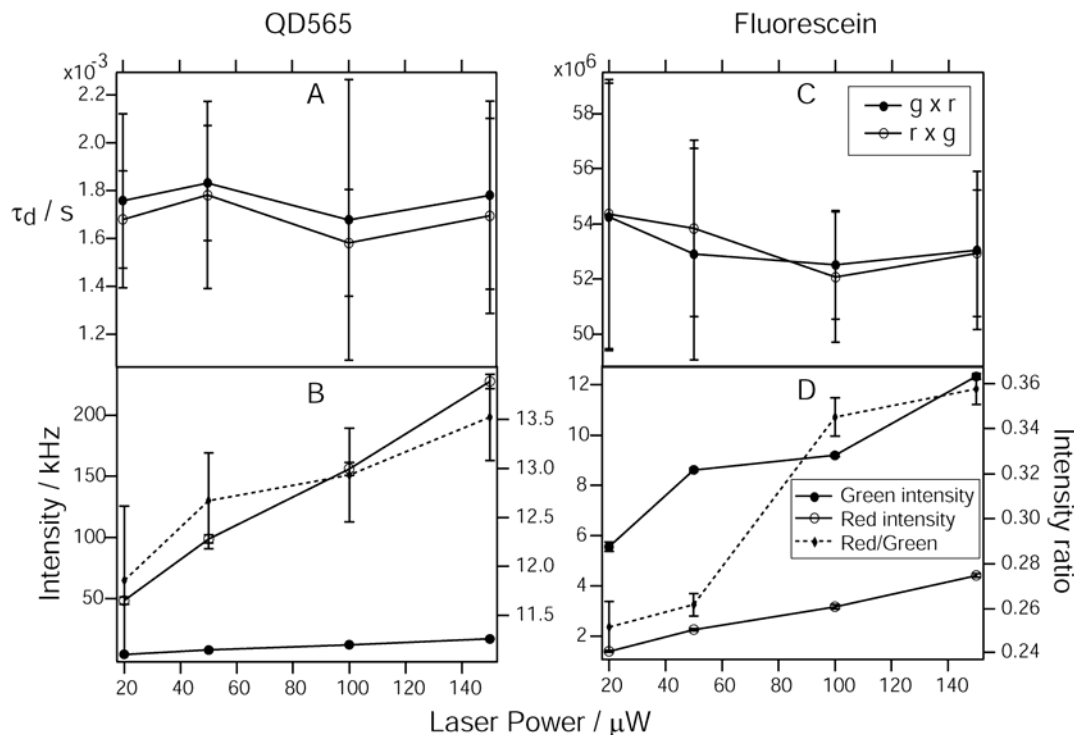


Figure 3.5: Diffusion times of cross-correlation functions between $g \times r$ and $r \times g$, average intensity and their intensity ratio of (A and B) QD565 and (C and D) fluorescein in both detection channels. The constant τ_d and linear increase of intensity ratio with laser power indicates there is no photobleaching of the dye molecules.

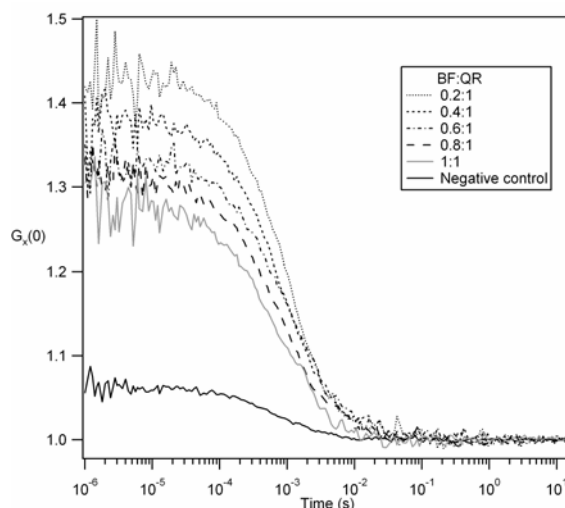


Figure 3.6: Amplitude of the cross-correlation curves decreases with increasing concentrations of bound species. BF/QR binding ratios from 0.2:1 to 1:1 are depicted against the 1:1 negative control curve. All measurements were performed at an excitation wavelength of 488 nm. Laser power = 100 μW .

cross-correlation amplitude. This is because the fluorescence yield of the QR-BF complex increases according to the number of BF molecules bound. Hence, increases the contribution of the complex to the numerator of $G_{\times}^{+}(0)$ (Eq. 3.9). However, the concentration of the reactant BF does not remain constant in this equilibrium binding reaction. It contributes to the denominator of $G_{\times}^{+}(0)$ (Eq. 3.9) and lowers the amplitude toward higher BF concentrations. Therefore, considering that if all reactants bind to form complexes i.e. equilibrium binding with high affinity, the CCF amplitude should remain roughly constant (see simulations in chapter 4, section 4.4.1). For equilibrium binding reactions with lower affinity, free reactants will contribute to the background signal in the CCF. Here, free BF molecules contribute to the denominator of the CCF by lowering its amplitude as BF concentrations increase (Fig. 3.7).

(3)[BF]/[QR] > 3–4 where all binding sites are occupied and only the number of free unquenched BF molecules increases. This leads to a sharp decrease in amplitude in accordance with Eq. 3.9, and a convergence of the amplitude toward the inhibition case.

For the inhibition case, in which binding of BF to QR was inhibited by excess unlabeled biotin, no complexes are formed and the amplitude decreases exponentially. This is expected since in both cases the decline stems from rising concentrations of BF that contribute stronger to the denominator than the numerator (Eq. 3.9). From the experimental data it is concluded that stoichiometry of binding of BF to QR is 3–4:1 (actual value 4:1). This inaccuracy is attributed to deviations from a 1:1 binding labeling with streptavidin in QR.

This chapter concentrates on region 1 with 1:1 binding of BF to QR. The experimental ratios of amplitudes for the binding and inhibition case ($G_{\times}^{+}(0)/G_{\times}^{-}(0)$) are fitted with Eq. 3.9/Eq. 3.10 and shown in Fig. 3.8. While the data clearly indicates K_d lower than 3×10^{-10} M, the fit results in $K_d = 7.1 \times 10^{-11}$ M that is consistent with published values ($K_d = 10^{-15}$ M) [120].

Fig. 3.9 shows the same plots with experiments performed on QD655. The

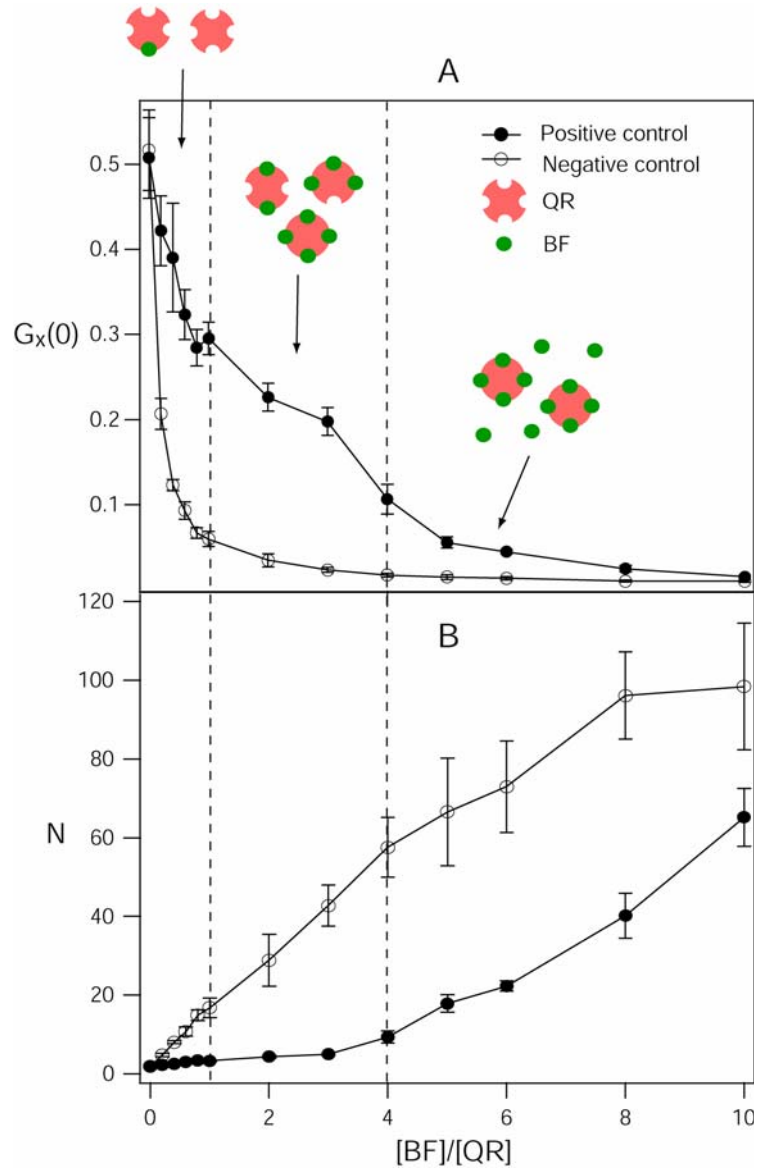


Figure 3.7: (A) Plot of cross-correlation amplitudes and (B) number of particles obtained from their fits with increasing ratio of BF to QR. The graphs shows the difference between positive control (filled circles) and negative control (empty circles). The binding curve can be separated into 3 regions (dashed lines): (1) $[BF]/[QR] \leq 1$, (2) $1 < [BF]/[QR] \leq 3-4$, (3) $[BF]/[QR] > 3-4$. The schematic drawing indicates the different binding conditions in the three regions. The stoichiometry of binding is determined to be between 3 and 4.

best fit of K_d is 5.8×10^{-10} M with the lowest χ^2 value. But due to the large standard deviations, a K_d as high as 4×10^{-9} M would still lie within the margins of error. This may be due to the large molecular size of QD (10–15 nm) that affects the binding affinity and a difficulty in fitting the CCF curves due to strong aggregate formation as observed during measurements. However, even in this case binding can be shown despite large errors in determining K_d .

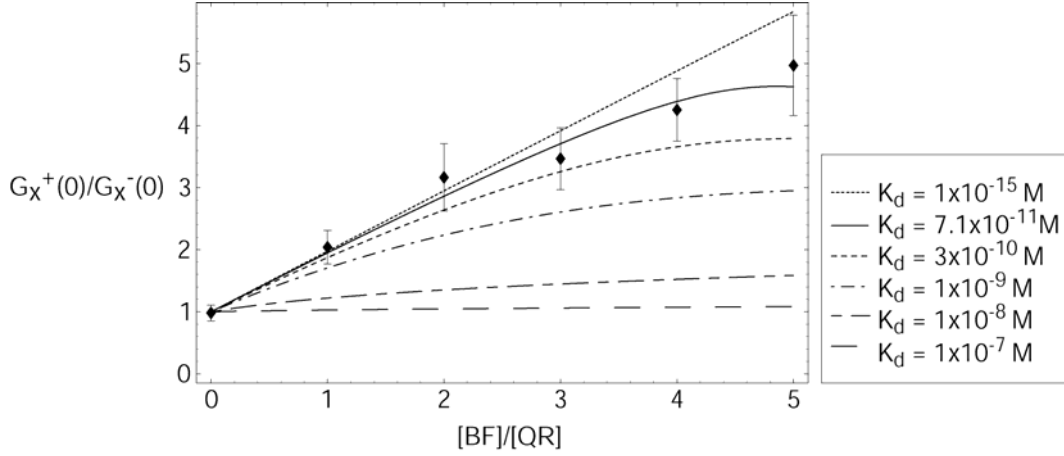


Figure 3.8: Plot of $G_X^+(0)/G_X^-(0)$ versus ratio of BF concentration to QR concentration at $[BF]/[QR] \leq 1$. The experimental data point (diamonds) can be fitted with a $K_d = 7.1 \times 10^{-11}$ M (solid line). Theoretical curves are given for $K_d = 10^{-15}$ M to 10^{-7} M.

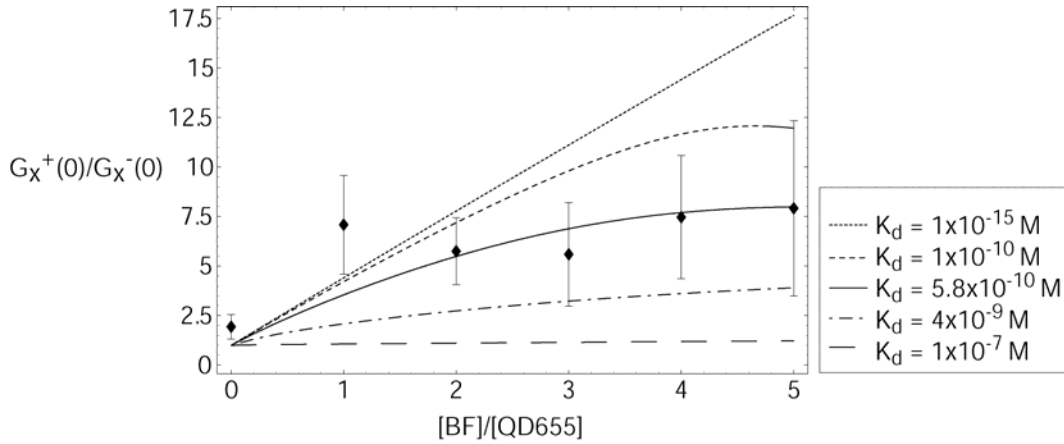


Figure 3.9: Plot of $G_X^+(0)/G_X^-(0)$ versus ratio of BF concentration to QD655 concentration at $[BF]/[QD655] \leq 1$. The experimental data points (diamonds) can be fitted with a $K_d = 5.8 \times 10^{-10}$ M (solid line). Theoretical curves are given for $K_d = 10^{-15}$ M to 10^{-7} M.

3.5 Conclusion

This chapter shows the theory and experimental realization of FCCS with single laser wavelength excitation. This simplifies conventional FCCS setups considerably and circumvents the problems of multiple laser alignment or two-photon excitation [66, 133].

The theory of SW-FCCS relating to a bimolecular equilibrium binding reaction of 1:1 stoichiometry has been formulated. Fluorescent probes, QR, QD655 and fluorescein were characterized on the setup and their fluorescence yields determined in the different detection channels. QR was observed to have acceptor photobleaching in the red detection channel and increased toward higher laser intensities.

Receptor-ligand binding between QR or QD655-labeled streptavidin and fluorescein-labeled biotin (BF) were measured with SW-FCCS. The CCF amplitude decreased with increasing QR/QD655-BF complexes and the ratio of CCF amplitude of positive control to negative control was fitted with the theoretical model to obtain their K_d s. QR-BF had a K_d similar to literature value but QD655-BF had a smaller binding affinity because of its large size and tendency to aggregate.

The use of fluorophores with large relative molecular weight is a problem that has to be resolved in the future. But since the difference in the CCF for binding and inhibition cases rests only on the fact that the fluorescence yield products of the bound complex are sufficiently different from the unbound species (Table 3.1), it is likely that this technique can be extended to other fluorophores. This is shown in chapters 4 and 5.

Chapter 4

Resolution of SW-FCCS

4.1 Introduction

In chapter 3, SW-FCCS was shown to work with fluorophore pairs with largely different emission characteristics. The method was able to detect the receptor-ligand binding of streptavidin labeled with quantum red or quantum dots and fluorescein-labeled biotin. The dissociation constants were also derived from the experimental fits. However, the limitations of the method to detect biomolecular interactions have yet to be addressed. What are the factors that affect the resolution of SW-FCCS to detect binding and can the method resolve binding using fluorophore pairs with similar spectral characteristics?

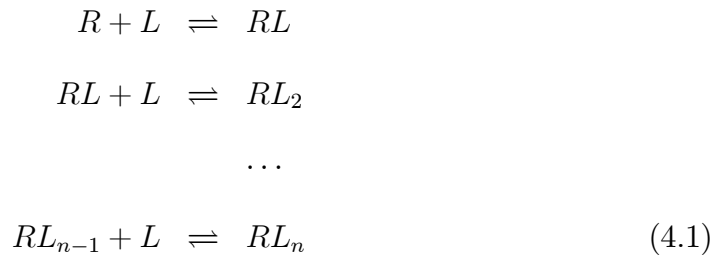
This chapter demonstrates that SW-FCCS can be conducted with fluorophores with similar excitation and emission spectra. The SW-FCCS theory from chapter 3 is extended to a binding stoichiometry of 1:4 and the limitations of SW-FCCS are determined in dependence of cross-talk, quenching, and sample impurities. Interactions of 1:1 stoichiometry are of significance as it is where neither the mass nor the molecular brightness change is sufficient to allow for the detection of binding by FCS. The use of organic dyes with similar emission spectra will inevitably result in a lower sensitivity of SW-FCCS compared to FCCS using two excitation lasers. This is due to the higher spectral cross-talk. However,

it is shown that even for measurements at a single concentration ratio between receptor and ligand, differences of more than 6 standard deviations in the amplitude can be attained. Binding between fluorescein-labeled biotin (BF) and tetramethylrhodamine-labeled streptavidin (TMRSA) is shown and the dissociation constant and stoichiometry of binding are determined.

4.2 Theory

4.2.1 Receptor-ligand complexes

Assume a receptor-ligand system consisting of R , a receptor with multiple binding sites for ligand L both fluorescence labeled. Considering a solution of receptor and ligands, free ligands L will bind with free receptors R to form complex RL_n at equilibrium binding where n is the number of bound ligands on R . Assume that each complex formed consists of one receptor with several ligands specifically bound, therefore excluding oligomerization of this receptor.



Assuming that each binding site has the same affinity. If the multiplicity of the binding sites is disregarded, the K_d for each individual binding site is then given by the law of mass action where the concentration of free and active reactants is divided by the products [134].

$$K_d = \frac{[R][L]}{[RL]} = \frac{[RL][L]}{[RL_2]} = \frac{[RL_{n-1}][L]}{[RL_n]} \tag{4.2}$$

To take into account of the multiple binding sites per receptor, binomial coefficients are introduced to describe the possibility of n ligands binding to n_t binding sites [135]. The ligands and receptors, active or inactive, are denoted by a “+” or “-“ sign in the superscript (L_t^+ , L_t^- , R_t^+ , R_t^-). The concentrations of free and active receptors and ligands, R_f^+ and L_f^+ , are thus related to the total concentrations of active receptor R_t^+ and ligand L_t^+ minus the sum of all bound receptors and ligands, respectively.

$$R_f^+ = R_t^+ - \sum_{n=1}^{n_t} \binom{n_t}{n} RL_n \quad (4.3)$$

$$L_f^+ = L_t^+ - \sum_{n=1}^{n_t} n \binom{n_t}{n} RL_n \quad (4.4)$$

The number of complexes with different ligands bound is calculated numerically (Mathematica 5.0, Wolfram Research, Champaign, IL) by simultaneously solving Eqs. 4.2–4.4 for equilibrium binding. It is assumed that in this reaction, all binding sites on the receptor have the same K_d . The extension of the equations to different K_d s can be obtained by using different K_d s in Eqs. 4.2–4.4.

In addition, ligands and receptors can have varying numbers of fluorophores attached that depend on the specific labeling procedure. A ligand can have between 0 and U fluorophores attached, where U is the number of labeling sites. The probability to have a specific number u between 0 and U fluorophores attached is denoted by $p_L(u)$. Similarly, a receptor can have between 0 and V fluorophores attached, where V is the number of labeling sites. The probability to have a specific number v between 0 and V fluorophores attached will be denoted by $p_R(v)$. The ligand and receptor concentrations can thus be described as

$$L_t = L_t^+ + L_t^- = \sum_{u=0}^U p_L(u) L_t^+ + \sum_{u=0}^U p_L(u) L_t^- \quad (4.5)$$

$$R_t = R_t^+ + R_t^- = \sum_{v=0}^V p_R(v) R_t^+ + \sum_{v=0}^V p_R(v) R_t^- \quad (4.6)$$

The signal in SW-FCCS is determined by the fluorescent particles, but binding is determined by the active particles. In the rest of this section the concentrations of the different possible complexes that are formed by the interaction of ligands and receptors are derived.

For the active particles, the probability of encountering a labeled/bright (*) or unlabeled/dark (°) active ligand or receptor is given by their mole fractions

$${}^*p_L = \frac{{}^*L^+}{L_t^+ + L_t^-} = \frac{\sum_{u=1}^U p_L(u) L_t^+}{\sum_{u=0}^U p_L(u) L_t^+ + \sum_{u=0}^U p_L(u) L_t^-} \quad (4.7)$$

$${}^\circ p_L = \frac{{}^\circ L^+}{L_t^+ + L_t^-} = \frac{p_L(0) L_t^+}{\sum_{u=0}^U p_L(u) L_t^+ + \sum_{u=0}^U p_L(u) L_t^-} \quad (4.8)$$

$${}^*p_R = \frac{{}^*R^+}{R_t^+ + R_t^-} = \frac{\sum_{v=1}^V p_R(v) R_t^+}{\sum_{v=0}^V p_R(v) R_t^+ + \sum_{v=0}^V p_R(v) R_t^-} \quad (4.9)$$

$${}^\circ p_R = \frac{{}^\circ R^+}{R_t^+ + R_t^-} = \frac{p_R(0) R_t^+}{\sum_{v=0}^V p_R(v) R_t^+ + \sum_{v=0}^V p_R(v) R_t^-} \quad (4.10)$$

Assuming a receptor with n_t possible binding sites and n ($0 \leq n \leq n_t$) occupied binding sites, each of these sites can have either a bright or a dark active ligand given by the probabilities in Eqs. 4.7 and 4.8. Each receptor-ligand complex can contain either a bright or a dark active receptor given by the probabilities in Eqs. 4.9 and 4.10. The concentration of all active bright receptors containing n ligands of which n^* are bright (and $(n - n^*)$ are dark) is expressed by [132].

$${}^*RL_{(n,n^*)} = \sum_{n=1}^{n_t} \binom{n_t}{n} \binom{n}{n^*} {}^\circ p_L^{n-n^*} {}^*p_L^{n^*} {}^*p_R RL_n \quad (4.11)$$

The first binomial coefficient represents the number of possibilities to distribute n ligands over n_t binding sites. The second binomial coefficient is the number of possibilities to distribute n^* bright ligands over the n occupied binding sites.

Although every ligand receptor complex contains only one receptor, it can contain several ligands with different amounts of fluorophores attached. Thus, the probability $p_C(n^*, u)$ that a complex with n^* bright ligands contains u fluorophores.

If the number of ligands is denoted by k and the number of fluorophores each ligand carries by n_k , the probability becomes

$$p_C(n^*, u) = \left[\prod_{k=1}^{n^*} p_L(n_k) \right]_{\text{sum over all permutations with } \sum_{k=1}^{n^*} n_k = u} \quad (4.12)$$

The concentration C_s of species s that contains u ligand fluorophores and v receptor fluorophores can now be calculated. Since bound and free particles have different fluorescence yields, the concentration of all bound and free particles containing u or v fluorophores respectively, and the concentration of receptor-ligand complexes containing u receptor and v ligand fluorophores are calculated.

The concentration of free bright ligands with u fluorophores and concentration of free bright receptors with v fluorophores are

$$C_L = p_L(u) \left[L_t - \sum_{n=1}^{n_t} \sum_{n^*=1}^n n^* {}^*RL_{(n,n^*)} \right] \quad (4.13)$$

$$C_R = p_R(v) \left[R_t - \sum_{n=1}^{n_t} \sum_{n^*=1}^n {}^*RL_{(n,n^*)} \right] \quad (4.14)$$

where the sum in brackets denote the total ligand or receptor concentration minus the bound ligands or receptors. The concentration of bright ligands bound to dark receptors is

$$C_{\circ R^*L} = p_C(n^*, u) p_R(0) {}^*RL_{(n,n^*)} \quad (4.15)$$

The concentration of bright receptors bound to dark ligands is

$$C_{^*R\circ L} = p_R(v) {}^*RL_{(n,0)} \quad (4.16)$$

and the concentrations of particles containing both fluorophores are given by

$$C_{RL} = p_R(v) \sum_{n=1}^{n_t} p_C(n^*, u) {}^*RL_{(n,n^*)} \quad (4.17)$$

These concentrations of particles with defined numbers of fluorophores are used

to calculate the CCF in the next section.

4.2.2 The Cross-correlation function

For the case of differently labeled ligands and receptors, which are detected in two different channels, the fluorescence in the different channels i is given by

$$F_i(t) = N_A V_{eff} \left[\begin{array}{l} \sum_{u=1}^U \eta_L^i C_L + \sum_{v=1}^V \eta_R^i C_R + \sum_{u=1}^U \eta_{\circ R^* L}^i C_{\circ R^* L} \\ + \sum_{v=1}^V \eta_{* R^{\circ} L}^i C_{* R^{\circ} L} + \sum_{u=0}^U \sum_{v=0}^V \eta_{RL}^i C_{RL} \end{array} \right] \quad (4.18)$$

Every molecule containing different numbers of u and v will have their own fluorescence yield (counts per molecule and second) in channel i . The fluorescence yields for species s (where $s = R, L, RL$) are given by η_s . These different fluorescence yields have to be included to account for the fluorescence of single- and multiple-labeled complexes, quenching effects (upon labeling or upon binding) and possible FRET in the different receptor-ligand complexes.

For a solution of the whole CCF, a characteristic time dependent process (diffusion, flow etc.) has to be assumed. This chapter concentrates on the amplitudes of the CCF but the extension to the full CCF is straightforward and the solution has been already described in chapter 2 [60, 132]. The substitution of Eq. 4.18 into Eq. 2.1, accounting for 2 detection channels i and j , and having assumed a focal intensity profile that is Gaussian in all three axes [136], the CCF is calculated [31] as

$$G_{\times}^+(0) = \frac{\sum_{u=1}^U \eta_L^i \eta_L^j C_L + \sum_{v=1}^V \eta_R^i \eta_R^j C_R + \sum_{u=1}^U \eta_{\circ R^* L}^i \eta_{\circ R^* L}^j C_{\circ R^* L} + \sum_{v=1}^V \eta_{* R^{\circ} L}^i \eta_{* R^{\circ} L}^j C_{* R^{\circ} L} + \sum_{u=0}^U \sum_{v=0}^V \eta_{RL}^i \eta_{RL}^j C_{RL}}{N_A V_{eff} \left[\begin{array}{l} \left(\begin{array}{l} \sum_{u=1}^U \eta_L^i C_L + \sum_{v=1}^V \eta_R^i C_R + \sum_{u=1}^U \eta_{\circ R^* L}^i C_{\circ R^* L} \\ \sum_{v=1}^V \eta_{* R^{\circ} L}^i C_{* R^{\circ} L} + \sum_{u=0}^U \sum_{v=0}^V \eta_{RL}^i C_{RL} \end{array} \right) \times \\ \left(\begin{array}{l} \sum_{u=1}^U \eta_L^j C_L + \sum_{v=1}^V \eta_R^j C_R + \sum_{u=1}^U \eta_{\circ R^* L}^j C_{\circ R^* L} \\ \sum_{v=1}^V \eta_{* R^{\circ} L}^j C_{* R^{\circ} L} + \sum_{u=0}^U \sum_{v=0}^V \eta_{RL}^j C_{RL} \end{array} \right) \end{array} \right]} \quad (4.19)$$

For the negative control, i.e. no binding, the fluorescence in the channels i is given by

$$F_i(t) = \sum_{u=1}^U \eta_L^i C_L + \sum_{v=1}^V \eta_R^i C_R \quad (4.20)$$

and the CCF simplifies to

$$G_{\times}^{-}(0) = \frac{\sum_{u=1}^U \eta_L^i \eta_L^j C_L + \sum_{v=1}^V \eta_R^i \eta_R^j C_R}{N_A V_{eff} \left[\left(\sum_{u=1}^U \eta_L^i C_L + \sum_{v=1}^V \eta_R^i C_R \right) \left(\sum_{u=1}^U \eta_L^j C_L + \sum_{v=1}^V \eta_R^j C_R \right) \right]} \quad (4.21)$$

It is assumed that the fluorescence yields of the different species do not change in the presence of the competitor for the negative control. Eqs. 4.19 and 4.21 are the general solutions for the CCF for binding interactions when both interaction partners are labeled.

Detection threshold for binding in SW-FCCS

In the case when SW-FCCS is used to detect simple binding, e.g. in a screening assay, the positive and negative control must differ by at least 6 standard deviations at one or more of the measured ligand and receptor concentrations. From the data collected, the standard deviation of the amplitude of the CCFs is on the order of $\Delta = 10\%$ or lower. To detect binding, the difference of amplitudes between positive and negative control has to differ by at least 6 standard deviations

$$G_{\times}^{+} - G_{\times}^{-} \geq 3\Delta (G_{\times}^{+} + G_{\times}^{-}) \quad (4.22)$$

This can be expressed in an inequality where the detection threshold R is defined as

$$R \equiv \frac{G_{\times}^{+}(1 - 3\Delta)}{G_{\times}^{-}(1 + 3\Delta)} \geq 1 \quad (4.23)$$

A measurement at a specific concentration can thus only succeed when the inequality in Eq. 4.23 is fulfilled. The ratio R depends on several parameters, in particular the (i) purity of receptor and ligand, (ii) quenching of receptor and ligand upon binding, (iii) non-specific binding, and (iv) the fluorescence yields of

ligand, receptor, and receptor-ligand complex (as measured on the setup).

Although Eq. 4.19 and 4.21 describe the CCF for the general case, they contain too many parameters to be of practical use. To be able to use these equations, as many parameters as possible should be determined independently. Therefore, the next section will discuss simplifications of the equations as applicable to the streptavidin-biotin system. It will be shown in the Results and Discussion section how the different parameters influence the detection threshold for binding.

4.2.3 The streptavidin-biotin receptor-ligand system

The streptavidin-biotin receptor-ligand system is a well-studied model system for receptor-ligand interactions. Green-emitting BF and red-shifted TMRSA are used. There are several points in this system that simplify the expression for the fluorescence intensity (Eqs. 4.18 and 4.20) and the CCF (Eqs. 4.19 and 4.21).

1) The fluorescence of TMRSA is not dependent on BF binding and no FRET was observed as there was no change in fluorescence intensity upon binding.

2) An average counts per molecule per secone (cpm) for the TMRSA is assumed, although different amounts of labels could be present on each molecule.

3) There is at most one fluorophore per ligand.

4) The fluorescence of BF is quenched by 75% upon binding (see chapter 3 and [122, 124]) but it is not dependent on the number of BF ligands bound to TMRSA or unlabeled streptavidin. Thus, a complex with n^* bright ligands will have just n^* times the fluorescence of a complex with only 1 bright ligand. In addition, the quenching is the same in both detectors and can be described by the factor $q_L = 0.25$ (this implies that there is no shift in the emission spectrum of the ligand fluorophore). With these four assumptions the fluorescence of all compounds can be described by the following parameters: the fluorescence yield of TMRSA and fluorescein in each channel, and the quenching of fluorescein upon binding q_L . Thus the fluorescence yields in Eq. 4.18 are expressed for free bright ligand, η_L^i ; free bright receptor, $\eta_R^i = v\eta_R^i$; dark ligands bound to bright receptor, $\eta_{*R^oL}^i = v\eta_R^i$;

bright ligands bound to dark receptor, $\eta_{\circ R^*L}^i = nq_L\eta_L^i$; bright receptor-ligand complex, $\tilde{\eta}_{RL}^i = v\eta_R^i + nq_L\eta_L^i$.

Since the fluorescence yield of receptor fluorophores is independent of the state of binding, terms η_R^i and $\eta_{*R^{\circ}L}$ are combined. The fluorescence intensity in channel i is written as

$$F_i(t) = N_A V_{eff} \left[\begin{aligned} &\eta_L^i C_L + \sum_{u=1}^U v\eta_R^i (C_R + C_{*R^{\circ}L}) + \sum_{n=1}^{n_t} nq_L\eta_L^i C_{\circ R^*L} \\ &+ \sum_{n=1}^{n_t} \sum_{v=1}^V \tilde{\eta}_{RL}^i C_{RL} \end{aligned} \right] \quad (4.24)$$

Substituting these equations into Eq. 2.1, the CCF between green and red detection channels is derived as

$$G_{\times}^+(t) = \frac{\eta_L^g \eta_L^r C_L + \sum_{v=1}^V v^2 \eta_R^g \eta_R^r (C_R + C_{*R^{\circ}L}) + \sum_{n=1}^{n_t} n^2 q^2 \eta_L^g \eta_L^r C_{\circ R^*L} + \sum_{n=1}^{n_t} \sum_{v=1}^V \tilde{\eta}_{RL}^g \tilde{\eta}_{RL}^r C_{RL}}{N_A V_{eff} \left[\begin{aligned} &\left(\begin{aligned} &\eta_L^g C_L + \sum_{u=1}^U v\eta_R^g (C_R + C_{*R^{\circ}L}) + \\ &\sum_{n=1}^{n_t} nq_L\eta_L^g C_{\circ R^*L} + \sum_{n=1}^{n_t} \sum_{v=1}^V \tilde{\eta}_{RL}^g C_{RL} \end{aligned} \right) \times \\ &\left(\begin{aligned} &\eta_L^r C_L + \sum_{u=1}^U v\eta_R^r (C_R + C_{*R^{\circ}L}) + \\ &\sum_{n=1}^{n_t} nq_L\eta_L^r C_{\circ R^*L} + \sum_{n=1}^{n_t} \sum_{v=1}^V \tilde{\eta}_{RL}^r C_{RL} \end{aligned} \right) \end{aligned} \right]} \quad (4.25)$$

In our experiments the competitor (unlabeled biotin) has no influence on the fluorescence yields of the labeled particles. For the negative control,

$$G_{\times}^-(t) = \frac{\eta_L^g \eta_L^r L_t + \sum_{v=1}^V v^2 \eta_R^g \eta_R^r p_R(v) R_t}{N_A V_{eff} \left(\eta_L^g L_t + \sum_{v=1}^V v\eta_R^g p_R(v) R_t \right) \left(\eta_L^r L_t + \sum_{v=1}^V v\eta_R^r p_R(v) R_t \right)} \quad (4.26)$$

It should be noted that most assumptions can be verified directly from the intensity traces recorded in the two detection channels. The values η_L^i , η_R^i , and q_L can be measured from samples by comparing the signals in the two detectors. The concentrations C_L , C_R , $C_{*R^{\circ}L}$, $C_{\circ R^*L}$ and C_{RL} can be numerically calculated from Eqs. 4.13–4.17 in dependence on the total receptor and ligand concentrations.

The unknown parameters that have to be measured are the K_d , the effective

observation volume V_{eff} and the relative concentrations of bright and dark receptors and ligands. However, the extent of labeling of the interaction partners is usually unknown. While it is safe for BF to assume that it has either one or no ligand attached, streptavidin can have up to 6 labels attached per monomer (number of lysines plus N-terminus). Although the extent of labeling in the case of TMRSA is given by the manufacturer as 4.2 mole dye per mole streptavidin, there is no information available about the exact distribution of the labels. However, I will show in the simulations that the distribution of labels on TMRSA plays a minor role in our measurements in which the TMRSA concentration is kept constant, and the assumption of an average count rate for TMRSA is justifiable.

The CCF of Eq. 4.25 contains several contributions: First, the first three sums in the numerator are contributions of particles that contain either only ligand fluorophores or only receptor fluorophores. These contributions are similar to the autocorrelation of these particles and are caused by the cross-talk of the signal into both detectors. Second, the fourth sum in the numerator is the contribution of particles that contains both fluorophores of ligands and receptors and represent actual binding interactions. The contribution of the different particles depends solely on the product of their fluorescence yields in the two detectors. Thus the condition for a successful distinction between the different contributions to the CCF is only that $\tilde{\eta}_{RL}^g \tilde{\eta}_{RL}^r$ is sufficiently different from $\eta_L^g \eta_L^r$, $\eta_R^g \eta_R^r$, and $n^2 q_L^2 \eta_L^g \eta_L^r$. This implies that even when the same label is used on both ligand and receptor, a distinction is possible between the different contributions to the CCF. This is provided the fluorescence characteristics of the complex are different from the characteristics of the ligand and receptor alone (see [60]).

4.2.4 Calculations of SW-FCCS limits

For calculations of the K_d limits, determined with SW-FCCS, the ratio R was calculated in dependence of different parameters. Since the solution for the binding curve (and the detection threshold R) is constant for constant ratios of L_t/R_t and

K_d/R_t , all results are given in terms of these dimensionless parameters.

From Eq. 4.23, the ratio R must be at least 1 to allow for the distinction between positive and negative control. Table 4.2 shows the maximum values for K_d/R_t where $R = 1$ and reports the corresponding value of L_t/R_t where this maximum is reached. With the knowledge that FCS measurements can be performed at fluorophore concentrations between about 0.1 nM and 1 μ M, one can directly calculate possible K_d s accessible by this method and the ideal receptor and ligand concentrations to be employed. In these calculations it was assumed i) a standard deviation of $\Delta = 10\%$ for all measurements; ii) quenching upon binding is always equal in both detection channels; and iii) there is no quenching for negative controls. Condition i) was found to be generally fulfilled in the measurements. In FCS the amplitude can often be determined with a much lower standard deviation. Condition ii) might improve or worsen the resolution limit since it can result in larger or smaller differences for the fluorescence yield products for the different species. Condition iii) would in general worsen the resolution limit since more quenching means lower signal-to-noise ratio in the SW-FCCS measurements.

One has to differentiate between two different cases:

- 1) If $L_t/R_t \geq 1$, then $R_t^{\max} = R_t/L_t \times 10^{-6}\text{M}$ and $R_t^{\min} = R_t/L_t \times 10^{-10}\text{M}$.
- 2) If $L_t/R_t < 1$, then $R_t^{\max} = 10^{-6}\text{M}$ and $R_t^{\min} = 10^{-10}\text{M}$.

The maximum and minimum K_d s can be calculated by

$$K_d^{\max} = \frac{K_d}{R_t} R_t^{\max} \quad (4.27)$$

$$K_d^{\min} = \frac{K_d}{R_t} R_t^{\min} \quad (4.28)$$

4.3 Materials and Methods

The SW-FCCS optical setup has already been described in chapter 2. The filters used for experiments here were D1: 505DRLP, D2: 560DRLP, F2: 510AF23 (green channel) and F3: 580DF30 (red channel). Calibrations of the setup were

performed with fluorescein (Molecular Probes, Eugene, USA) in both channels and the geometry parameter K , describing the ratio of the extension of the confocal volume along compared to perpendicular to the optical axis, was fixed between 2–4 for the curve fittings, depending on the calibrations.

TMRSA (Molecular Probes, Eugene, USA) was diluted to 12 sample solutions of 5 nM. Each solution was incubated at least 1/2 hour with increasing concentrations of BF (Molecular Probes) from 0–50 nM to obtain mixtures with BF/TMRSA ratios between 0–10. Negative controls at the same concentration ratios were prepared by saturating all binding sites of TMRSA with 1 μ M of excess D-biotin (Amersham Biosciences Ltd., Singapore) before adding BF. All solutions were prepared in PBS at pH 7.4 (Sigma-Aldrich, Singapore).

4.4 Results and Discussion

To study the influence of the dissociation constant, impurities, cross-talk and labeling ratio, the following assumptions are made if not stated otherwise:

- i) Interactions have a 1:1 stoichiometry. Since FCS cannot resolve interactions of molecules with similar masses, especially when there is no accompanying change in fluorescence yield.
- ii) All fluorophores have the following fluorescence yields: $\eta_L^g = 27,000$ Hz, $\eta_L^r = 3,000$ Hz, $\eta_R^g = 3,000$ Hz, $\eta_R^r = 27,000$ Hz.
- iii) Receptors and ligands carry only one fluorophore.
- iv) No quenching occurs for the fluorophores upon binding: $q_L = q_R = 1$.
- v) All receptors and ligands are active and carry one fluorophore (no impurities).

The following calculations will determine the influence of each of these conditions on the CCF by varying each parameter at a time, while keeping the others at their values stated here.

4.4.1 Influence of the dissociation constant on SW-FCCS

The amplitudes of the CCF were calculated as a function of ligand receptor ratio L_t/R_t for dissociation constants $10^{-15} \text{ M} < K_d < 10^{-7} \text{ M}$ (Fig. 4.1). The negative control decreases steadily with an increasing ratio L_t/R_t since the receptor concentration remains constant and the ligand concentration increases. The CCF for the negative control changes only due to the cross-talk of the ligand in the two channels. This behavior is similar to FCS (Eq. 4.26).

The CCFs of the positive control have two different parts. In the first part where $L_t/R_t < 1$ during unsaturated binding, not every receptor has one ligand bound and the amplitude of the CCF changes due to increasing binding. As soon as all receptor binding sites are occupied, at saturating binding conditions, contributions to the CCF are made by increasing numbers of free ligands. Again, the increase in free ligand concentration leads to a decrease of the CCF amplitude. The CCF converges to the negative control due to cross-talk of the ligand in the two channels. This separation of the CCF for positive and negative control is obvious for small K_d s and can also be seen in the experimental data (Fig. 4.1). For increasing K_d s, i.e. smaller affinities, this difference vanishes slowly and allows the maximum K_d to be measured (Fig. 4.2).

4.4.2 Influence of impurities on SW-FCCS

Different impurities can be present in a sample. The receptor can be either active or inactive, and the receptor can either be fluorescence labeled or unlabeled. To make the influence of the individual impurities clear, it is assumed that only one impurity is present at a time and represents 50% of the total ligand or receptor concentration. The graphs for two different K_d s (10^{-15} M and 10^{-9} M) and the three kinds of impurities are shown in Fig. 4.3.

Impurities, in general, lead to a reduction in the difference between negative and positive control and thus reduce the sensitivity of the method (see Table 4.2). Fluorescent but inactive ligands and receptors shift the apparent separation

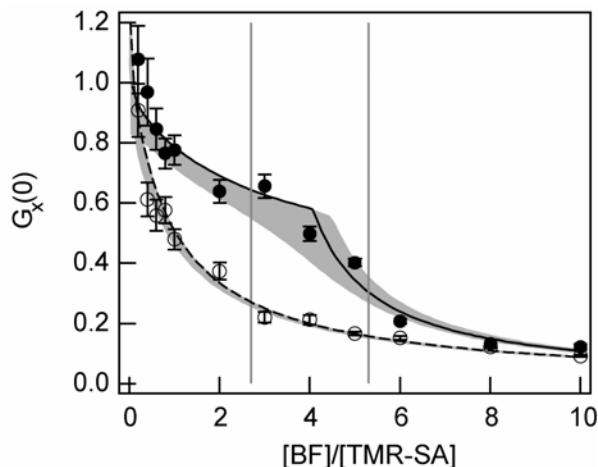


Figure 4.1: Binding experiments of BF to TMRSA. Depicted is the amplitude of the cross-correlation function versus the BF to TMRSA concentration ratio. The concentration of TMRSA was 5 nM in all experiments. The positive control (filled circles) is shown with the best fitting model as solid curve ($V_{eff} = 0.42$ fl; $*L_t^+ = 0.9$, $*L_t^- = 0.1$; $*R_t^+ = 0.7$; $*R_t^- = 0.1$; ${}^\circ R_t^+ = 0.2$). The negative control (empty circles) is shown with the best fitting model as the dashed curve ($V_{eff} = 0.33$ fl; $K_d = 10^{-15}$ M; $*L_t^+ = 0.9$, $*L_t^- = 0.1$; $*R_t^+ = 0.7$; $*R_t^- = 0.1$; ${}^\circ R_t^+ = 0.2$). The shaded areas show the borders of the models which can fit the data with a change of χ^2 of less than 50% parameters have the following ranges: $V_{eff} = [0.33 - 0.42]$ fl; $K_d = [10^{-15} - 5 \times 10^{-10}]$ M; $*L_t^+ = 0.9$, $*L_t^- = 0.1$; $*R_t^+ = [0.7 - 0.85]$; $*R_t^- = [0.0 - 0.1]$; ${}^\circ R_t^+ = [0.1 - 0.2]$. The two vertical grey lines delimit the $[BF]/[TMRSA]$ concentration region in which the detection threshold for binding $R \geq 1$ (Eqs. 22 and 23).

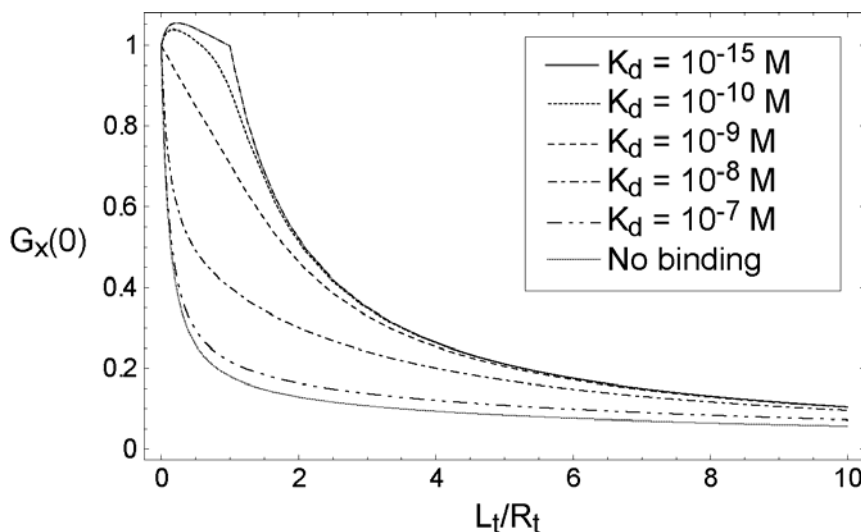


Figure 4.2: Influence of K_d on the CCF. The CCF amplitude is shown against the ligand/receptor concentration ratio. The curves were calculated for a standard fluorophore pair (fluorescence yields $\eta_L^g = 27,000$ Hz, $\eta_L^r = 3,000$ Hz, $\eta_R^g = 3,000$ Hz, $\eta_R^r = 27,000$ Hz; binding stoichiometry 1:1; no quenching of ligand and receptor i.e. $q_L = q_R = 1$).

of unsaturated binding to saturated binding at higher or lower values of L_t/R_t , respectively, and thus lead to misinterpretation of binding stoichiometries. In addition, for increasing concentrations of bright non-active ligands, the initial slope of the binding curve becomes steeper (Fig. 4.3 A).

Dark but active ligands and receptors have almost no influence on the point of separation of unsaturated to saturated binding. However, dark but active receptors change the initial slope of the CCF and thus its amplitude. From the experimental data in Fig. 4.1, the strong initial decrease of the CCF amplitude can be explained by impurities that are either bright, inactive ligands or dark, active receptors.

Dark inactive impurities shift the point of separation of unsaturated to saturated binding and influence the absolute amplitudes. Due to the different influences of the impurities it is theoretically possible to analyze their fractions from experimental data. But under experimental conditions, it will largely depend on the signal-to-noise ratio and the exact receptor or ligand labeling conditions.

4.4.3 Influence of cross-talk and quenching on SW-FCCS

Cross-talk is a serious problem in FCCS and SW-FCCS since it increases the contributions of the single-labeled species and reduces the difference between the fluorescence yield products of single- and double-labeled species. The influence of cross-talk of the ligand fluorophores into the channel for the detection of the receptor fluorophore on the binding curves is shown in Fig. 4.4. The question for SW-FCCS is therefore, how large can cross-talk, i.e. overlap between emission spectra, be without compromising binding measurements. The answer depends on the binding affinity measured. Fig. 4.5 depicts the values for K_d/R_t and L_t/R_t versus the percentage of cross-talk of either the ligand fluorophore, the receptor fluorophore, or both fluorophores simultaneously. 50% cross-talk means that both detection channels detect the same amount of fluorescence from a fluorophore. Thus, in cases with more than 50% cross-talk of one of the fluorophores it would be better to measure with a single detector. From these graphs one can directly

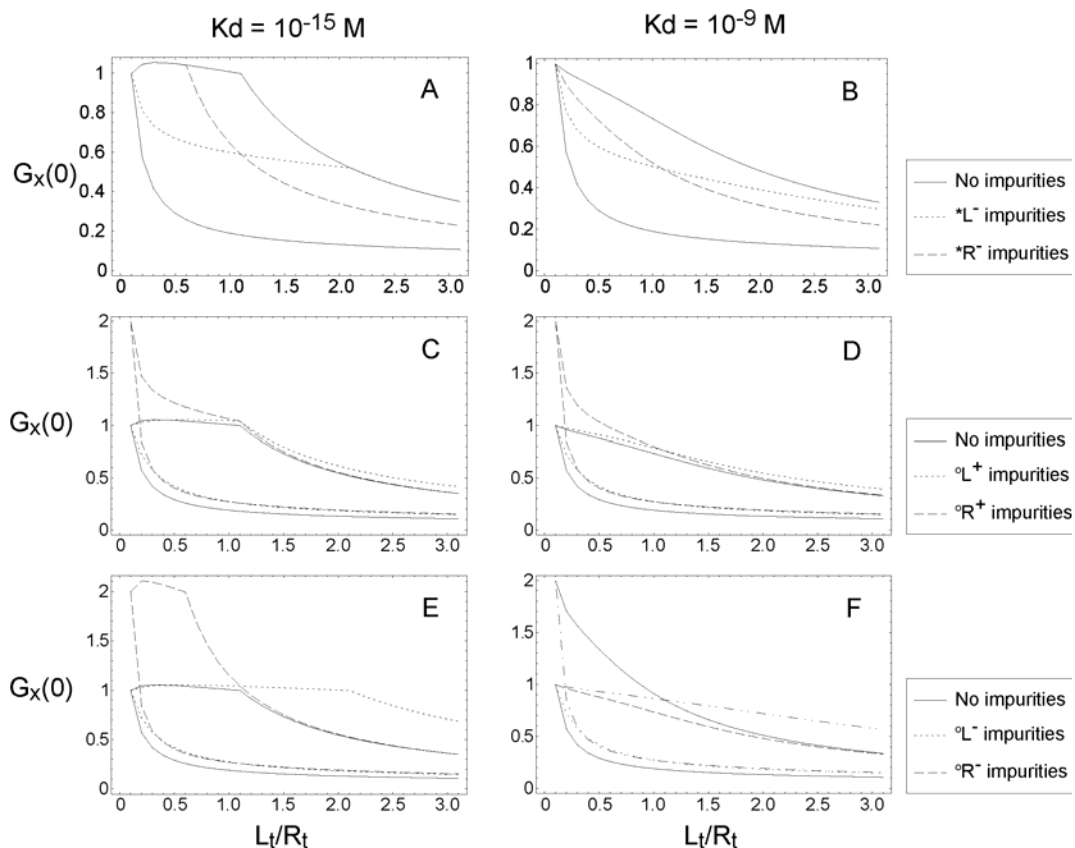


Figure 4.3: Influence of impurities on the CCF. The amplitude of the CCF is shown versus the ligand/receptor concentration ratio. The curves were calculated for a standard fluorophores pair (fluorescence yields $\eta_L^g = 27,000$ Hz, $\eta_L^r = 3,000$ Hz, $\eta_R^g = 3,000$ Hz, $\eta_R^r = 27,000$ Hz; binding stoichiometry 1:1; no quenching of ligand and receptor $q_L = q_R = 1$) and for two different K_d s (A, C, E) $K_d = 10^{-15}$ M and (B, D, F) $K_d = 10^{-9}$ M) with (A, B) bright inactive impurities. (C, D) dark active impurities. (E, F) dark inactive impurities. Curves for calculations assuming no impurities are shown as solid lines. Curves for ligand impurities are shown as dotted lines. Curves for receptor impurities are given as dashed lines.

evaluate whether a measurement of an expected K_d is possible by calculating the maximum measurable dissociation constant K_d^{\max} from the values of K_d/R_t and L_t/R_t at the measured level of cross-talk.

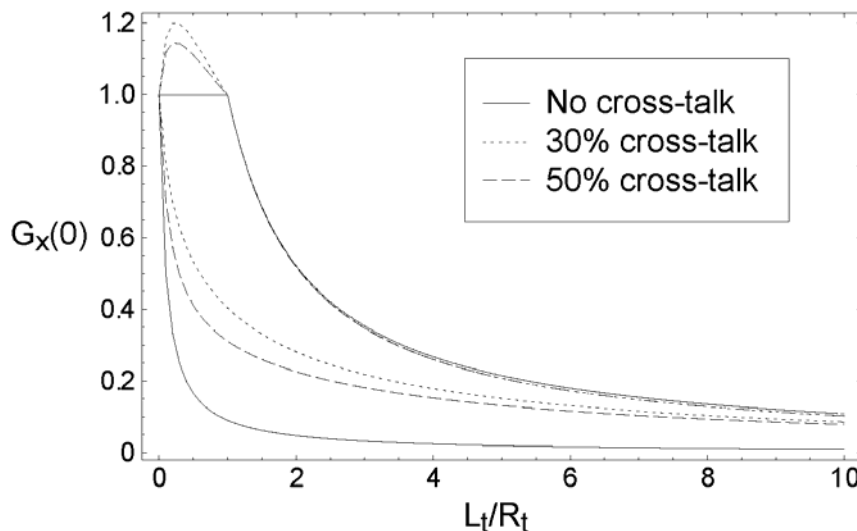


Figure 4.4: Influence of cross-talk on the CCF. The CCF amplitude is shown versus the ligand/receptor concentration ratio. The curves were calculated for three different levels of cross-talk of the ligand fluorophores into the channel of the receptor fluorophores (fluorescence yield $\eta_L^g + \eta_R^r = 30,000$ Hz distributed over the two channels depending on cross-talk). The receptor was assumed to have a cross-talk of 10 ($\eta_R^g = 3,000$ Hz, $\eta_R^r = 27,000$ Hz;). The binding stoichiometry is 1:1 and no quenching of ligand and receptor were used $q_L = q_R = 1$.

4.4.4 Influence of receptor labeling on SW-FCCS

The number of labels per receptor and ligand can have a strong influence on the correlation curves in FCS as well as in FCCS. This is due to the fact that the ACF amplitude is proportional to the square of the fluorescence yield per molecule. Similarly, the CCF amplitude is proportional to the product of the fluorescence yield per molecule in the two detection channels. Thus, a molecule with two labels instead of one contributes four times more to the ACF than a molecule with only one label.

The influence of labeling on measurements has to be determined for every individual system. This is often a problem since the exact distribution of labels is not known and is usually not available for commercial products. Especially

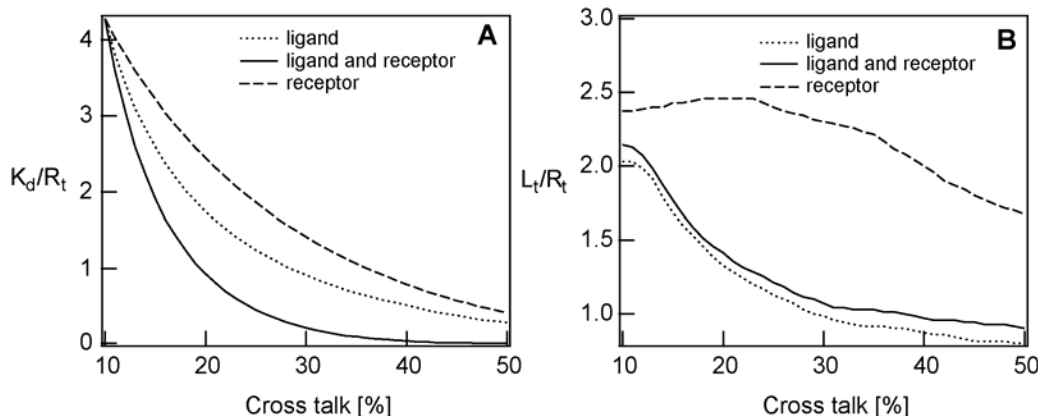


Figure 4.5: Sensitivity of SW-FCCS depending on increasing cross-talk of ligand fluorophores (dotted lines), receptor fluorophores (dashed lines), or both fluorophores simultaneously (solid lines). For these calculations a 1:1 binding stoichiometry and no quenching upon binding were assumed. For the ligand and receptor curves the cross-talk of one fluorophore was fixed at 10% while the cross-talk of the other fluorophore was varied between 10 and 50%. At 50% cross-talk for a fluorophore, the intensities detected in the two detection channels are equal. For the ligand and receptor curves the cross-talk of both fluorophores was varied simultaneously between 10 and 90%. The fluorophores were assumed to result in 30,000 cpm over all detection channels. (A) The values of K_d/R_t are depicted versus percentage of cross-talk. (B) The values of L_t/R_t are depicted versus percentage of cross-talk. Maximum measurable K_d s are calculated from the data.

proteins that are common to have several possible labeling sites, are usually not fully labeled, since the extent of labeling increases the probability of precipitation of the protein. However, two conditions help to reduce this influence. Firstly, the ligand is usually well-known and labeling can be controlled so that a single label is attached to this molecule (e.g. peptide synthesis, small molecule ligands, ligands with a fluorescent protein attached). Secondly, the concentration of the receptor R_t that contains an unknown distribution of labels can be held constant while the ligand concentration L_t is varied. In this case, it is shown that the influence of the unknown label distribution is relatively small and affects the detection of binding only marginally.

For this purpose, the expected amplitudes of the CCF were calculated for two K_d s (10^{-15} and 10^{-9} M) and for a receptor that has either 2 or 4 possible binding sites and thus can carry either 1 or 2 or 1–4 fluorophores, respectively. All fluorophores were assumed to be independent of binding site, contributing

equally to the fluorescence signal. Although this assumption is in general not true, the calculations showed that the extent of labeling of the receptor, thus its fluorescence yield did not influence the CCFs strongly. All calculations were performed for standard fluorophores where the ligands carry only one fluorophore while the receptors can carry several fluorophores. The results of these calculations are shown in Fig. 4.6.

From Fig. 4.6 it is shown that the influence of labeling on the CCF is strongest at low ratios of L_t/R_t . But this is as well the region where the distinction between positive and negative control is most difficult since the differences are small. This effect can be seen especially well in the calculations for a $K_d = 10^{-9}$ M where at $L_t/R_t < 1$, the difference between positive and negative control is very small. In the region $1 < L_t/R_t < 4$ where the differences between positive and negative control are large, the influence of the labeling distribution is small.

4.4.5 SW-FCCS with spectrally similar fluorophores on the streptavidin-biotin system

Binding of BF to TMRSA was measured at constant TMRSA concentration (5 nM) and increasing BF concentrations. The resulting CCF amplitudes are depicted in Fig. 4.1 as function of $[BF]/[TMRSA]$. The background corrected intensities detected in the different channels are given in Table 4.1 for solutions of 1 nM. The number of particles per observation volume in our system is 0.22 ± 0.01 . From this value, all necessary numbers of cpm η_s^i were calculated.

At low ratios of $[BF]/[TMRSA]$, the binding curve decreases until a ratio between 3–4 where full binding is attained and stoichiometry of binding is determined. Beyond this point, the binding curve decreases steeply towards the negative control due to the saturation of binding sites of streptavidin. A proper fit of the data is difficult since Eqs. 4.25 and 4.26 contain too many unknown parameters. In particular, the unknown labeling ratio of streptavidin, and the uncertainty in the purity of the sample. Thus, two assumptions are made: 90% of the ligand

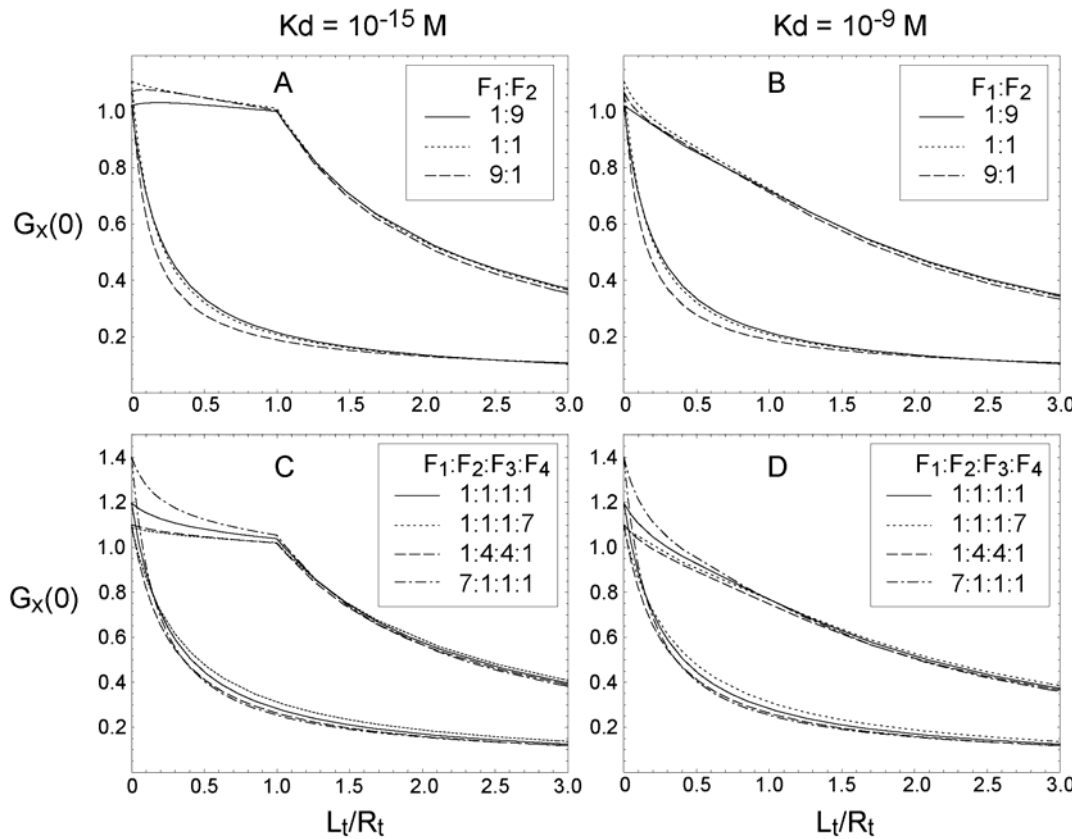


Figure 4.6: The influence of receptor labeling on the cross-correlation amplitudes. The graphs depict the cross-correlation amplitudes for a standard fluorophore pair (fluorescence yields $\eta_L^g = 27,000$ Hz, $\eta_L^r = 3,000$ Hz, $\eta_R^g = 3,000$ Hz, $\eta_R^r = 27,000$ Hz; binding stoichiometry 1:1; no quenching of ligand and receptor $q_L = q_R = 1$). The ligand carries one fluorophore and the receptor can carry either 1 – 2 fluorophores (A, B) or 1 – 4 fluorophores (C, D). The ratios of receptors carrying 1 to n fluorophores are given in the legends as $F_1 : F_2 : \dots : F_n$. (A) and (C) depict the curves at a $K_d = 10^{-15}$ M. (C) and (D) depict the curves at a $K_d = 10^{-9}$ M.

consists of active labeled ligands and 10% are bright inactive impurities. This is in line with the 90% purity level given by the manufacturer. Secondly, TMRSA has an average fluorescence yield as measured in Table 4.1, and the distribution of labels is disregarded.

With these two assumptions and all the fluorescence yields measured, the data is modeled as shown in Fig. 4.1. The best fit with the lowest χ^2 has the following values: $\{V_{eff} = 0.33 \times 10^{-15}$ L; $K_d = 10^{-15}$ M; bright active receptor: 0.7; bright inactive receptor: 0.1; dark active receptor: 0.2}. This confirms the simulations which showed that dark active receptor (and bright inactive ligands as fixed by us) is responsible for the steep initial slope in the binding curve. To give an idea of how accurate the fitting parameters are, the parameters are varied to determine the minimum and maximum values without changing the χ^2 value by more than 50%. The range of the models are indicated by the shaded area in Fig. 4.1. The parameter ranges are: $V_{eff} = [0.33 - 0.42] \times 10^{-15}$ L; K_d : $[10^{-15} - 5 \times 10^{-10}]$ M; bright active receptor = $[0.7 - 0.85]$; bright inactive receptor = $[0.0 - 0.1]$; dark active receptor = $[0.1 - 0.2]$. The effective volume V_{eff} is close to the expected value of 0.37×10^{-15} L, as calculated from the 0.22 particles per observation volume. The K_d has a very large range due to the small differences for the binding curves at low K_d s. As shown in Fig. 4.2, the difference in the binding curve between a $K_d = 10^{-15}$ M and a $K_d = 10^{-10}$ M is smaller than between a $K_d = 10^{-10}$ M and a $K_d = 10^{-9}$ M. This is mainly due to the fact that the concentrations measured is in the nanomolar range, which is far away from the actual K_d . The fractions for the bright active receptors compared to the bright inactive and the dark active receptors are slightly low. Only 70 – 85% of the receptors are bright and active. However, the manufacturer claims only 90% of the labeled sample is active.

The model shows systematic deviations from the data to smaller values at low [BF]/[TMRSA] ratios. This could be due to the fact that the distribution of labels on the receptor is not taken into account. As shown in Fig. 4.6 it is at the low ligand to receptor ratios that the curves deviate most strongly from curves that

assumed one average label per receptor.

Molecule	$I^g (\eta^g) / \text{Hz}$	$I^r (\eta^r) / \text{Hz}$	q_s
Flu	10,700 (48,600)	2,700 (12,300)	-
TMR	< 50 (< 300)	800 (3,600)	-
BF	5,700 (25,900)	1,200 (5,500)	0.25
TMRSA	300 (1,400)	1,500 (6,800)	1.0
QR	700 (3,200)	15,700 (71,400)	1.0
QD655	500 (2,300)	43,000 (195,500)	1.0

Table 4.1: Fluorescence intensities of the different particles in the detection channels g and r for standard solutions of 1 nM. The average number of molecules per observation volume in our setup for a 1 nM solution is 0.22 ± 0.01 . From this number the values in brackets, the cpm values are calculated. The quenching factor for the different molecules is given by q_s .

4.4.6 Comparison of sensitivities of different fluorophore pair systems

To give a general idea of how different fluorophores influence SW-FCCS measurements, the values are compared for two fluorophore pairs that represent different extremes: fluorescein-quantum red (Flu-QR) and fluorescein-tetramethylrhodamine (Flu-TMR). The system with Flu-QR can be excited at 488 nm, and due to the large Stokes shift of QR (emission mainly at 670 nm) the emission of the two fluorophores can be easily separated. Binding measurements have been shown in chapter 3 with SW-FCCS on this binding system. The emission maxima of Flu-TMR are not well separated and excitation at 488 nm is not as efficient for TMR.

Table 4.2 shows the calculated maximum values of K_d/R_t and the corresponding value of L_t/R_t for these two fluorophore pairs. The values have been calculated from the cpm data of Table 4.1 and Eqs. 4.23, 4.25 and 4.26 for different conditions that show extreme values of 80% quenching of either ligand or receptor, and for 20% bright non-active impurities of both ligand and receptor. These conditions were chosen to be representative of typical situations.

In the Flu-QR system, the ratio K_d/R_t ranges from 0.77 to 377 with values

of L_t/R_t of 1.99 and 113, respectively. This translates into a measurable K_d^{\max} between 0.4–3.3 μM and shows that this system can be used for the measurement of even weak interactions. In the case of Flu-TMR, the ratio of K_d/R_t can be well below 1 and in general for 1:1 binding stoichiometry it is between 0.02 and 0.22 with L_t/R_t between 0.47 and 1. Therefore, the measurable K_d^{\max} is in the range of 20–220 nM or lower. For a binding stoichiometry of 1:4, the values increase to $K_d/R_t = 4.5$ at $L_t/R_t = 5.5$, resulting in a measurable K_d^{\max} of 0.8 μM .

Stoich- iometry	No quenching no impurities		80% quenching of ligand (green)		80% quenching of receptor (red)		R impurity 20% L impurity 20%	
	L_t/R_t	K_d/R_t	L_t/R_t	K_d/R_t	L_t/R_t	K_d/R_t	L_t/R_t	K_d/R_t
Flu-QR								
1:1	41	43.5	1.99	0.77	39.2	9.0	33	22.0
4:1	113	377	33	33	85.0	153.0	104.0	224.0
Flu-QR								
1:1	0.47	0.22	0.85	0.02	1.0	0.04	0.61	0.03
4:1	5.5	4.5	2.9	1.2	5.3	4.5	4.9	2.5

Table 4.2: Maximum K_d/R_t values with corresponding L_t/R_t values, for a value of the detection threshold $R = 1$. Values are given for two fluorophore combinations: BF/QR and BF/TMRSA. With these values maximum and minimum detectable K_d s can be calculated.

4.4.7 Possible fluorophore pairs for SW-FCCS

The preceding discussion shows that ideal fluorophore pairs for SW-FCCS minimize cross-talk due to large differences in Stokes shift but have strong absorptions at the same wavelength. This is suitable for QDs and energy transfer dyes that can be excited at 488 nm but have largely different emission spectra. However, these labels suffer from several drawbacks: QDs are large and often of similar or larger size than the labeled molecule; aggregation may also occur (see chapter 3). Therefore other labels, preferably small organic dyes or bright proteins can be applied. The choice of fluorescein-TMR is a borderline case and the improvement over FCS with two of the same labels is small. This is mainly due to the quenching of fluorescein upon binding and the limited absorption of TMR at 488 nm. However, new commercial fluorophores with large Stokes shifts could offer new perspectives for SW-FCCS. Possible candidates are MegaStokes dyes [89] that can

be excited at 488 nm, but have emission wavelengths between 530 and 670 nm. These fluorophores could be paired with standard fluorophores that can be excited at 488 nm (fluorescein, GFP). A problem with these dyes is that their emission spectra get broader with longer emission wavelength, possibly increasing problems of cross-talk. Another possibility would be combinations of fluorescent proteins, several of which can be excited pair wise at 488 nm but emit at different wavelength. For instance, green and red fluorescent proteins can be excited efficiently at 488 nm and FCS curves can be measured efficiently *in vivo* as shown in chapter 5, Table 5.2. Fluorescent proteins would not only offer the advantage of *in vivo* measurements but also the precise control of labeling ratio. Thus, eliminating the need to determine fluorophore distributions on the interacting partners. With these different fluorophore combinations, SW-FCCS could be used for screening and the determination of dimerization of proteins *in vivo*.

4.4.8 A comparison between FCS and SW-FCCS

In general, binding can be measured by fluorescence spectroscopy if the fluorescence yield changes upon binding. However, if there are no changes in fluorescence yield, binding can be measured using FCS. For a stoichiometry unequal to 1:1, binding can be determined by a change in amplitude of the ACF [47]. Otherwise binding can be measured by a change in the diffusion coefficient under the condition that the mass change upon binding is at least a factor 4–8 [53, 137]

In cases of 1:1 binding with mass changes smaller than a factor 4–8 and no accompanying fluorescence yield changes, binding can no longer be measured by FCS. To measure binding under these conditions, both binding partners have to be labeled. This is done by using either the same label for both binding partners and detecting the fluorescence in one channel for autocorrelation (FCS). Alternatively, it is achieved by using different labels per molecule and detected in a different channel. The detection channels can then be cross-correlated (SW-FCCS).

The contribution of a molecule to the ACF depends on the square of the

fluorescence yield (η_s^2) in the single detection channel. In the best case a complex of a ligand and receptor would thus have double the fluorescence yield and contribute 4 times as much to the ACF than the unbound particles. Table 4.1 reports the fluorescence yield products for the TMRSA and BF system for a 1:1 stoichiometry. For higher stoichiometries the comparison is more favorable. The fluorescence yield product for the two detection channels of the bound TMRSA-BF complex ($\eta_c^g \eta_c^r$) is more than 4 times larger than that for BF ($\eta_s^g \eta_s^r$). Since BF is quenched by 75% upon binding, an FCS experiment with both interaction partners labeled with BF would increase the square of the fluorescence yield (η_c^2) of the single detection channel by only a factor of $1.25^2 \approx 1.56$. Therefore, SW-FCCS is a definite improvement over FCS as it increases the contribution of the bound complex almost 3 times more than FCS. However, when comparing $\eta_c^g \eta_c^r$ of the TMRSA-BF complex to $\eta_s^g \eta_s^r$ of TMRSA, the improvement is much less than a factor of 4. In this case an FCS experiment with double-labeling using TMR would have a better signal than SW-FCCS using TMR and fluorescein. Responsible for this effect is the strong quenching by 75% of fluorescein upon binding. Therefore, one has to choose carefully the fluorophore pairs used in a SW-FCCS experiment, so that an improvement over FCS is achieved. However, the extension of labels for SW-FCCS to organic dyes with only narrowly separated emission spectra makes a wide range of labels accessible for experimental optimization.

4.5 Conclusion

This chapter investigates the resolution of SW-FCCS by experiments conducted with fluorescent probes with similar emission wavelengths. This extends the applicability of SW-FCCS from the previously reported long Stokes shift fluorophores (in chapter 3) to the more routinely used small organic dyes.

The theory of SW-FCCS has been extended from chapter 3 for equilibrium binding of receptor-ligand at 1:1 binding stoichiometry to 1:4 stoichiometry. The

theory takes into account the receptor and ligand impurities and the fluorophore labeling ratio. It is also defined that for SW-FCCS to resolve binding, the CCF amplitudes of the binding curve and the negative control will have to differ by at least six standard deviations. Fluorescent probes with similar excitation and emission spectra, fluorescein and tetramethylrhodamine, were characterized on the setup with higher percentage of cross-talk obtained in both channels.

Receptor-ligand binding between TMRSA and BF has been measured on SW-FCCS and the binding curve was fitted with the theoretical model to obtain the percentages of receptor impurities and a K_d close to the literature value [120]. Various parameters such as cross-talk, impurities, fluorophore labeling ratios and dissociation constants influencing the binding curves have been simulated. The resolution of binding for TMRSA/BF is lower than that compared with QR/BF, a fluorophore pair with larger difference in emission wavelengths and higher fluorescence yields. However, it is shown that even for measurements at a single concentration ratio between receptor and ligand, differences of more than 6 standard deviations in the CCF amplitude can be reached. When comparing SW-FCCS with FCS, the capability of the methods to resolve binding will depend on the contribution of the fluorescence yields to the CCF or ACF respectively.

It has been shown that SW-FCCS can be applied to excitation of fluorophores that have only small differences in emission spectra. Although, depending on the fluorophores, the detection of interactions can be restricted to very low dissociation constants, i.e. very strong binders, (~ 1 nM), the method is applicable in most cases to dissociation constants up to about $1 \mu\text{M}$. Thus, this study raises the possibility of extending the method to the excitation of more than two fluorophores for multicolor detection of multiple binding partners (see chapter 5). This is an important step towards simultaneous multiplex detection of biomolecular interactions in high throughput screening or complex signaling networks in living cells.

Chapter 5

Multicolor SW-FCCS

5.1 Introduction

The resolution limit of SW-FCCS was determined with respect to binding constants, sample impurities, cross-talk and quenching in chapter 4. It was shown that it is possible to achieve fluorescence cross-correlation with spectrally similar fluorophores using single laser wavelength excitation. This raises the question if SW-FCCS can be extended to more than two colors to detect higher order molecular interactions. Biomolecular interactions involving more than two molecular species have been elucidated using fluorescence techniques. Colocalization analysis [90, 138] and image correlation analysis [72, 139] by confocal microscopes compare images with differently labeled molecular species and calculate the image superposition or correlation functions. Although interacting molecules localize to the same site, the overlap of images of molecules at the same position does not necessarily prove mutual interactions. Recently, other methods with single molecule sensitivity have been developed, such as triple-color FRET [140] and triple-color coincidence fluctuation analysis [83], for the probing of higher order molecular complexes. However, triple-color FRET depends on the proximity of labeling sites for efficient energy transfer upon interacting. Also, triple-color coincidence analysis uses two-photon excitation that requires expensive laser systems.

Moreover, these methods do not provide dynamic information of the molecular interactions as compared with correlation functions.

In this chapter, an extension of dual-color SW-FCCS to triple-color or multicolor SW-FCCS is described. Using a single laser wavelength to excite up to three differently emitting dyes simultaneously, the binding of green ligand biotin-4-fluorescein (BF) and yellow ligand R-phycoerythrin biotin (BPE) to red receptor Alexa Fluor 647-R-phycoerythrin-streptavidin (AXSA) is measured. The theory is formulated to explain the pair-wise cross-correlations green \times red ($G_{gr}(\tau)$), yellow \times red ($G_{yr}(\tau)$) and green \times yellow ($G_{gy}(\tau)$) for this system. It is shown that even with a higher amount of cross-talk between three differently emitting fluorescent labels, SW-FCCS is able to discriminate bound complexes from free reactants by more than 6 standard deviations difference in the cross-correlation amplitudes. The capability of distinguishing trimers, dimers and monomers regardless of their molecular weight, when performed with appropriate negative controls, opens up new possibilities of studying higher order interactions in complex molecular systems.

5.2 Theory

5.2.1 Cross-correlation of triple species

The theory presented here adapts the theory described from chapter 4 to a three component binding system. Assume a receptor-ligand system consisting of R , a red fluorescent receptor with multiple binding sites for one ligand, and L_g and L_y , the ligand that is either labeled with a green or yellow emitting fluorophore. Considering a solution of receptor and ligands, free ligands L will bind with free receptors R to form complex RL_n at equilibrium binding where n is the number of bound ligands on R . Assume that each complex formed consists of one receptor with several ligands specifically bound, therefore excluding oligomerization of this receptor. The binding scheme has already been described in chapter 4, Eq. 4.1.

Assuming that each binding site has the same affinity. If the multiplicity of the binding sites is disregarded, the dissociation constant K_d for each individual binding site is then given by Eq. 4.2 in chapter 4. To take account of the multiple binding sites per receptor, binomial coefficients are introduced to describe the possibility of n ligands binding to n_t binding sites [135]. The concentrations of free receptors and ligands, R_f and L_f , are thus related to the total concentrations of receptor R_t and ligand L_t minus the sum of all bound receptors and ligands, respectively.

$$R_f = R_t - \sum_{n=1}^{n_t} \binom{n_t}{n} RL_n \quad (5.1)$$

$$L_f = L_t - \sum_{n=1}^{n_t} n \binom{n_t}{n} RL_n \quad (5.2)$$

The concentrations of the complexes RL_n , L_f and R_f at binding equilibrium can then be numerically determined by simultaneously solving Eq. 4.2, 5.1 and 5.2.

The total concentration of ligand L_t consists of the ligands L_g and L_y . The probability of encountering either ligand L_g or L_y to form a complex with a receptor is given by their mole fractions

$$f_{l_g} = \frac{L_g}{L_t} \quad (5.3)$$

$$f_{L_y} = \frac{L_y}{L_t} = 1 - f_{l_g} \quad (5.4)$$

Consider a receptor with n_t binding sites and n fluorescent ligands bound of which n_g are L_g ligands and n_y are L_y ligands ($n_g \leq n \leq n_t$). In this case, the number of possibilities of how to distribute firstly n ligands over n_t binding sites and secondly n_g ligands L_g to the n bound sites has to be taken into account. The distribution of n_y ligands L_y to the $n_y = n - n_g$ remaining binding sites has

then only one possibility. The concentration of a complex with n bound ligands becomes

$$RL_{(n,n_g)} = \binom{n_t}{n} \binom{n}{n_g} f_{L_g}^{n_g} \cdot f_{L_y}^{n_y} \cdot RL_n \quad (5.5)$$

The first binomial coefficient describes the distribution of n bound ligands over the total number of binding sites n_t and the second coefficient is the distribution of L_g over the total number of bound ligands. Equations 5.1-5.5 will be used to calculate the cross-correlation amplitude as shown below.

The time dependent total fluorescence signal $F_i(t)$ in detection channel i is the sum of all fluorescent species ($s = L, R, RL$) contributing to the signal. It is determined by their fluorescence yields (often expressed as counts per molecule per second), and the time dependent number of particles $N_A V_{eff} C(t)$ in the effective observation volume V_{eff} . N_A is Avogadro's number and $C(t)$ represents the time dependent values of the averages L_f , R_f , or $RL(n, n_g)$ as defined in Eqs. 5.1, 5.2, and 5.5, respectively. All possible species that contribute with via cross-talk into the detection channels are taken into account.

$$\begin{aligned} F_i(t) &= F_R^i(t) + F_L^i(t) + F_{RL}^i(t) \\ &= N_A V_{eff} \left[\eta_L^i L_f(t) + \eta_R^i R_f(t) + \sum_{n=1}^{n_t} \sum_{n_g=1}^n \eta_{RL}^i RL_{(n,n_g)}(t) \right] \\ &= N_A V_{eff} \left[\begin{aligned} & \left(\eta_{L_g}^i f_{L_g} + \eta_{L_y}^i f_{L_y} \right) L_f(t) + \eta_R^i R_f(t) + \\ & \sum_{n=1}^{n_t} \sum_{n_g=1}^n \left(n_g q_{L_g} \eta_{L_g}^i + n_y q_{L_y} \eta_{L_y}^i + \eta_R^i \right) RL_{(n,n_g)}(t) \end{aligned} \right] \end{aligned} \quad (5.6)$$

The first term represents the total free ligands with different fluorescence yields η_{L_g}, η_{L_y} for ligands labeled with different fluorophores. The second term represents the free receptor and the third term denotes the complex itself with both types of ligands bound to the receptor where the fluorescence yield contribution of L_g and

L_y are proportional to the number of ligands bound i.e. n_g times L_g and n_y times L_y . Changes in fluorescence yields upon binding via processes such as quenching or FRET are taken into account by the factors q_{L_g}, q_{L_y} where $q = 1.0$ if there is no change in fluorescence yield. Assuming that the emission spectra do not undergo any shifts in wavelength, q_{L_g}, q_{L_y} are the same in all channels.

Since it is only interesting in observing relative changes in the cross-correlation amplitudes, the CCF is calculated at $\tau = 0$. The fluorescence yield factor is obtained by the product of fluorescence yields in the cross-correlated channels. It determines the weighting factor contributing from various species to the CCF amplitude respectively

$$\eta_L^{ij} = \eta_{L_f}^i \eta_{L_g}^j f_{L_g} + \eta_{L_y}^i \eta_{L_y}^j f_{L_y} \quad (5.7)$$

$$\eta_R^{ij} = \eta_R^i \eta_R^j \quad (5.8)$$

$$\eta_{RL(n,n_g)}^{ij} = \left(n_g q_{L_g} \eta_{L_g}^i + n_y q_{L_y} \eta_{L_y}^i + \eta_R^i \right) \quad (5.9)$$

$$\left(n_g q_{L_g} \eta_{L_g}^j + n_y q_{L_y} \eta_{L_y}^j + \eta_R^j \right) \quad (5.10)$$

By substituting Eq. 5.6 for two detection channels $i \times j$ (where $i \times j$ can be any combination pair of detection channels) into the CCF in Eq. 2.1, and assuming a 3D Gaussian illumination intensity profile, the CCF amplitude then becomes

$$G_{ij}^+(0) = \frac{\eta_L^{ij} L_f + \eta_R^{ij} R_f + \sum_{n=1}^{n_t} \sum_{n_g=1}^n \eta_{RL(n,n_g)}^{ij} RL(n,n_g)}{N_A V_{eff} \left[\begin{array}{l} \left(\eta_L^i L_f + \eta_R^i R_f + \sum_{n=1}^{n_t} \sum_{n_g=1}^n \eta_{RL(n,n_g)}^i RL(n,n_g) \right) \\ \left(\eta_L^j L_f + \eta_R^j R_f + \sum_{n=1}^{n_t} \sum_{n_g=1}^n \eta_{RL(n,n_g)}^j RL(n,n_g) \right) \end{array} \right]} \quad (5.11)$$

where the effective volume V_{eff} is experimentally determined.

The CCF for the negative control does not include binding of ligand to receptor therefore only cross-talk is contributing to the function

$$G_{ij}^-(0) = \frac{\eta_L^{ij} L_t + \eta_R^{ij} R_t}{N_A V_{eff} [(\eta_L^i L_t + \eta_R^i R_t) (\eta_L^j L_t + \eta_R^j R_t)]} \quad (5.12)$$

Equation 5.11 is based on the assumption that both L_g and L_y bind to R to form a trimer. But in the case where only one type of ligand is bound to R and the other remains free, the CCF amplitude will resemble the positive control function for the bound ligand and receptor and the negative control function for the free ligand. In this case there are two possible cases.

5.2.2 Case 1: $R + L_g + L_y \rightarrow RL_g + L_y$

In the case where all ligands binding to the red receptor R are green ligands L_g ($n = n_g$) and the yellow ligands L_y remain free, the probability of binding L_g becomes 1. The concentration of complex RL_g from Eq. 5.5 becomes

$$RL_{(n_g)} = \binom{n_t}{n_g} RL_{n=n_g} \quad (5.13)$$

All of the complexes formed consist of only RL_g , therefore there is no fraction of L_y contributing to the concentration of free ligands L_f after binding ($fL_y = 0$) nor to the formation of the complex RL_g . Instead, all of L_y ($= fL_y L_t$) remains as completely free ligands but still contribute to the CCF between $g \times r$ via cross-talk. These conditions are substituted into the CCF in Eq. 5.11 to obtain $G_{ij}(0)$ as a positive control for $g \times r$

$$G_{ij}(0) = \frac{\eta_{L_g}^{ij} L_f + \eta_{L_y}^{ij} L_y + \eta_R^{ij} R_f + \sum_{n_g=1}^n \eta_{RL(n_g)}^{ij} RL_{(n_g)}}{N_A V_{eff} \left[\begin{array}{l} \left(\eta_{L_g}^i L_f + \eta_{L_y}^i L_y + \eta_R^i R_f + \sum_{n_g=1}^n \eta_{RL(n_g)}^i RL_{(n_g)} \right) \\ \left(\eta_{L_g}^j L_f + \eta_{L_y}^j L_y + \eta_R^j R_f + \sum_{n_g=1}^n \eta_{RL(n_g)}^j RL_{(n_g)} \right) \end{array} \right]} \quad (5.14)$$

The first two terms in the numerator denote free L_g and total non-binding L_y respectively. The third and fourth terms represent the contribution from free R and complexes RL_g respectively. The fluorescence yield factors for species s

(where $s = L_g$ or L_y or R) are described by

$$\eta_s^{ij} = \eta_s^i \eta_s^j \quad (5.15)$$

$$\eta_{RL(n_g)}^{ij} = \left(n_g q_{L_g} \eta_{L_g}^i + \eta_R^i \right) \left(n_g q_{L_g} \eta_{L_g}^j + \eta_R^j \right) \quad (5.16)$$

Since there are no bound complexes formed between L_g and L_y or R and L_y , $G_{gy}(0)$ and $G_{yr}(0)$ represent the negative controls and any contribution from the RL_g receptor-ligand complexes comes via cross-talk.

5.2.3 Case 2: $R + L_g + L_y \rightarrow RL_y + L_g$

In the case where all ligands bound to red R are yellow L_y ($n = n_y$) and green L_g remain free, the probability of binding L_y becomes 1. Eq. 5.13 then refers to the concentration of complex RL_y formed and the cross-correlations can be derived from Eqs. 5.14–5.16 by exchanging indices g and y .

$$G_{ij}(0) = \frac{\eta_{L_y}^{ij} L_f + \eta_{L_g}^{ij} L_g + \eta_R^{ij} R_f + \sum_{n_g=1}^n \eta_{RL(n_g)}^{ij} RL(n_g)}{N_{A} V_{eff} \left[\begin{array}{l} \left(\eta_{L_y}^i L_f + \eta_{L_g}^i L_g + \eta_R^i R_f + \sum_{n_g=1}^n \eta_{RL(n_g)}^i RL(n_g) \right) \\ \left(\eta_{L_y}^j L_f + \eta_{L_g}^j L_g + \eta_R^j R_f + \sum_{n_g=1}^n \eta_{RL(n_g)}^j RL(n_g) \right) \end{array} \right]} \quad (5.17)$$

5.2.4 Application of theory to streptavidin-biotin binding system

The biochemical system presented here consists of the red AXSA receptor R with up to 4 specific binding sites ($n_t = 4$) for biotin ligand that is differently labeled with fluorescein (L_g) and R-phycoerythrin (L_y). In this case, the number of n_g and n_y ligands bound to R is varied from 0–4, such that the complex is always at full binding with all streptavidin binding sites occupied with biotin (see Materials and Methods). The CCFs for the positive and negative controls G_{ij} can be any permutations of detection channels in the green, yellow and red, corresponding to

the colors at the emission maximum of the binding species.

5.3 Materials and Methods

5.3.1 Optical setup

The triple-color SW-FCCS optical setup (Fig. 5.1) consisted of a cw Argon ion laser (Lasos Lasertechnik GmbH, Jena, Germany) with two laser lines 488 nm and 514 nm. An excitation filter z488/10x (Chroma Technology Corp., Rockingham, USA) is used to transmit only the 488 nm excitation line. The collimated laser beam is expanded by two biconvex lenses $f = 10$ mm and $f = 150$ mm and illuminates the back aperture of a 40x/1.15 NA water immersion objective (Olympus, Hamburg, Germany) mounted on an Olympus microscope IX70. The beam is focused to a diffraction-limited spot in a sample solution containing fluorescent dyes. The emitted fluorescence is collected by the same objective and is transmitted by a dichroic mirror 505DRLP (Omega Optical, Brattleboro, USA) that separates the fluorescence from the scattering and excitation light. Two more dichroic mirrors 560DRLP and 630DRLP (Omega) split the emission pathway into three detection channels, green, yellow and red. The intermediate focus by the tube lens is imaged (magnification $M = 1$) via three achromat lenses $f = 30$ mm (green), 40 mm (yellow) and 50 mm (red) (Thorlabs Inc., Newton, USA) onto the proximal end of a 50 μ m fiber (Thorlabs). Bandpass filters 520DF40 (Omega), HQ585/40m and HQ700/90m (Chroma) are placed in front of the fiber ends to further restrict the wavelength interval for an enhanced wavelength filtering. Photons are detected with three avalanche photodiodes (Perkin-Elmer SPCM-AQR-13 in the green and yellow channel and SPCM-AQR-14 in the red channel). The signals are split between three hardware correlator cards Flex02-12D, Flex99 (Correlator.com, New Jersey, USA) and three pair-wise cross-correlations between green and red, yellow and red, and green and yellow channels are performed at the same time on three separate personal computers.

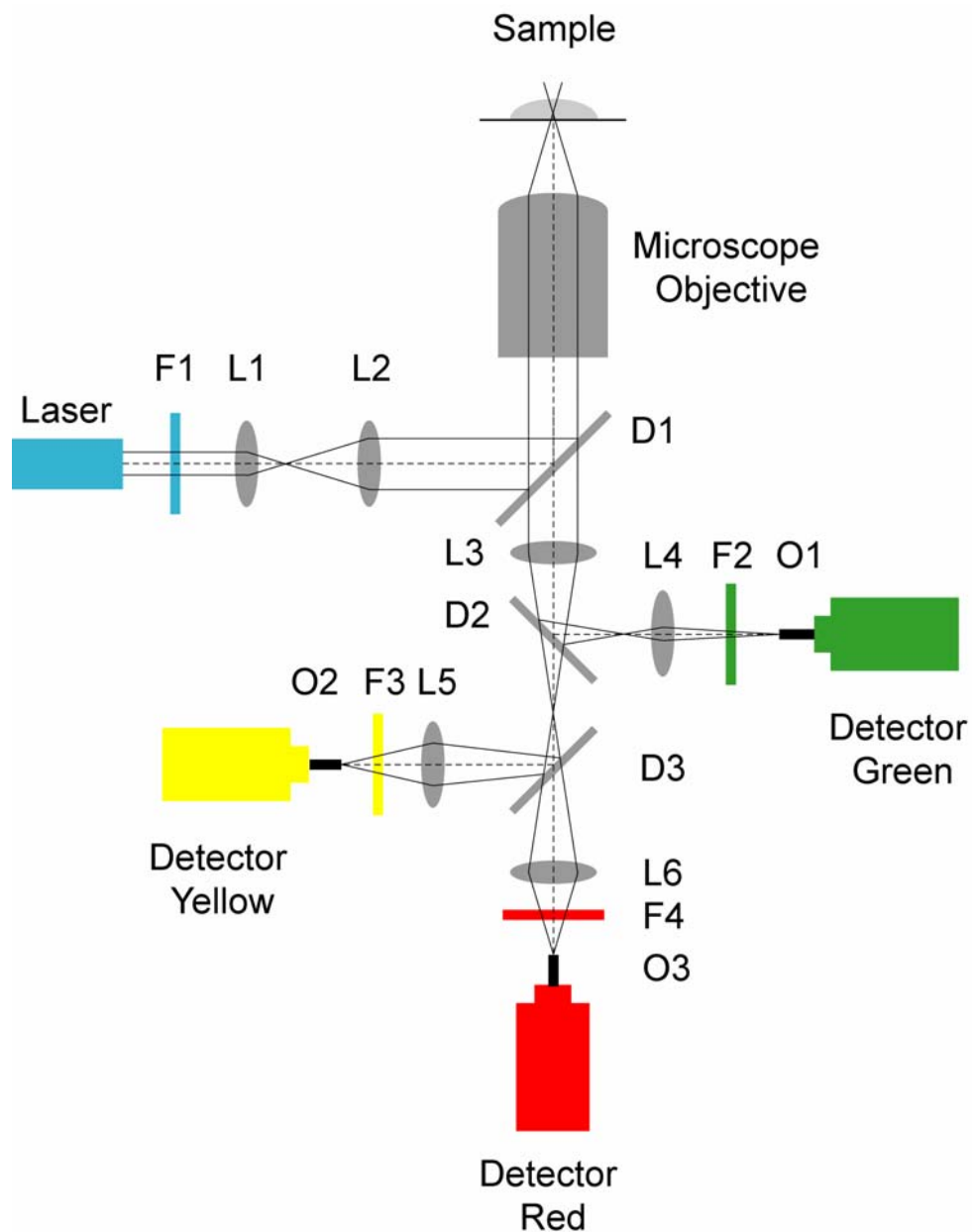


Figure 5.1: The three-color cross-correlation fluorescence spectrometer consists of a typical FCS setup with three detection pathways. A single laser beam is expanded and collimated by lenses L1 and L2. The microscope objective focuses the beam into the sample. The fluorescence light emitted is focused by the tube lens L3 and split three-ways into different wavelength regions via dichroics D2 and D3. Lenses L4-L6 focus the emission beams onto fibers O1-O3. F1: excitation filter; F2-F4: bandpass filters; L1-L6: lenses; D1-D3: dichroic mirrors; O1-O3: optical fibers.

5.3.2 Chemistry

Ligands biotin-4-fluorescein, R-phycoerythrin biotin-XX conjugate and receptor Alexa Fluor 647-R-phycoerythrin-streptavidin were purchased from Invitrogen (Basel, Switzerland). Streptavidin is a homotetrameric protein with 4 biotin-binding sites. To maintain AXSA always at full binding with varying BF and BPE concentrations, 9 aliquots of AXSA was fixed at constant concentration 5 nM whilst BF was added in increasing concentrations from 0-20 nM to give BF/AXSA concentration ratios = 0, 0.5, 1...4. This was incubated before adding decreasing concentrations of BPE into the same aliquots from 20-0 nM at BPE/AXSA concentration ratios = 4, 3.5, 3...0 to fully occupy the remaining free binding sites of AXSA. Three types of negative controls with all three reactants at the same concentrations as the positive control were prepared in 9 aliquots to inhibit (1) all binding sites, (2) BPE binding and (3) BF binding. Negative control (1) was prepared by first incubating AXSA with excess unlabeled D-biotin (Invitrogen, 1 μ M) to saturate completely all binding sites, then adding BF and incubating it before adding in BPE. In negative control (2), BPE binding was inhibited by first incubating BF with AXSA and then saturating all available binding sites with excess D-biotin (1 μ M), before mixing BPE. Likewise, negative control (3) was prepared by first incubating BPE to AXSA and the remaining binding sites saturated with excess D-biotin (1 μ M), before adding the inhibited BF ligand. All incubation times were \sim 30 minutes and all samples were prepared in PBS buffer pH 7.4 (Sigma-Aldrich Chemie GmbH, Buchs, Switzerland).

5.4 Results and Discussions

5.4.1 Characterization of fluorophores for SW-FCCS

In this chapter, fluorescein, R-phycoerythrin, a 240 kDa phycobiliprotein and Alexa Fluor 647-R-phycoerythrin, a tandem dye, were selected for SW-FCCS due to their overlapping excitation spectra and minimal cross-talk. Their molar extinc-

tion coefficients at 488 nm are shown in Table 5.1. The series of installed dichroic mirrors and bandpass filters effectively separates the emission wavelengths yet providing high count rates. Their absorbance and emission spectra are shown in Fig. 5.2, A and B. The fluorescence yields η in each channel were calculated from the photon counts per second divided by the number of molecules determined from the amplitude of the ACF. The η values were corrected for background from Raman scattering of water in the yellow and Rayleigh scattering of the laser line (Table 5.1).

Molecule	ϵ [$\text{M}^{-1} \text{cm}^{-1}$]	η^g	η^y	η^r	q
BF	63,500	13,300	4,300	500	0.17
BPE	824,500	200	24,400	2,300	1.0
AXSA	980,000	6,100	22,000	318,100	1.0

Table 5.1: Molar extinction coefficients ϵ at 488 nm, fluorescence yields (η) in Hz/molecule and residual fluorescence factor (q) after binding of the receptor and ligands measured at laser power 50 μW .

The quenching of BF and BPE upon binding was measured independently by adding excess unlabeled streptavidin (Sigma-Aldrich) and by monitoring the changes in their fluorescence intensities. The average fluorescence intensity for BPE remains the same ($q = 1.0$) upon binding streptavidin but BF is quenched 83% ($q = 0.17$) corresponding to literature values (84 – 88%) [123]. Note that the shorter biotin-4-fluorescein ligand is quenched more than fluorescein-biotin used in chapters 3 and 4 ($\sim 75\%$) due to stronger, faster and non-cooperative binding between the less hindered biotin-4-fluorescein and streptavidin [123]. The fluorescence yields η and the quenching factors q in all three channels contributed by the fluorophores are tabulated in Table 5.1. These values are used to calculate the fits from Eq. 5.11 for the positive control curves. Average photon count rates detected for all three channels were measured and compared between the positive and negative controls for all binding ratios. No relative changes were observed in fluorescence intensities upon binding to form BPE-AXSA and BF-BPE complexes. Therefore, FRET process was excluded from the equations.

Other fluorophore combinations have also been considered for multicolor SW-

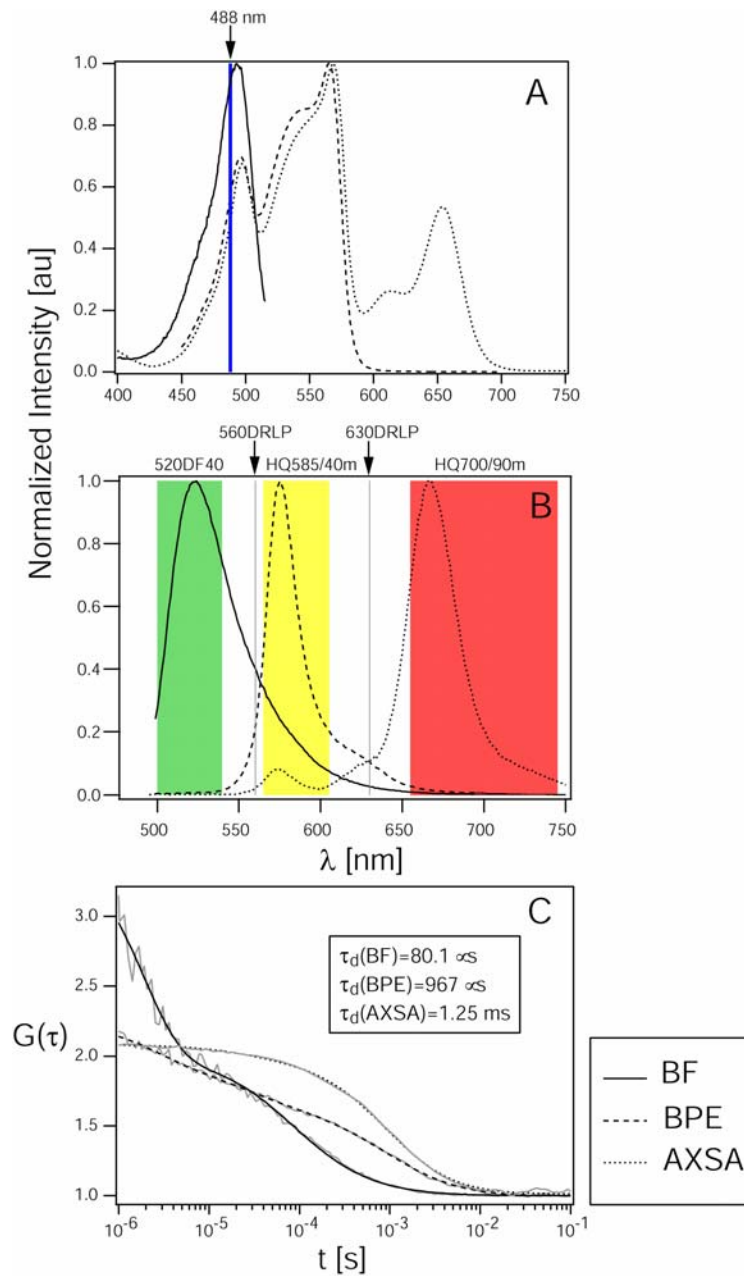


Figure 5.2: (A) Absorbance spectra of the fluorophores labels of BF, BPE and AXSA. The excitation probabilities at the laser excitation line 488 nm are 93%, 56% and 50% respectively. (B) Fluorescence emission spectra of the three dyes. The detection windows of the molecules are specified by the dichroics and bandpass filters selected. All spectral curves are normalized. (C) Autocorrelation functions (grey curves) and their fits (black curves) all normalized to their total number of molecules in the green, yellow and red detection channels for BF, BPE and AXSA respectively. The inset box shows the average diffusion times obtained from the fitting of the functions.

FCCS. Organic dye pairs and QDs have been measured in chapters 3 and 4. In particular, quantum dots have become a convenient choice for multicolor detection due to high quantum yield and continuously tunable emission spectra that can all be excited with one laser line. In these experiments, organic dyes were selected instead of quantum dots due to the relative ease of control of binding ratios of biotin to streptavidin. Commercially available quantum dots are developed mainly for imaging purposes and usually have high protein to label conjugation (10–15 streptavidin molecules per quantum dot) [91], making the binding concentrations difficult to manipulate between three binding partners. In addition, aggregation problem with quantum dots has been previously reported in chapter 3. Although QDs are better in terms of photostability and brightness, their aggregation in solution makes it difficult to unambiguously determine interactions. Alternatively, tandem dyes have been widely used in flow cytometric applications for simultaneous detection of multiple fluorophores excited with a single laser [112]. These bright dyes are used for the same advantages for the application to SW-FCCS.

A range of other possible dyes that could be used for *in vitro* and *in vivo* SW-FCCS, including fluorescent proteins and Megastokes dyes [89], have been measured and their fluorescence yields are listed with their filter sets in Table 5.2.

Count rates per molecule [Hz] obtained at excitation wavelength of 488 nm					
Fluorophore	$\lambda_{ex}/\lambda_{em}$ [nm]	Green (510AF23)	Yellow (560DF15)	Red (645AF75)	
Fluorescein	494/518	22,000	3,800	1,600	
485XL-SA	485/560	2,400	12,000	10,000	
480XL-SA	500/630	800	800	1,500	
QRSA	488/670	3,200		71,400	Red (695AF55)
QD655	400-633/ 655	500		195,500	
GFP	484/510	2-8,000	43% cross-talk	20% cross-talk	
YFP	512/529	24% cross-talk	2-8,000	-	
RFP	584/607	12.5% cross-talk	-	2-20,000	
Count rates per molecule [Hz] obtained at excitation wavelength of 514 nm					
520XL-B	520/664		50	1,000	Yellow (545AF35) Red (645AF75)
480XL-SA	500/630		1,800	20,000	

Table 5.2: Possible fluorophores and filter sets for multicolor SW-FCCS. For fluorescent proteins the cross talk is given in yield strongly depends on the labeled protein.

G/Y/RFP: Green/Yellow/Red fluorescent protein
xxxXL-SA/B: Megastokes dyes conjugated with streptavidin/biotin
QRSA: Quantum red (R-phycoerythrin-Cy5)-streptavidin
QD655: quantum dot-streptavidin

5.4.2 Calibration experiments

Calibration measurements were performed with Fluorescein (Invitrogen, 1 nM) in the green and yellow channels and AXSA in the red channel. ACFs of BF, BPE and AXSA were measured with increasing laser power from 50–500 μW to investigate the change of cpm and triplet state population against excitation intensity. The diffusion times of the different molecules showed deviations at higher excitation intensities, however this change depended on the molecular species and was minimal in the setup below 100 μW for all three species. A laser power of 50 μW was selected for minimal optical saturation and photobleaching of the dyes, optimal count rates and low triplet fraction obtained between all three fluorescent dyes. Ten correlation functions measured for 10 s were taken for all ACF and CCFs. All correlation curves were fitted with the Levenberg-Marquadt fitting algorithm in Igor Pro (v4.0 Wavemetrics, Oregon, USA). A fitting model for one-component diffusion model with triplet state (see chapter 2, Eq. 2.17 [126]) was used for the ACFs of BF and AXSA. The BPE ACFs were fitted with the one-component diffusion model with two triplet states where the first decay corresponds to the singlet-triplet lifetime in the microsecond timescale [141]. The second decay in the tens of microsecond timescale could be due to other photodynamic process involved with R-phycoerythrin. The normalized ACFs and their fits are shown in Fig 5.2, C. Fluorescein with a relative molecular weight of 376.3 Da and a reported diffusion coefficient D of $3.0 \times 10^{-6} \text{ cm}^2/\text{s}$ [37] was used as a standard dye to characterize the excitation volume. The beam waist radius w_o of 0.29 μm is calculated from Eq. 2.16 where the average diffusion time τ_d of 70.6 μs of fluorescein was determined from the fits of the ACFs. The diffusion coefficients of BF, BPE and AXSA at $2.6 \times 10^{-6} \text{ cm}^2/\text{s}$, $2.2 \times 10^{-6} \text{ cm}^2/\text{s}$ and $1.7 \times 10^{-7} \text{ cm}^2/\text{s}$ respectively are calculated from the beam waist and the respective diffusion times that are obtained from the fits in Fig. 5.2 C. The relative molecular weights of the molecules are then determined from Stokes-Einstein equation (see chapter 2, Eq. 2.19), which assumes spherical molecules, to be 547.6 Da, 964 kDa and 2,100 kDa

respectively. The experimentally determined relative molecular weight of BF is similar to the literature value of 644.7 Da. However, the molecular weights of BPE and AXSA are much higher than the reported values of 240 kDa and 294 kDa. This is most likely due to the non-spherical shapes of the molecules [142] that the equation does not take into account. A deviation from the spherical shape will lead to a decrease in the diffusion coefficient [47].

The blinking times of the triplet states for different labels are uncorrelated to each other despite being bound to the same complex. Thus, the triplet fractions that are detected in the ACFs, are not detectable in the CCFs. The triplet state will reduce the count rate of the dye but the total number of molecules in the ACF/CCFs remains constant. All the CCFs could be fitted sufficiently well with the one-component diffusion model and the structure parameter K [37] was obtained as 1.02 ± 0.02 for $G_{gr}(\tau)$, 1.06 ± 0.18 for $G_{yr}(\tau)$ and 3.45 ± 1.45 for $G_{gy}(\tau)$. The average K parameter was then fixed at 2 for all future cross-correlation fits.

5.4.3 Experimental results of streptavidin-biotin binding

In the following discussion, AXSA is referred as R , BPE as L_y and BF as L_g . In general the CCFs exhibit the following trends. Under otherwise equal conditions the positive controls will have higher CCF amplitudes due to complexes with multiple colors than the negative controls. The negative controls show only weak cross-correlations due to the cross-talk of the fluorophores into different channels. But both, negative and positive controls will show decreasing amplitudes with increasing number of complexes or ligands and receptors.

5.4.4 Correlations of triple-color complexes

At any one time, three different components were mixed together in one sample aliquot and $G_{gr}(\tau)$, $G_{yr}(\tau)$, $G_{gy}(\tau)$ were measured simultaneously. The CCFs and their fits for a ligand/receptor concentration ratio $L_g:L_y:R = 2:2:1$ are shown in Fig. 5.3, A–C. The negative control amplitudes are due to cross-talk between

the respective channels but the positive control amplitudes are clearly higher due to the bound species.

The amplitudes for each ligand/receptor ratio for positive and negative controls are plotted in Fig. 5.4, A–C. Fig. 5.4 A shows $G_{gr}(0)$ decreasing with 0–4 L_g and 4–0 L_y molecules bound to R due to the formation of complexes containing R and L_g (Eq. 5.11). In the case of the negative control (Eq. 5.12) where there is an absence of receptor-ligand complexes, the curve decreases sharply. The contribution to the amplitude is from cross-talk which is analogous to the ACFs. Likewise for Fig. 5.4 B, $G_{yr}(0)$ decrease toward increasing concentration of complexes containing R and L_y . Although there is no direct binding between L_g and L_y , the binding through an intermediate receptor R gives rise to $G_{gr}(\tau)$ as shown in Fig. 5.4 C. In this case, the positive control amplitude drops to a minimum toward the center of the curve where a maximum of complexes containing L_g and L_y is reached due to the presence of equal concentrations of L_g and L_y . As predicted, the correlation amplitudes are smaller for negative controls compared to positive controls in all cases.

5.4.5 Fitting analysis of triple-color complexes

It is well-known that biotin-(strept)avidin has one of the strongest interactions known at present between a receptor and its ligand ($K_d = 10^{-15}$ M). In order to determine how accurate the fitting parameters are to model the experimental curves, the parameters K_d and V_{eff} were varied by changing the goodness-of-fit χ^2 value by no more than 50% from the best fit value i.e. minimum χ^2 . The negative control curves, shown by the shaded regions in Fig. 5.4, A–C are fitted (Eq. 5.11) to give V_{eff} 1.1 to 2.1 femtoliter (Table 5.3). The fitted V_{eff} values generally increase with the emission wavelengths detected from the fluorescent dyes i.e. $V_{eff}(G_{gy}(0)) \leq V_{eff}(G_{gr}(0)) \leq V_{eff}(G_{yr}(0))$. Positive controls are modeled with Eq. 5.11 to give the range of V_{eff} and K_d s (Table 5.3), shown by the shaded regions in Fig. 5.4.

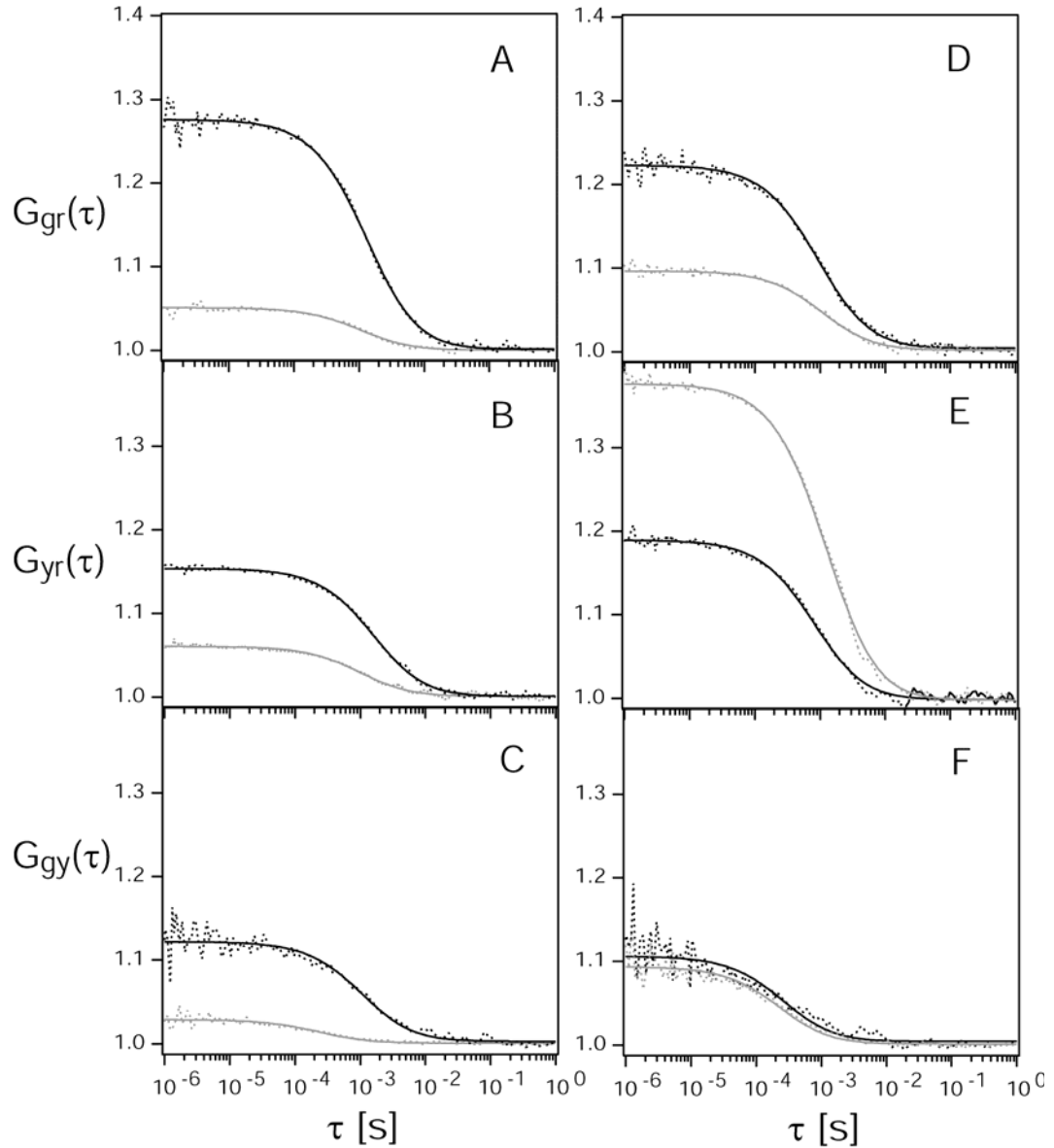


Figure 5.3: Cross-correlation functions of green \times red, yellow \times red and green \times yellow at concentration ratios $L_g/R = L_y/R = 2$ and $R = 5$ nM. (A–C) Positive control (black curves) and negative control (grey curves) of L_g and L_y binding to R . (D–F) Binding and inhibition curves of alternate ligand, L_g binding to R and L_y inhibited (black curves) or L_y binding to R and L_g inhibited (grey curves). Dotted curves show cross-correlation data and bold curves show their fits. Excitation wavelength: 488 nm, laser power: 50 μ W.

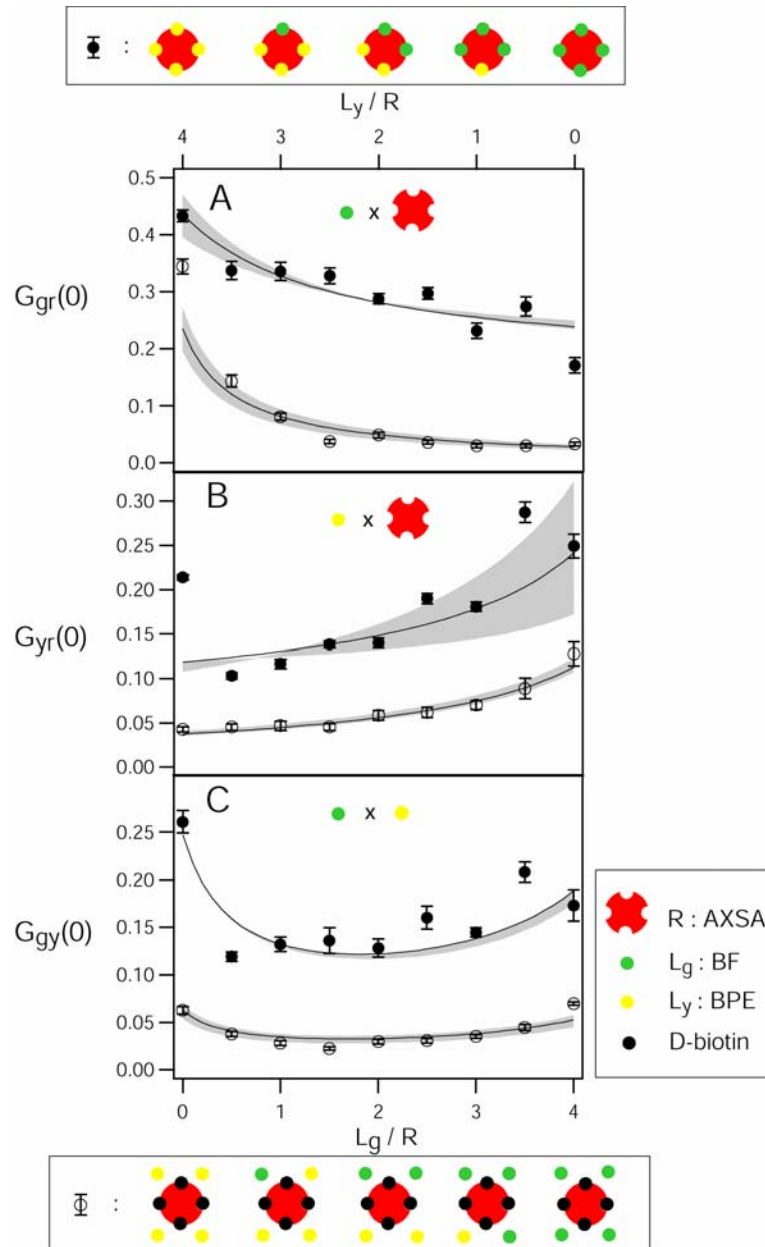


Figure 5.4: Simultaneous binding experiments of L_g and L_y ligands to R show the change of the cross-correlation amplitudes with increasing ligand/receptor concentration ratios. The top schematic drawing depicts R with four binding sites binding to 0–4 of L_g molecules and 4–0 of L_y molecules keeping the number of biotin ligands constant; and the bottom drawing depicts the negative control where all binding sites are inhibited with D-biotin. Experimental data points for positive control (filled circles) and negative control (empty circles) show the binding between L_g and R (A); L_y and R (B) and L_g and L_y (C). The error bar at each data point is calculated from the standard deviation of 10 measurements. The black curve shows the best fitting model to the data points and the shaded regions show the K_d and V_{eff} limits where models are fitted within 50% of the best fit parameter χ^2 (Table 2). The curves show a clear distinction between the positive and negative controls in their cross-correlation amplitudes. Excitation wavelength: 488 nm, laser power: 50 μW .

The obtained K_{ds} are 6 orders of magnitude above the predicted 10^{-15} M. One reason for this is that the experiments were performed with sample concentrations in the nanomolar range (sensitivity limit of FCS) that makes it difficult to determine K_{ds} at 6 orders below this concentration limit. The K_{ds} determined from these fits however are close to FCS measurements done on the same binding system at similar concentration levels [101]. Another reason could be due to ligand and/or receptor impurities that cause the binding curve to alter its slope. Labeling ratios between protein and label is another possible factor affecting the slope of the binding curve. Having more than one label increases the brightness of the product and this contributes to the ACF amplitude with the square of its fluorescence yield and the CCF with the product of the fluorescence yields. Here, it is assumed that all labeling ratios for ligands and receptor are 1:1 as stated by the supplier, and the average cpm values are used to model the curves.

Nevertheless, it is the magnitude of difference in amplitudes between the positive and negative control curves that resolves the binding of two components. To determine complex formation, it is demanded that the difference between the positive (+) and negative (-) control should be at least 6 standard deviations (see chapter 4, Eq. 4.22). Factors that affect this difference include fluorescence yields, cross-talk and impurities (see chapter 4). Although $G_{yr}(0)$ has a smaller difference because of larger cross-talk between L_y and R from yellow emitting R-phycoerythrin molecules in AXSA molecules, the differences between all positive and negative control curves are more than 6 standard deviations. Therefore, by measuring multiple cross-correlation curves with a single sample at one $L_g/L_y/R$ concentration ratio, it is possible to determine binding between the different biomolecules.

The most significant differences between positive and negative controls are found when working at stoichiometric concentrations. When measuring biotin to streptavidin ratios above 4:1, increasing free L_g molecules contribute a larger background to the CCF. This decreases the amplitudes sharply toward the negative

control, thus making binding irresolvable (see chapter 4).

Samples	V_{eff} [femtoliter]		K_d [M]		
	Lower-Upper	Best Fit	Lower-Upper	Best Fit	
Negative control	$G_{gr}(0)$	1.3 – 1.8	1.5		
	$G_{yr}(0)$	1.84 – 2.1	2.0		
	$G_{gy}(0)$	1.1 – 1.4	1.2		
Positive control	$G_{gr}(0)$	0.83 – 1.0	0.9	$(2 - 4)10^{-8}$	1×10^{-8}
	$G_{yr}(0)$	0.7 – 1.57	1.0	$(0.07 - 1.9)10^{-8}$	7×10^{-10}
	$G_{gy}(0)$	0.35 – 0.39	0.35	$(2 - 7)10^{-8}$	4×10^{-8}
L_g binds, L_y free	$G_{gr}(0)$	0.94 – 1.1	1.0	$(0.7 - 1)10^{-8}$	1×10^{-8}
	$G_{yr}(0)$	1.2 – 1.3	1.3	$(0.05 - 1)10^{-9}$	5×10^{-11}
	$G_{gy}(0)$	2.5 – 3.1	3.1	$(0.5 - 4)10^{-10}$	5×10^{-11}
L_y binds, L_g free	$G_{gr}(0)$	0.94 – 1.1	1.1		
	$G_{yr}(0)$	1.63 – 2.2	2.2	$(0.09 - 4)10^{-9}$	9×10^{-11}
	$G_{gy}(0)$		1.2	$(5 - 7)10^{-9}$	6×10^{-9}

Table 5.3: Lower to upper limits and best fit values obtained for effective observation volumes (V_{eff}) and equilibrium dissociation constants (K_d), determined from the various binding curves.

5.4.6 Correlations of complexes with alternate ligand binding

The difference in amplitudes between the positive and negative controls of Fig. 5.4 A and B show that binding occurs between both L_g and L_y ligands with receptors. However, this does not proof the existence of complexes formed between L_g , L_y and R simultaneously. Only $G_{gy}(\tau)$ confirms the existence of complexes containing L_g , L_y and R . However, this conclusion is based on the assumption that the components are known beforehand and the nature of binding is identified. In this case, it is known that biotin binds specifically to streptavidin and does not dimerize with itself. In fact, $G_{gy}(\tau)$ may even be sufficient to determine complexation between L_g , L_y and R here [143]. In cases where the nature of binding is not known, additional negative controls will have to be performed to confirm that complexes RL_gL_y are formed. Further negative controls have been performed, where only one ligand at a time is bound to the receptor and the binding of the second ligand is inhibited. The cross-correlation curves for a ligand/receptor con-

centration ratio of $L_g:L_y:R = 2:2:1$ are shown in Fig. 5.3, D–F. The binding and non-binding cases are clearly distinguishable for $G_{gr}(\tau)$ and $G_{yr}(\tau)$ (Fig. 5.3, D and E) where the interacting species possesses the higher cross-correlation amplitudes. The similar cross-correlation curves for $G_{gy}(\tau)$ (Fig. 5.3 F) demonstrate that the ligands are not complexed either directly or indirectly via streptavidin. The cross-correlation amplitudes over the whole range of ligand/receptor ratios are plotted in Fig 5.5, A–C.

Case 1: When L_g is added to R with L_y inhibited, $G_{gr}(0)$ (Fig. 5.5 A, empty circles) decreases gradually comparable to the positive control (Fig. 5.4 A), whilst the $G_{yr}(0)$ and $G_{gy}(0)$ curves (Fig. 5.5, B and C, empty circles) are similar to the negative controls of Fig. 5.4 B and C.

Case 2: Binding between L_y and R with L_g inhibited shows the $G_{yr}(0)$ values (Fig. 5.5 B, filled circles) eventually decreasing at higher L_y concentrations, as expected. Conversely, the $G_{gr}(0)$ and $G_{gy}(0)$ negative controls curves (Fig. 5.5, A and C, filled circles) decrease rapidly to lower amplitudes similar to the negative control curves in Fig. 5.4, A and C.

In Fig. 5.5 A the cross-correlations $G_{gr}(0)$ have the same amplitudes when no ligand L_g is present. The same effect can be observed in Fig. 5.5 B, where the cross-correlation amplitudes are similar when no ligand L_y is present. For all other cases the cross-correlations representing the interacting molecules are always higher in amplitude than the cross-correlation representing the non-interacting molecules. In Fig. 5.5 C, the $G_{gy}(0)$ values are similar, no matter whether L_y or L_g is inhibited from binding. The curves are comparable to the negative control of Fig. 5.4 C since no complexes containing L_g and L_y simultaneously exist. In addition, it should be noted that if all three species are present, the amplitudes of the CCFs are always highest for the case of interacting molecules. For instance, when inhibiting L_y from binding (empty circles) the highest amplitudes are found in Fig. 5.5 A, the $G_{gr}(0)$ channel. Conversely, when inhibiting L_g from binding (filled circles) the highest amplitudes are found in the $G_{yr}(0)$ channel (Fig. 5.5 B). The triple

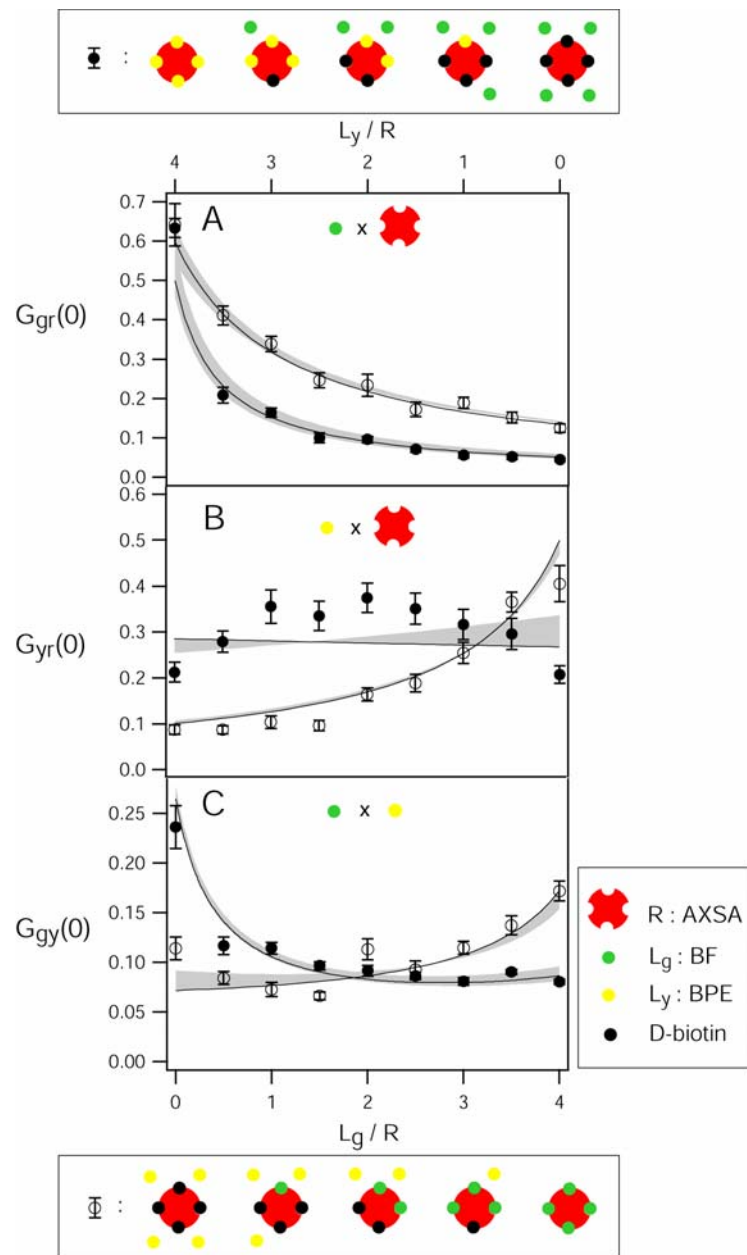


Figure 5.5: Controls with alternate ligand L_g or L_y inhibited independently with D-biotin are shown in the top and bottom schematic drawings respectively. The cross-correlation amplitudes vs. ligand/receptor concentration ratios are depicted. L_g bound and L_y free (empty circles) give higher amplitudes for $G_{gr}(0)$ indicating RL_g complexes formed (A), but no binding shown for $G_{yr}(0)$ (B) and $G_{gy}(0)$ (C). The cross-correlations with L_y bound and L_g free (filled circles) give higher amplitudes for $G_{yr}(0)$ indicating RL_y complexes formed (B), but no binding shown for $G_{gr}(0)$ (A) and $G_{gy}(0)$ (C). Black curves show the best fit curve with the lowest χ^2 and the shaded regions give the limits of K_d values and V_{eff} values fit to within 50% from the lowest χ^2 (Table 2). Excitation wavelength: 488 nm, laser power: 50 μ W.

pair-wise cross-correlations directly show which molecules are interacting, thus substantiate the initial results from Fig. 5.4, A–C that trimers are indeed formed between both ligands and the receptor.

5.4.7 Fitting analysis of complexes with alternate ligand binding

Additional negative control curves with L_y or L_g binding inhibited are also modeled with Eq. 5.14 to give the best fit range of V_{eff} and K_d within 50% of the lowest χ^2 (shaded regions Fig. 5.5, A–C). The exception is the $G_{gr}(0)$ curve representing L_y binding and L_g inhibition (Fig 5.5 A, filled circles) that could not be fitted to give a K_d within the limits of 10^{-15} to 10^{-6} M. This is due to the fact that L_y does have negligible cross-talk into the green channel (see Table 5.1) and thus the RL_y complexes do not contribute to the CCF and a determination of a K_d value is not possible. Therefore, the data points are fitted instead with Eq. 5.12 where cross-talk from free L_y and RL_y complexes into the green channel could be taken to be negligible. The fitting analysis yield K_d s of streptavidin-biotin binding from 10^{-11} – 10^{-8} M (Table 5.3). The difference between $G_{gr}(0)$ positive and negative control curve is more than 6 standard deviations (Fig. 5.5 A). This excludes the first point that does not have any L_g present and consists of only background from RL_y complexes. $G_{gr}(0)$ on the other hand fulfills the condition for binding only at higher concentrations of L_y/R (Fig. 5.5 B). This is because at low L_y/R concentrations, free L_g molecules contribute to the cross-correlation as background via cross-talk, making binding indistinguishable. Both the negative controls with L_y or L_g inhibited have no contribution to $G_{gy}(\tau)$ from simultaneous binding of L_y and L_g to R (Fig. 5.5 C). Therefore both curves at low amplitudes show little difference from each other and the contribution to the cross-correlation amplitudes come mainly from cross-talk of the fluorophores.

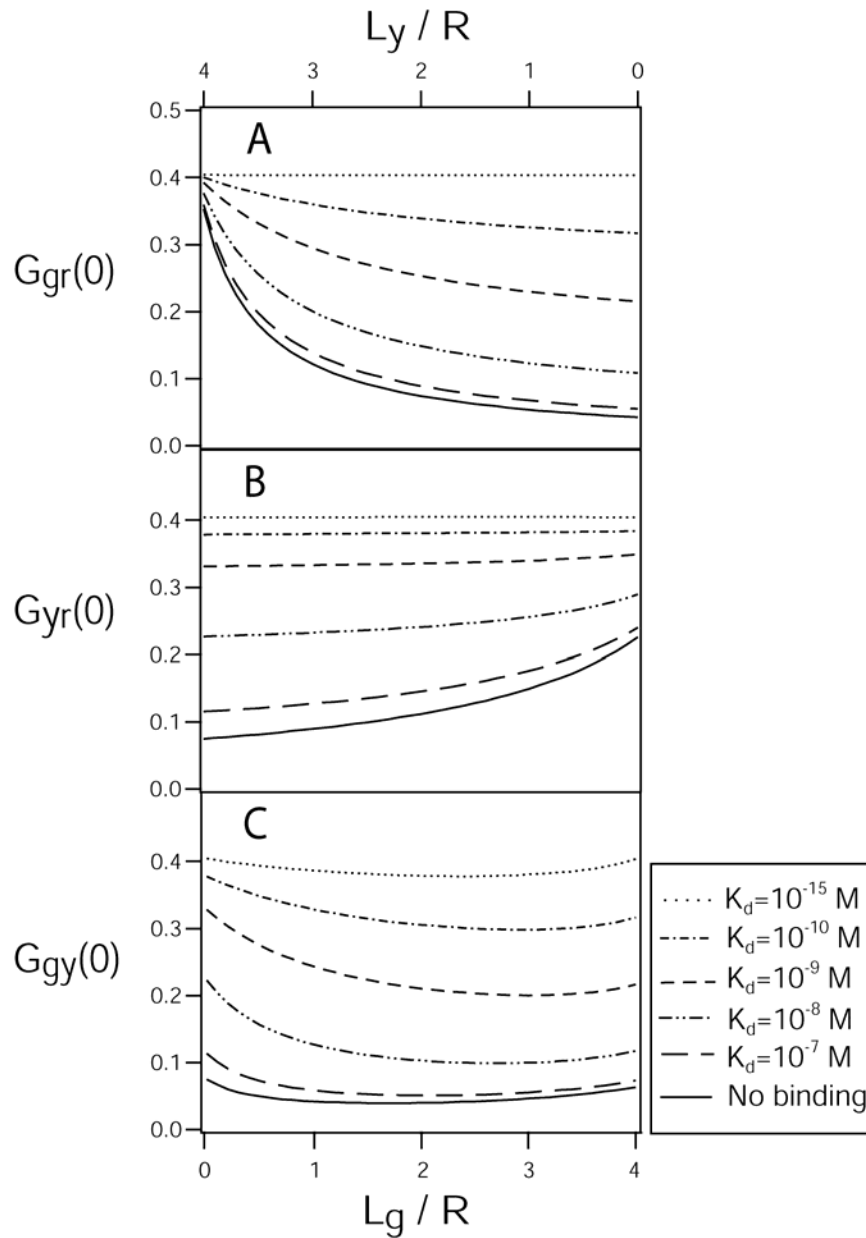


Figure 5.6: Effect of K_d on cross-correlation amplitudes calculated for the binding of L_g and L_y to R using fluorescence yields from Table 1 at $V_{eff} = 1.0$ fl and 4:1 stoichiometry. Cross-correlation amplitudes are plotted vs. ligand/receptor concentration ratios for (A) $G_{gr}(0)$; (B) $G_{yr}(0)$ and (C) $G_{gy}(0)$. The positive control curves with lower binding affinity converge towards the negative control.

5.4.8 Limitations of SW-FCCS

Influence of K_d on cross-correlations

The effect of K_d on cross-correlation amplitudes were calculated from the models as a function of ligand/receptor concentration ratios. K_{dS} were varied from 10^{-15} to 10^{-7} M at full binding conditions (Fig. 5.6, A–C). The changes in cross-correlation amplitudes of the negative control curves are due to cross-talk in both channels. The positive control curves decrease toward higher ligand concentrations for Fig. 5.6, A and B but remain relatively constant for Fig. 5.6 C. At higher K_{dS} (10^{-7} M) where more free reactants contribute to the CCFs and fewer complexes are formed, the separations of amplitudes between the positive and negative control curves diminish. Thus the limit of measurable K_d is reached when the positive and negative control have a difference that is smaller than 6 standard deviations. This in turn is dependent on the count rates of the different reactants and their cross-talk into the different channels.

Influence of impurities on cross-correlations

Various types of impurities influence cross-correlation measurements. Inactive or unlabeled receptors or ligands contribute to the reduction in the difference between the positive and negative controls and decreases the sensitivity of the method. Multiple labeling sites on a reactant may as well affect the cross-correlation amplitudes. Some of these problems can be circumvented in cellular measurements when fluorescent proteins are used and labeling ratios are fixed. These parameters and its effects on dual-color SW-FCCS have been analyzed in detail in chapter 4.

Stoichiometry determination

The determination of stoichiometry with SW-FCCS has been demonstrated previously for direct binding with dual-color biomolecules in chapter 3 and 4. In the present case for triple-color cross-correlations, the ligands bind indirectly over a common interaction partner. With higher background due to a third color, the

stoichiometry can still be determined in a similar way depending on the K_d s of the ligands. By varying each ligand L_g and L_y across a range of concentrations whilst maintaining the receptor concentration constant, a plot of with L_g and L_y will reveal the stoichiometry of the binding system. Various simulations of different stoichiometric ratios and further explanations are presented in the next section.

5.4.9 Simulations of cross-correlation amplitudes for different reaction models

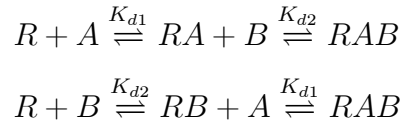
Receptor with the same ligand binding sites

This model assumes that 1–4 of the same ligands interact with 1 receptor. The dissociation constants of the receptor-ligand complexes $RL_1 \cdots RL_4$ are assumed to be the same throughout. This model has already been described before in the theory section. Here, I show how the stoichiometry of the receptor-ligand complex can be determined with simulations of $G_{gy}(0)$ with varying ligand/receptor concentration ratios. The fluorescence yields from Table 5.1 and V_{eff} of 0.35 fl were used for all simulations. It was assumed that there was no quenching ($q = 1$) upon binding of the ligands. Simulations were done for complexes from $R : L = 1 : 4$ to $R : L = 1 : 1$ at K_d of 10^{-15} M and 10^{-9} M. The stoichiometry of the binding ligand can be easily determined at the cut-off points of the curves along the x- or y-axis, just before it drops towards the negative control. At higher K_d s, the cut-off points become less obvious. Along the line of inflection diagonally between x- and y-axes, is where the receptor binding sites are always fully occupied, although with different numbers of L_g and L_y ($L = L_g + L_y$). For the cross-correlation experiments of $G_{gy}(\tau)$ (Figs. 5.4 and 5.5), the stoichiometry could not be determined because the experiments were measured at this concentration of full binding (along the line of inflection). In order to determine the stoichiometry, concentrations of either L_y (or L_g) will have to be kept constant and the concentration of L_g (or L_y) varied. The cut-off point indicating the stoichiometry of the ligand can then

be read off from the x-axis (or y-axis). This has been shown in chapter 3 and 4.

Receptor with different ligand binding sites

Receptor binding 1 ligand A and 1 ligand B The model for interactions of a receptor with 2 ligands is described in the following equations. It is presented here that 2 ligands A and B interact with receptor R with dissociation constants K_{d1} and K_{d2} respectively. This model is independent of sequential or simultaneous binding and does not take into account allosteric interactions. Allosteric interactions involve the binding of a specific ligand molecule that shifts the equilibrium between unbound and bound state. Thus, altering the affinity of the receptor for other ligand molecules [144]. Thus, in order to account for allosteric interactions, the interactions will have 4 different K_d s depending on the sequence of binding and which ligand molecule is binding to the receptor. This will allow allosteric interactions of a positive ($K_{d1} < K_{d2}$) or a negative nature ($K_{d1} > K_{d2}$) [135].



In this scheme, R is the free receptor that has two specific binding sites each for free ligand A and free ligand B . RA , RB and RAB are the bound complexes formed with RAB as the fully occupied receptor, yielding the following equations for K_{d1} and K_{d2} .

$$\begin{aligned} K_{d1} &= \frac{[R][A]}{[RA]} = \frac{[RB][A]}{[RAB]} \\ K_{d2} &= \frac{[R][B]}{[RB]} = \frac{[RA][B]}{[RAB]} \end{aligned}$$

The number of free receptors R_f is then defined by the total number of recep-

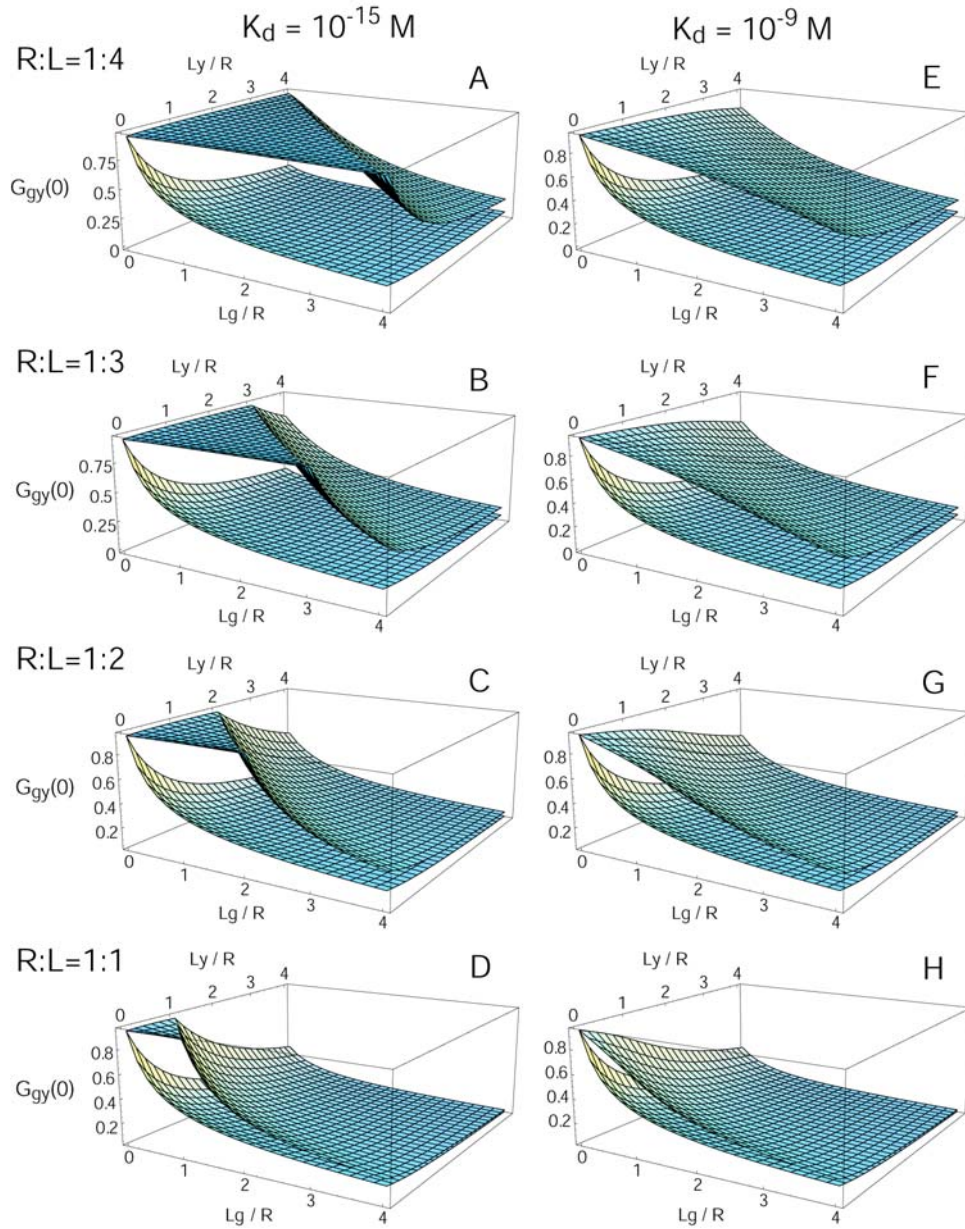


Figure 5.7: Simulations of the positive control cross-correlation amplitudes $G_{gy}(0)$ with L_g/R and L_y/R are shown for $K_d = 10^{-15}$ M (A-D, top curves) and $K_d = 10^{-9}$ M (E-H, top curves) and plotted against the negative controls (bottom curves) at a $V_{eff} = 0.35$ fl. Different stoichiometry ratios of $R : L (= L_g + L_y) = 1:4, 1:3, 1:2$ and $1:1$ are also shown. The line of inflection between both x-axes represents full binding between R and L . Stoichiometry is determined from the points where the line cuts the x- or y-axes, beyond which $G_{gy}(0)$ decreases steeply towards the negative control upon saturation of all binding sites. The cross-correlation experiments of $G_{gy}(\tau)$ (Figs. 4 and 5) were performed at this concentration of full binding. The line of inflection becomes less pronounced as K_d increases and the stoichiometry becomes less obvious.

tors R_t subtracted by the total number of occupied receptors. Similar equations are also derived for the number of free ligand molecules, A_f and B_f . The concentration of free receptors and ligands as well as the concentration of bound complexes RA , RB and RAB at binding equilibrium can then be numerically determined by solving the following equations simultaneously.

$$\begin{aligned}
R_f &= R_t - ([RA] + [RB] + [RAB]) \\
&= R_t - R_f \left(\frac{A_f}{K_{d1}} + \frac{B_f}{K_{d2}} + \frac{A_f B_f}{K_{d1} K_{d2}} \right) \\
A_f &= A_t - ([RA] + [RAB]) \\
&= A_t - \frac{R_f A_f}{K_{d1}} \left(1 + \frac{B_f}{K_{d2}} \right) \\
B_f &= B_t - ([RB] + [RAB]) \\
&= B_t - \frac{R_f B_f}{K_{d2}} \left(1 + \frac{A_f}{K_{d1}} \right)
\end{aligned}$$

The time dependent total fluorescence signal $F_i(t)$ from detection channel i is the sum of all signals of fluorescent species that contribute to the total signal, including species that cross-talk into the detection channel. To take into account possible changes in fluorescence yields η of interacting molecules upon binding, q factors representing the percentage of quenching or FRET processes can be included with η .

$$\begin{aligned}
F_i(t) &= F_A^i(t) + F_B^i(t) + F_R^i(t) + F_{RA}^i(t) + F_{RB}^i(t) + F_{RAB}^i(t) \\
&= N_A V_{eff} \left[\begin{aligned} &\eta_A^i A_f(t) + \eta_B^i B_f(t) + \eta_R^i R_f(t) + \eta_{RA}^i RA(t) \\ &+ \eta_{RB}^i RB(t) + \eta_{RAB}^i RAB(t) \end{aligned} \right]
\end{aligned}$$

where $\eta_{RA/B}^i = \eta_R^i + \eta_{A/B}^i$ and $\eta_{RAB}^i = \eta_R^i + \eta_A^i + \eta_B^i$

The CCF at $\tau = 0$ is obtained by cross-correlating the fluorescence signals from both detection channels i and j where

$$G_{ij}^+(0) = \frac{\eta_A^{ij}A_f + \eta_B^{ij}B_f + \eta_R^{ij}R_f + \eta_{RA}^{ij}RA + \eta_{RB}^{ij}RB + \eta_{RAB}^{ij}RAB}{N_A V_{eff} \left[\begin{array}{c} \left(\begin{array}{c} \eta_A^i A_f + \eta_B^i B_f + \eta_R^i R_f + \eta_{RA}^i RA \\ + \eta_{RB}^i RB + \eta_{RAB}^i RAB \end{array} \right) \times \\ \left(\begin{array}{c} \eta_A^j A_f + \eta_B^j B_f + \eta_R^j R_f + \eta_{RA}^j RA \\ + \eta_{RB}^j RB + \eta_{RAB}^j RAB \end{array} \right) \end{array} \right]}$$

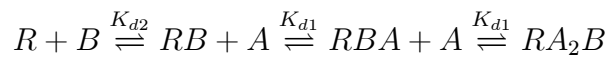
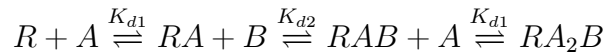
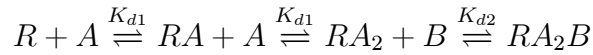
$$\text{where } \eta_{RA/B}^{ij} = \left(\eta_R^i + \eta_{A/B}^i \right) \left(\eta_R^j + \eta_{A/B}^j \right)$$

$$\text{and } \eta_{RAB}^{ij} = \left(\eta_R^i + \eta_A^i + \eta_B^i \right) \left(\eta_R^j + \eta_A^j + \eta_B^j \right)$$

The CCF for the negative control (at $\tau = 0$) consists of only free molecules that contribute to the CCF via cross-talk between both channels.

$$G_{ij}^-(0) = \frac{\eta_A^{ij}A_t + \eta_B^{ij}B_t + \eta_R^{ij}R_t}{N_A V_{eff} \left[\left(\eta_A^i A_t + \eta_B^i B_t + \eta_R^i R_t \right) \left(\eta_A^j A_t + \eta_B^j B_t + \eta_R^j R_t \right) \right]}$$

Receptor binding 2 ligands A and 1 ligand B The model for interactions of a receptor with 3 ligands is described in the following equations. In the present case, 2 ligand molecules *A* and 1 ligand molecule *B* interact with receptor *R* with dissociation constants K_{d1} and K_{d2} respectively. This model does not take into account allosteric interactions where there could be a possibility of the binding model having up to 9 different K_{d} s.



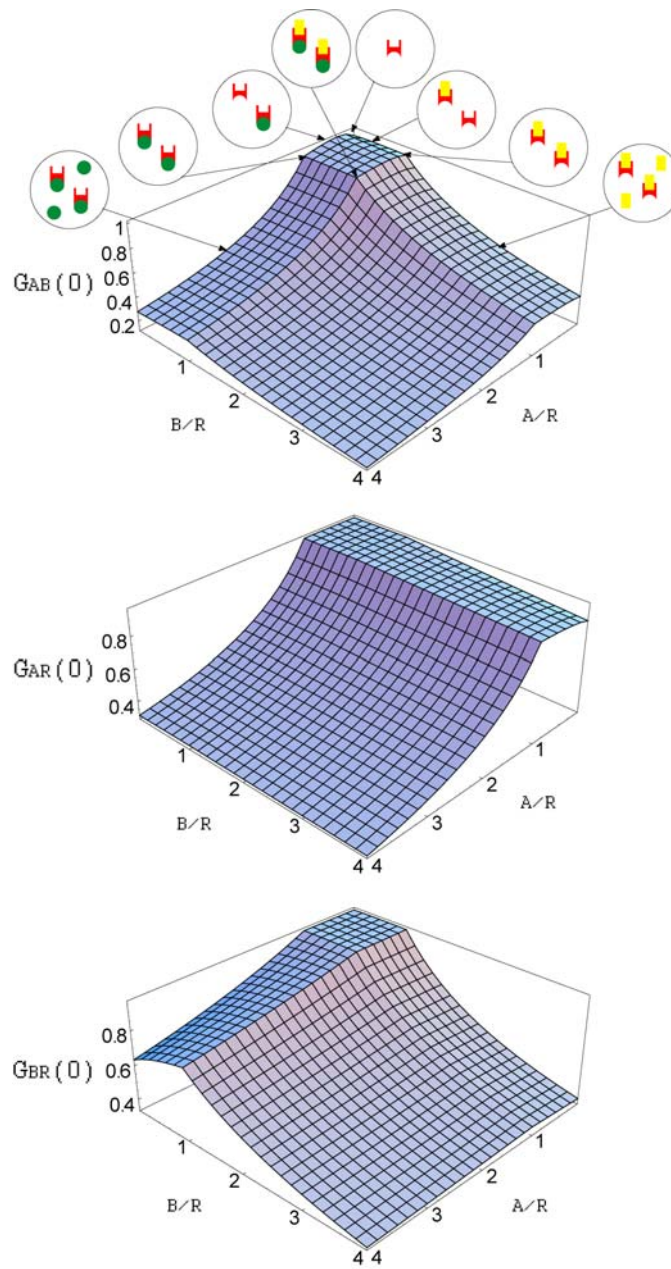


Figure 5.8: Simulations of cross-correlation amplitudes obtained from the binding of 1 ligand A and 1 ligand B to each receptor R. G_{AB} (top graph), G_{AR} (middle graph) and G_{BR} (bottom graph) are simulated at various combinations of A/R and B/R concentration ratios at $K_d = 10^{-15}M$ for all receptor-ligand interactions. The schematic drawing depicts the binding reaction at different ligand/receptor concentration ratios.

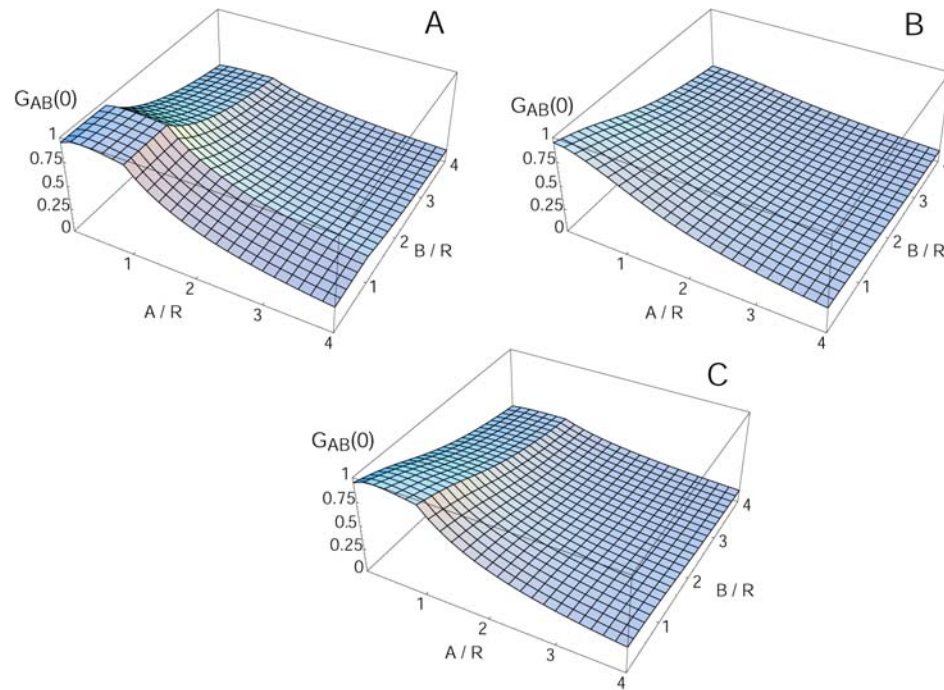


Figure 5.9: Determination of stoichiometry for complex RAB . Simulations of the positive control cross-correlation amplitudes $G_{AB}(0)$ for A/R and B/R are shown as 3D plots for (A) $K_d = 10^{-15}$ M and (B) $K_d = 10^{-9}$ M for both ligands A and B . The simulations were done using $V_{eff} = 0.35$ fl. The lines of inflection perpendicular to both the x- and y-axes represent the stoichiometry of the ligands A and B , respectively, i.e. $R : A : B = 1:1:1$. The lines of inflection becomes less pronounced as K_d s increases and the stoichiometry becomes less obvious. (C) Simulations of $K_{d1} = 10^{-15}$ M for ligand A and $K_{d2} = 10^{-9}$ M for ligand B . For this reaction where the K_d s of the ligands are independent of each other, the binding curves of the ligands that lie on the x- or y-axes remain the same despite the second ligand having a different K_d .

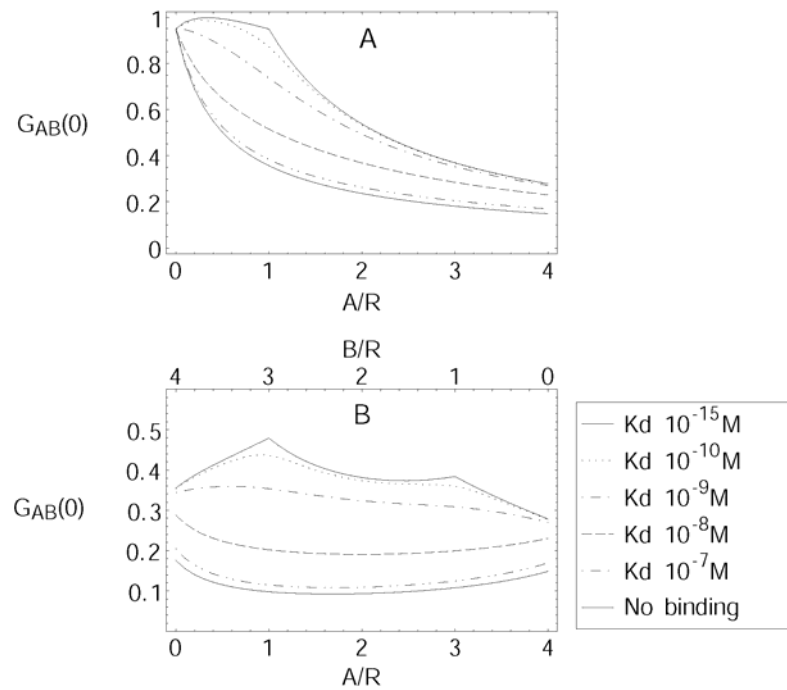


Figure 5.10: (A) Simulation of the $G_{AB}(0)$ binding curves at 0–4 A/R concentration ratios, with no ligand B from $K_d = 10^{-15}$ M to $K_d = 10^{-9}$ M. The plots of binding curves for ligand B is also similar at 0–4 B/R when ligand A is not included. The positive control curves decreases towards the negative control curves at higher saturation of the binding site. The difference in amplitudes between the positive and negative control decreases at higher K_d s. (B) Simulation of the $G_{AB}(0)$ binding curves at 0–4 A/R and 4–0 B/R ratios (view the diagonal cross-section of the 3D plot from $A/R = 4$ to $B/R = 4$). The stoichiometry of ligands A and B can be determined from the cut-off points of the curves where $A/R = 1$ and $B/R = 1$. These cut-off points become less defined as K_d of the reaction increases. Stoichiometry becomes then indistinguishable beyond $K_d = 10^{-9}$ M.

$$\begin{aligned}
K_{d1} &= \frac{[R][A]}{[RA]} = \frac{[RA][A]}{[RA_2]} = \frac{[RAB][A]}{[RA_2B]} = \frac{[RB][A]}{[RBA]} \\
K_{d2} &= \frac{[R][B]}{[RB]} = \frac{[RA][B]}{[RAB]} = \frac{[RA_2][B]}{[RA_2B]}
\end{aligned}$$

In this model, R is the unoccupied receptor with 2 binding sites for A , RA are receptors with one of either binding site occupied with A , and RA_2 is the receptor fully occupied with A . For complexes RA and RAB , A could be binding to either one of 2 binding sites of R , thus multiplicity of binding sites is taken into account for the following equations. Take note that the total concentration of ligand A in complexes RA_2 and RA_2B is twice of the concentration of the complexes.

$$\begin{aligned}
R_f &= R_t - (2[RA] + [RB] + [RA_2] + 2[RAB] + [RA_2B]) \\
&= R_t - \left(\frac{2R_f A_f}{K_{d1}} + \frac{R_f B_f}{K_{d2}} + \frac{R_f A_f^2}{K_{d1}^2} + \frac{2R_f A_f B_f}{K_{d1} K_{d2}} + \frac{R_f A_f^2 B_f}{K_{d1}^2 K_{d2}} \right) \\
A_f &= A_t - (2[RA] + 2[RA_2] + 2[RAB] + 2[RA_2B]) \\
&= A_t - \left(\frac{2R_f A_f}{K_{d1}} + \frac{2R_f A_f^2}{K_{d1}^2} + \frac{2R_f A_f B_f}{K_{d1} K_{d2}} + \frac{2R_f A_f^2 B_f}{K_{d1}^2 K_{d2}} \right) \\
B_f &= B_t - ([RB] + 2[RAB] + [RA_2B]) \\
&= B_t - \left(\frac{R_f B_f}{K_{d2}} + \frac{2R_f A_f B_f}{K_{d1} K_{d2}} + \frac{R_f A_f^2 B_f}{K_{d1}^2 K_{d2}} \right)
\end{aligned}$$

$$\begin{aligned}
F_i(t) &= F_A^i(t) + F_B^i(t) + F_R^i(t) + F_{RA}^i(t) \\
&\quad + F_{RA_2}^i(t) + F_{RB}^i(t) + F_{RAB}^i(t) + F_{RA_2B}^i(t) \\
&= N_A V_{eff} \left[\begin{aligned} &\eta_A^i A_f(t) + \eta_B^i B_f(t) + \eta_R^i R_f(t) + \eta_{RA}^i RA(t) + \eta_{RA_2}^i RA_2(t) \\ &\quad + \eta_{RB}^i RB(t) + \eta_{RAB}^i RAB(t) + \eta_{RA_2B}^i RA_2B(t) \end{aligned} \right]
\end{aligned}$$

where $\eta_{RA_n/B}^i = \eta_R^i + n\eta_{A/B}^i$ and $\eta_{RA_nB}^i = \eta_R^i + n\eta_A^i + \eta_B^i$

$$G_{ij}^+(0) = \frac{\eta_A^{ij}A_f + \eta_B^{ij}B_f + \eta_R^{ij}R_f + \eta_{RA}^{ij}RA + \eta_{RA_2}^{ij}RA_2 + \eta_{RB}^{ij}RB + \eta_{RAB}^{ij}RAB + \eta_{RA_2B}^{ij}RA_2B}{N_A V_{eff} \left[\begin{array}{c} \left(\begin{array}{c} \eta_A^i A_f + \eta_B^i B_f + \eta_R^i R_f + \eta_{RA}^i RA + \eta_{RA_2}^i RA_2 + \\ \eta_{RB}^i RB + \eta_{RAB}^i RAB + \eta_{RA_2B}^i RA_2B \end{array} \right) \\ \left(\begin{array}{c} \eta_A^j A_f + \eta_B^j B_f + \eta_R^j R_f + \eta_{RA}^j RA + \eta_{RA_2}^j RA_2 + \\ \eta_{RB}^j RB + \eta_{RAB}^j RAB + \eta_{RA_2B}^j RA_2B \end{array} \right) \end{array} \right]}$$

$$\text{where } \eta_{RA_n/B}^{ij} = \left(\eta_R^i + n\eta_{A/B}^i \right) \left(\eta_R^j + n\eta_{A/B}^j \right)$$

$$\text{and } \eta_{RA_nB}^{ij} = \left(\eta_R^i + n\eta_A^i + \eta_B^i \right) \left(\eta_R^j + n\eta_A^j + \eta_B^j \right)$$

The negative control is the same as that for the model of receptor with 2 binding sites.

5.4.10 Applications of multicolor SW-FCCS

The extension of FCCS to three colors diminishes the signal-to-noise ratio of the measurements since a narrower wavelength range is available for each channel and cross-talk between the channels will be larger. Nevertheless, the extension to three colors is important for at least two reasons. Firstly, the biological variability between cells is often so high that any correlations between distinct biomolecules are hidden and can only be detected when all relevant molecules are observed simultaneously in a cell. Secondly, complex biochemical reactions in cellular systems involve higher order molecular interactions. These interactions consist of temporal association and dissociation reactions that multicolor SW-FCCS has the potential to detect and monitor. For instance, the detection of binding of the various proteins involved in signaling complexes in a cellular environment over time can only be followed when the different interaction partners are labeled. To be able to detect these intermediate complexes, the lifetimes of these complexes have to be longer than the time it takes for the complexed molecule to diffuse through

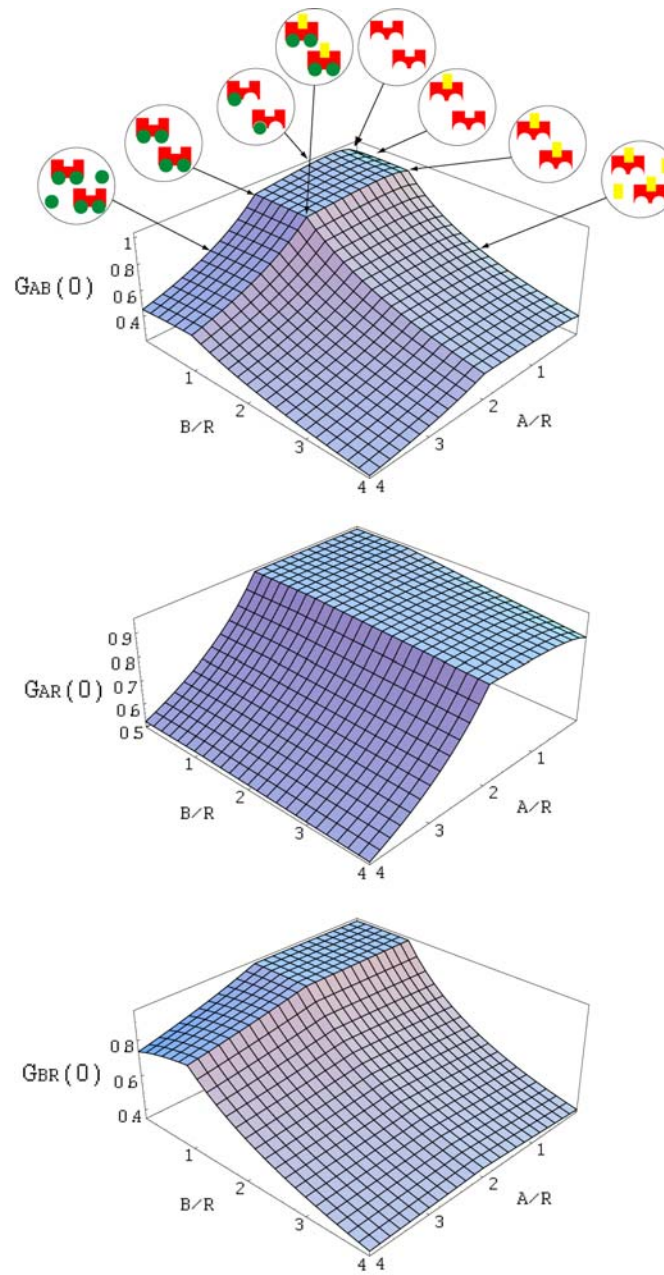


Figure 5.11: Simulations of cross-correlation amplitudes obtained from the binding of 2 ligands A (green) and 1 ligand B (yellow) to each receptor R (red). G_{AB} (top graph), G_{AR} (middle graph) and G_{BR} (bottom graph) are simulated at various combinations of A/R and B/R concentration ratios at $K_d = 10^{-15}M$ for all receptor-ligand interactions. The schematic drawing depicts the binding reaction at different ligand/receptor concentration ratios.

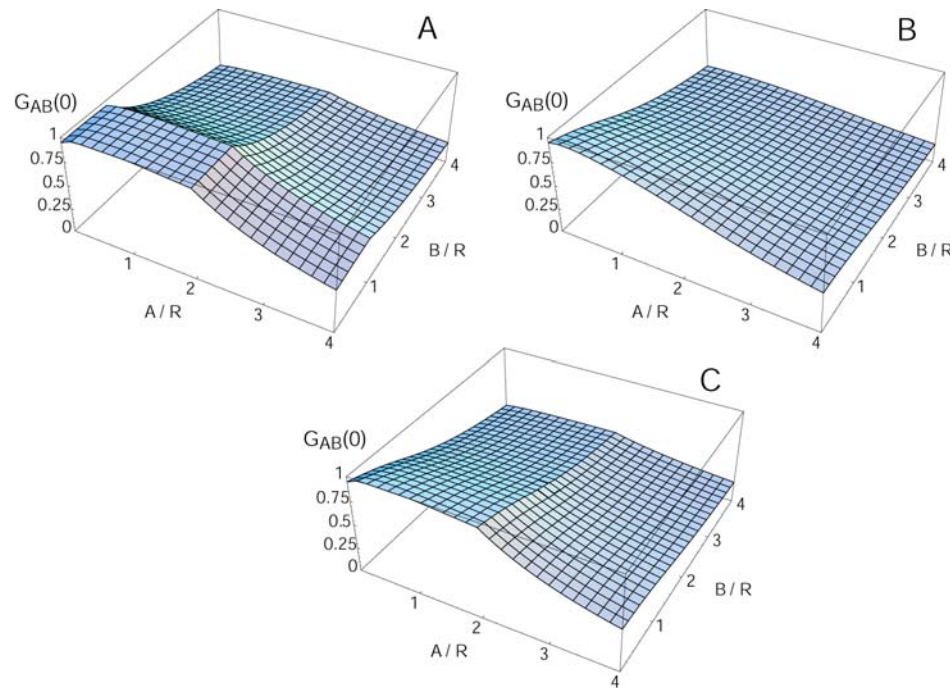


Figure 5.12: Determination of stoichiometry for complex RA_2B . Simulations of the positive control cross-correlation amplitudes $G_{AB}(0)$ for A/R and B/R are shown for (A) $K_d = 10^{-15}$ M and (B) $K_d = 10^{-9}$ M for both ligands A and B . The simulations were done using $V_{eff} = 0.35$ fl. The lines of inflection perpendicular to both the x- and y-axes represent the stoichiometry of the ligands A and B respectively i.e. $R : A : B = 1 : 2 : 1$. The lines of inflection becomes less pronounced as K_d s increases and the stoichiometry becomes less obvious. (C) Simulations of $K_{d1} = 10^{-15}$ M for ligand A and $K_{d2} = 10^{-9}$ M for ligand B . For this reaction where the K_{d1} for all ligands A is the same and K_{d2} is independent of each other, the binding curves of the ligands that lie on the x- or y-axes remain the same despite the second ligand having a different K_d .

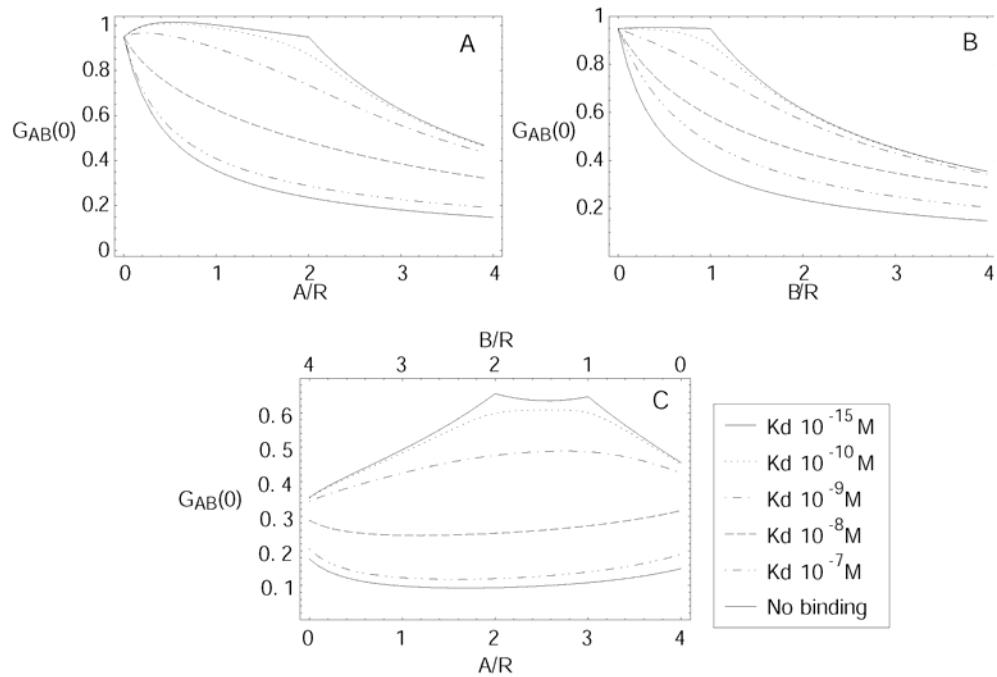


Figure 5.13: (A) Simulation of the $G_{AB}(0)$ binding curves at 0–4 A/R concentration ratios, with no ligand B . The curve cut-off point determines the stoichiometry of A at 2. (B) Simulation of the $G_{AB}(0)$ binding curves at 0–4 B/R concentration ratios, with no ligand A . The curve cut-off point determines the stoichiometry of B at 1. (C) Simulation of the $G_{AB}(0)$ binding curves at 0–4 A/R and 4–0 B/R ratios (view the diagonal cross-section of the 3D plot from $A/R = 4$ to $B/R = 4$). The stoichiometry of ligands A and B can be determined from the cut-off points of the curves where $A/R = 2$ and $B/R = 1$. These cut-off points become less defined as K_d of the reaction increases. Stoichiometry becomes then indistinguishable beyond $K_d = 10^{-9}$ M.

the observation volume and the characteristic times of the interactions have to be of the same order or longer than the measurement time that is limited by ~ 1 s for FC(C)S. If that is the case, SW-FCCS measurements with three colors can differentiate between trimers, dimers and monomers and can elucidate temporal sequence of biological interactions.

5.5 Conclusion

In this chapter, fluorescence multicolor cross-correlations was performed using single laser wavelength for the excitation and simultaneous detection of three spectrally distinct fluorophores. The independent binding of two differently labeled ligands to a receptor tagged with a third color was verified with the standard streptavidin-biotin system. Modeling the positive control curves with the described SW-FCCS theory enabled the determination of dissociation constants. Although several factors such as cross-talk, impurities and potential multiple labeling ratios may limit the accurate determination of K_d , it has been shown that the method is able to resolve the different possible complexes of three interacting molecules.

Multicolor SW-FCCS provides a fast and convenient method to offer yes or no answers to interacting biochemical systems, determines an upper K_d limit and the stoichiometry of binding. Existing FCS optical setups can be easily modified to perform SW-FCCS by including three detectors at the detection pathway whilst keeping the excitation path unchanged with one cw laser. Multiple laser excitation setups, in contrast, involve the complicated alignment of several laser beams in 3D to the same excitation volume and suffer from artifacts of non-ideal overlap of excitation volumes that arise because of chromatic aberrations. Compared to multi-photon FCCS, SW-FCCS utilizes one-photon excitation that not only uses less expensive lasers but also offers higher count rates per molecule and better signal-to-noise ratio [67]. In addition, recent advances in the setup of the detec-

tion pathways by using dispersive elements further simplify the setup and offer a simpler way of choosing wavelength ranges for detection and thus minimization of spectral cross-talk [87], which will be demonstrated in chapter 6.

SW-FCCS uses fluorophores that require similar excitation spectra but spectrally different emission characteristics with minimal cross-talk. It has been shown to work with tandem dyes, quantum dots and even with spectrally similar organic dyes. Experimental count rates per molecule for fluorescent proteins and small organic dyes with large Stokes shifts, both of which are potential fluorophores for this technique have been presented in Table 5.2. The high sensitivity of FCS and its ability to probe spatial and temporal reactions, coupled with the capability to detect multicolor labels simultaneously using single laser excitation, provides the opportunity to study higher order complex formation and molecular networks with a good signal-to-noise ratio in live cells. Potential applications include interactions involving membrane receptors and intracellular proteins involved in signaling networks.

Chapter 6

Prism-based Fluorescence Correlation Spectrometer

6.1 Introduction

With the advancement of fluorescence techniques towards multiplexing technologies, complex signaling networks and higher order biomolecular interactions probed with multiple labels can be simultaneously studied. Chapters 3–5 have described such techniques that apply dual and multicolor FCCS using single laser wavelength excitation. SW-FCCS setups use conventional instrumentation including dichroic mirrors and emission filter sets to select the desired emission wavelengths or separate them into different detection channels. For multiple wavelength detection, multiple dichroics and emission filters will have to be used. Not only does this complicate the setup it also amplifies the intensity losses due to non-ideal transmission, principally surface reflections through each optical component. Commercially available emission filters and dichroics have usually broad spectral bandwidths and rise/fall bandwidths respectively. Unless each detection window of the filter is customized to overlap with the emission spectra of the probes, the difficulty of balancing between optimizing signal detection and reducing spectral cross-talk will augment with each additional detection channel.

To overcome these problems, a dispersive element such as a diffraction grating or a prism could be used to spectrally separate the emission light. Prism and grating spectrographs have been implemented with the confocal scanning laser microscope to acquire emission spectra [145, 146] for applications in FRET imaging [147, 148] and FLIM studies [149]. Multicolor fluorescence imaging using a single laser wavelength excitation was also applied on quantum dots for colocalization studies [90]. Commercial confocal microscopes now utilize parallel detection channels for multicolor imaging. Zeiss LSM510 Meta uses a grating for the spectral dispersion of the signal onto a PMT array and the Leica TCS SP2 AOBS uses a prism as a spectral dispersion element and a scanning PMT detector [150–153]. On the other hand, the only reported FCS systems that used dispersive elements were conceived for filtering the scattered excitation light and Raman scattering of water using a prism monochromator for rotational FCS experiments [41]; and most recently a grating-based detection setup consisting of a fiber array coupled to individual APDs developed for simultaneously measuring autocorrelations of four distinct quantum dots [87].

This chapter demonstrates the use of a dispersive element in the detection path to spectrally disperse the fluorescence emission. A prism-based spectrometer is designed, constructed and combined with a FCS system with single laser excitation. The reason for using a prism is the cost effectiveness and higher efficiency as compared with diffraction gratings, which lose part of the light due to multiple diffraction orders. The dispersion by the prism spectrometer causes a wavelength-dependent deflection angle such that the fluorescence signal can be focused on well separated spots for the spectral ranges of interest. An optical fiber scanned through these foci selects different spectral ranges for detection and autocorrelation of standard and tandem dyes. The single fiber was then replaced with an optic fiber array to detect signals from two channels for cross-correlation. The binding of biotinylated rhodamine green polymeric vesicles (or nanocontainers) and AXSA was tested on the prism-based setup as a proof of principle. The

prism-based fluorescence correlation spectrometer has established a wavelength tunable and filter-free setup for multicolor correlation spectroscopy. This is an important step towards multiplexing technologies for high throughput screening of molecular interactions.

6.2 Materials and Methods

6.2.1 Prism spectrometer

A schematic diagram of the prism-based fluorescence correlation spectrometer is shown in Fig. 6.1. An argon-ion laser (Lasos Lasertechnik GmbH) emitting at an excitation wavelength of 488 nm is used for the excitation of several fluorophores. The laser beam diameter is expanded with two planar convex lenses L1 ($f = 25$ mm) and L2 ($f = 100$ mm) and coupled into the back aperture (diameter = 11 mm) of the objective (Olympus 40x, NA 1.15) mounted onto a Zeiss Axiovert 100 (tube lens, L3: $f = 164$ mm). Fluorescence emission from the sample is collected by the objective and separated from the backscattered excitation light with a dichroic mirror DM (Q505LP, Chroma). The fluorescence light is focused by the microscope tube lens L3 ($f = 164$ mm) into a 50 μ m pinhole. An achromat L4 ($f = 100$ mm) collimates the emission light, which passes then a 30° isosceles prism (Linos) dispersing the fluorescence light. The focusing lens L5 (achromat $f = 120$ mm) brings the dispersed wavelengths into focus at different positions in the focal plane. A 1.2 times magnified image of the pinhole is formed for each wavelength, distributed on the image plane. The desired wavelength range is defined by the core diameter and the position of the optic fiber at the image plane.

There are several factors influencing the desired wavelength range to be detected: (1) the core diameter of the optic fiber acting as a slit width for the spectrometer. The core diameter determines the spectral bandwidth whilst the distance between the fiber cores determines the size of spectral channel separa-

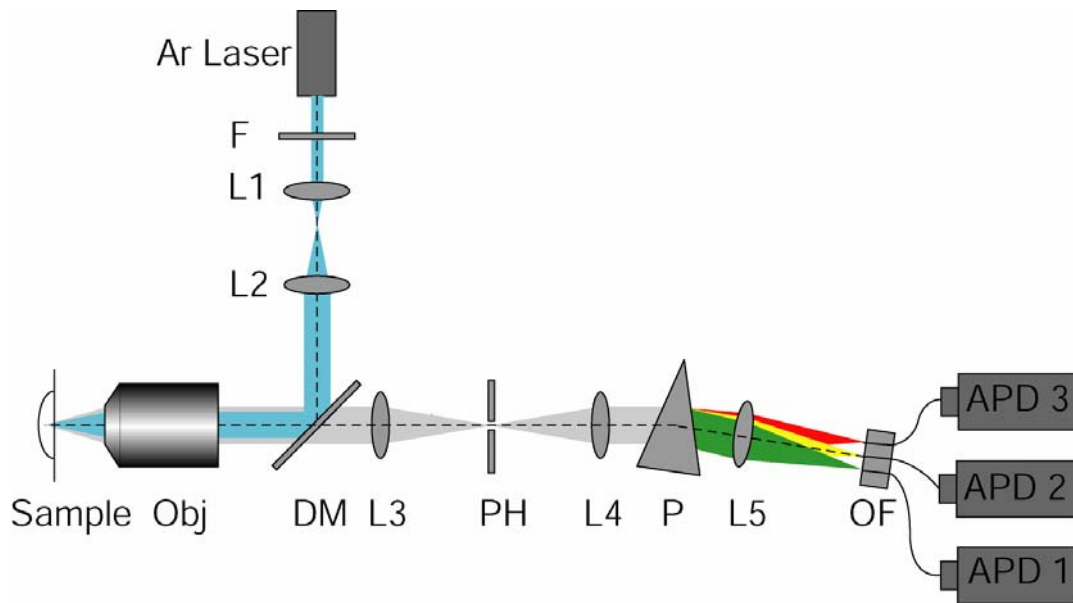


Figure 6.1: Optical setup of prism-based FCSpectrometer. A single laser wavelength excites several fluorescent species. The emitted light is collimated and chromatically dispersed by an isosceles prism and focused onto an array of optical fibers that are coupled to avalanche photodiodes. F: excitation filter; Obj: microscope objective; L1-L5: lenses; DM: dichroic mirror; PH: pinhole; P: dispersive prism; OF: optical fibers; APD1-3: avalanche photodiodes.

tion; (2) the focal length of the focusing lens. A longer focal length increases the linear deflection of the wavelengths at the image plane; (3) the size or angle of the prism. A larger prism (60° equilateral) will have a higher dispersion than a smaller prism (30° isosceles); and (4) the spot size in the image plane. To achieve good spectral filtering, it is important to keep the ratio of core diameter to spot diameter high while keeping the focusing NA below the acceptance angle of the fiber. When detected by the optic fiber array, a larger deflection of wavelengths at the image plane will result in a narrower bandwidth of the detected wavelengths and a smaller separation between each spectral channel. A larger spectral bandwidth will increase the amount of signal collected and a broader channel separation will reduce cross-talk between the detection channels. In addition, this depends on the overlap of the emission spectra and the peak emission wavelengths of the fluorophores with the cores of the optic fibers. All these factors were taken into account when the setup was first simulated and optimized with an optical design software (Zemax, USA). The Zemax results (shown in the appendix) are verified

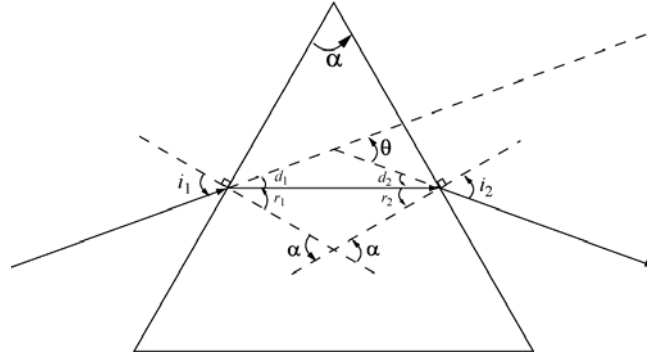


Figure 6.2: Deviation of a ray through a prism

with calculations presented below.

The refractive index of the optical medium, in this case the prism, varies with the wavelength of the incident ray. The prism separates the colors of a beam of white light into differently directed beams; with the shorter wavelengths emerging at larger angles than longer wavelengths. These wavelength-dependent exit angles are measured by the angular dispersion $\Delta\theta(\lambda)$. The angular dispersion $\Delta\theta(\lambda)$ leads to a linear shift of the focal positions $\Delta y(\lambda)$ in the image plane. This linear dispersion is expressed as $\Delta y(\lambda)$ where Δy is the displacement against a reference wavelength λ_{ref} . Fig. 6.2 shows the path of a ray through a prism of refracting angle α . The deflection angle of the ray passing through the prism is θ , therefore [154, 155],

$$\alpha = r_1 + r_2 \quad (6.1)$$

$$\begin{aligned} \theta &= d_1 + d_2 \\ &= i_1 - r_1 + i_2 - r_2 \\ &= i_1 + i_2 - (r_1 + r_2) \\ &= i_1 + i_2 - \alpha \end{aligned} \quad (6.2)$$

When the ray traverses the prism symmetrically and emerge at a minimum deviation angle, $i_1 = i_2$ and $r_1 = r_2$. Eq. 6.2 becomes $\theta = 2i - \alpha$ and

$$i = \frac{\theta + \alpha}{2} \quad (6.3)$$

Also, since $\alpha = r_1 + r_2 = 2r$

$$r = \frac{\alpha}{2} \quad (6.4)$$

Snell's Law of Refraction [156] is then given by

$$n_o \sin i = n \sin r \quad (6.5)$$

$$n = \frac{\sin i}{\sin r} = \frac{\sin \frac{\theta + \alpha}{2}}{\sin \frac{\alpha}{2}} \quad (6.6)$$

where $n_o = 1.0$ for the refractive index of air, and n the refractive index of the glass depending on the wavelength of the incident light. This refractive index n is given by Sellmeier's equation [157] where the constants of dispersion for the glass material N-BK7 [158] is given in Table 6.1.

$$n^2(\lambda) - 1 = \frac{B_1 \lambda^2}{(\lambda^2 - C_1)} + \frac{B_2 \lambda^2}{(\lambda^2 - C_2)} + \frac{B_3 \lambda^2}{(\lambda^2 - C_3)} \quad (6.7)$$

N-BK7	Dispersion constants
B_1	1.03961212
B_2	0.231792344
B_3	1.01046945
C_1	0.00600069867
C_2	0.0200179144
C_3	103.560653

Table 6.1: Table of dispersion constants of prism material N-BK7 from Schott Catalog

Since $\alpha = 30^\circ$ and $n = 1.51712182$ at a reference wavelength $\lambda_{ref} = 580 \text{ nm}$, these values are substituted into Eq. 6.6 to obtain $\theta = 16.24^\circ$. The incident and emergent angles are then calculated to be $i = 23.12^\circ$ from Eq. 6.3. And given that $d_1 = d_2 = i_1 - r_1 = i_2 - r_2 = 23.12^\circ - 15^\circ = 8.12^\circ$, i.e. the prism has to be tilted by 8.12° in order to pass the rays at minimum deviation angle, hence with maximum transmission efficiency. The angle of dispersion as a function of wavelength is calculated for all other wavelengths using Eq. 6.2 and Snell's Law

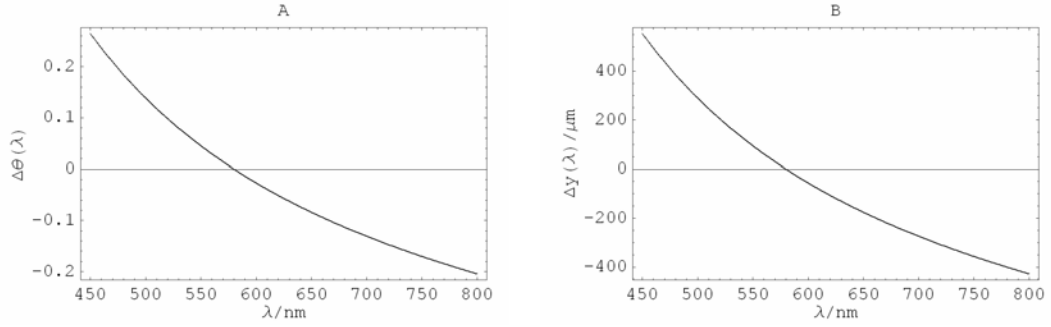


Figure 6.3: (A) Change of angular dispersion $\Delta\theta(\lambda)$ in degrees and (B) lateral displacement $\Delta y(\lambda)$ with wavelength caused by the prism dispersion. The dispersion depends on the glass material of the prism.

to give

$$\theta(\lambda) = i_1 + \arcsin\left(n \sin\left(\alpha - \arcsin\left(n^{-1} \sin i_1\right)\right)\right) - \alpha \quad (6.8)$$

The angular dispersion for each emergent wavelength is determined with respect to λ_{ref}

$$\Delta\theta(\lambda) = \theta(\lambda) - \theta(\lambda_{ref}) \quad (6.9)$$

The lateral displacement of the dispersed wavelengths from λ_{ref} is defined by geometrical optics and given by the product of the focal length of the focusing lens L5 and the angular dispersion.

$$\Delta y(\lambda) = f \cdot \Delta\theta(\lambda) \quad (6.10)$$

Due to the non-linear dispersion of the prism (as shown from Eq. 6.7), the lateral displacement is not linear with respect to wavelength. Fig. 6.3 shows the angular dispersion $\Delta\theta(\lambda)$ and lateral displacement $\Delta y(\lambda)$ versus wavelength with respect to the reference wavelength of 580 nm.

6.2.2 Calibration with a single optic fiber

To first demonstrate that FCS can be performed with a prism as a dispersive element, a single 100 μm multimode optical fiber (Thorlabs) was scanned along the image plane. The beam diameter and focal length of lens L5 resulted in a

NA of 0.028, much smaller than the fiber NA 0.22 which assured optimal coupling efficiency of the fiber. An APD (SPCM-AQR-14, Perkin Elmer) was used for detecting single photons. The detector signal was autocorrelated by a hardware correlator (Flex02-12D, correlator.com). The system was calibrated with a standard fluorophore, Rhodamine green (RhG) and a tandem dye, AXSA having two emission peaks at 575 nm and 667 nm (emission spectra shown in Fig. 6.4). Optimum laser powers of 600 μW for RhG and 50 μW for AXSA were used to obtain high photon count rates at minimum photobleaching. The fiber was aligned for maximum count rates in the green, yellow and red channels respectively. From the fits of the autocorrelation curves, the ratio of axial to radial dimensions of the confocal volume K was measured between 2 and 4. We measured a diffusion time of 134.5 μs for RhG. Using the diffusion coefficient of Rhodamine of $2.8 \times 10^{-6} \text{ cm}^2/\text{s}$ [36], the beam cross-section radius and the effective confocal volume were determined to be 390 nm and 0.89 fl, respectively. Cpm calculated from the autocorrelation curves, 26.5 kHz (RhG in green channel), 9.5 kHz (AXSA in yellow channel) and 47.2 kHz (AXSA in red channel), were corrected for laser background in the blue region and Raman scattering of water in the yellow region. The cpm for RhG was reduced by about 60% as compared with a FCS setup using emission bandpass filters for wavelength selection. This reduced cpm is partly due to the narrower spectral bandwidth of the green channel (19 nm as calculated below) collected by the optic fiber as compared with the bandpass filter with a spectral range of 40 nm. Another reason for lower cpm is the light losses from reflection and scattering at each optical surface. This can be improved by using optics with anti-reflective coating.

6.2.3 Calibration with an optic fiber array

The optical fiber array consisted of an optic fiber array holder with grooves to fix $3 \times 105 \mu\text{m}$ core diameter bare fibers with 250 μm of cladding and acrylate jacket (AFS105/125Y, Thorlabs). The bare fibers did not have outer jackets such

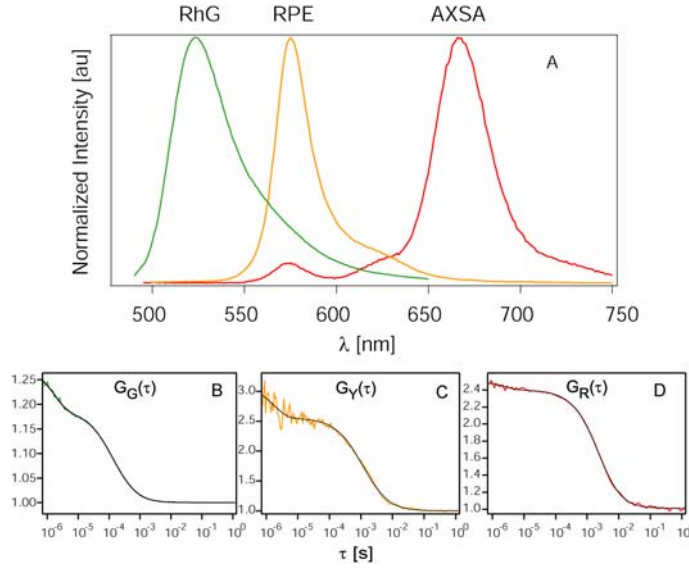


Figure 6.4: (A) Emission spectra of fluorophores used for the FCS experiments. The spectrum of AXSA shows two emission peaks at 575 nm and 667 nm. The spectrum of RPE is included to illustrate the normalized intensity profile at 575 nm when no FRET occurs. The autocorrelation functions of (B) RhG in the green channel, (C) AXSA in the yellow channel and (D) AXSA in the red channel.

that the core centers were separated by 250 μm when clamped next to each other. This design ensured that the dimensions of the optic fiber cores overlap as much as possible with the lateral displacements of the emission wavelengths of the fluorophores to obtain a sufficiently high detection efficiency in each channel; yet minimizing cross-talk between the detection channels. The detection efficiency of a fiber for wavelength λ is given by the overlap integral of the wavelength dependent image with the fiber core. For monochromatic light with wavelength λ , the effective image of a point emitter results in an intensity profile in the image plane equal to the PSF of the system. The PSF is approximated by the Airy disk (Eq. 6.11), where r is the radial position and r_a the Airy radius ($r_a = 0.61\lambda/NA$) [156]

$$PSF(\vec{r}) = \left(\frac{2J_1(\pi\vec{r})}{(\pi\vec{r})} \right)^2 \quad (6.11)$$

where J_1 is the Bessel function of the first kind of order 1. In this case, the point emitter is moving through the excitation volume with waist w_o . The image is formed by the convolution of the diffraction limited point spread function with the excitation intensity, to obtain the average image intensity profile of dyes diffusing

through the excitation volume.

$$I(\vec{r}) \propto PSF(\vec{r}) \otimes I_{ex}(\vec{r}/M) \quad (6.12)$$

$$= \int \int PSF(\vec{r}) I_{ex}((\vec{r}' - \vec{r})/M) d\vec{r}' \quad (6.13)$$

where M is the magnification of the system ($M = 40 \times \frac{164 \text{ mm}}{180 \text{ mm}} \times \frac{120 \text{ mm}}{100 \text{ mm}} = 43.7$) and the Gaussian excitation profile of the laser is given by

$$I_{ex}\left(\frac{\vec{R}}{M}\right) = \exp\left(-2\frac{R^2}{M^2 w_o^2}\right) \quad (6.14)$$

The excitation profile and the PSF are both rotationally symmetric. Therefore the image intensity is also rotationally symmetric. The convolution is evaluated in polar coordinates and limits the calculation to $r \in [0, \infty]$. The excitation intensity is then computed for $\theta \in [-\pi, +\pi]$ for the radii R . From the cosine law (similar to Fig. 6.5),

$$R^2 = r^2 + r'^2 - 2rr' \cos \phi \quad (6.15)$$

the image intensity becomes

$$I(\vec{r}) \propto \int_0^\infty r PSF(r) dr \int_{-\pi}^{+\pi} I_{ex}\left(\frac{\vec{R}}{M}\right) d\theta \quad (6.16)$$

The PSF is convoluted with the Gaussian excitation profile. Although the intermediate pinhole provides the spatial filtering of the optical system and determines the size of the sampling volume (see chapter 2), the intermediate image is typically hardly distinguishable from a Gaussian profile with somewhat a larger waist. If the diameter of the intermediate pinhole is carefully chosen, the transmission is near 100% for light originating from the sampling volume and the intermediate image is not affected much. Under the conditions stated above, the image on the fiber ends is of approximately Gaussian shape with diameter and y position depending upon the emission wavelength. The coupling efficiency is then approximated by the overlap intergral with the fiber core.

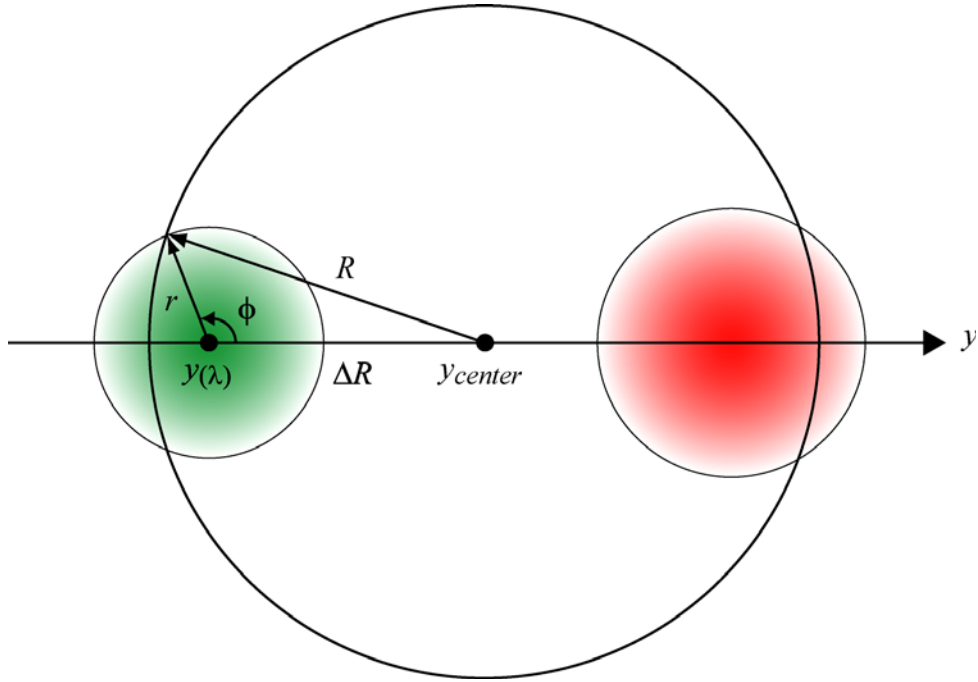


Figure 6.5: Schematic drawing of two imaged spots of different wavelengths, green (left circle) and red (right circle) focused onto an optic fiber core (larger middle circle). The transmission function of a fiber for wavelength λ is given by the overlap integral of the wavelength dependent image with the fiber core.

After normalization of the image intensity, the transmission $T(\lambda)$ into the fiber is obtained by evaluating the overlap integral with the fiber core.

Fig. 6.5 shows the center of the fiber core y_{center} and the center of the image $y(\lambda)$ as a function of the dispersed wavelength of the image. R is the fiber core radius and r is the radius from the image center. Both the fiber core and the image are rotationally symmetric. Hence polar coordinates (ϕ, r) are used and the 2D integration can be reduced to a 1D integration along the radius r . The centers of the image and the fiber core are at a distance of

$$\Delta R = |y(\lambda) - y_{center}| \quad (6.17)$$

The cosine law states that

$$R^2 = r^2 + \Delta R^2 - 2r\Delta R \cos \phi \quad (6.18)$$

$$\phi = \arccos \left(\frac{r^2 + \Delta R^2 - R^2}{2r\Delta R} \right) \quad (6.19)$$

When $r < R - \Delta R$, the integrand is non-null over the full circle, i.e. over an angle of 2π rad. When $r > R - \Delta R$, the integrand is non-null over an angle of 2ϕ only. To calculate the transmission $T(\lambda)$ of a fiber over the full spectral range this integral is computed for $\lambda = 450 \text{ nm} - 800 \text{ nm}$.

$$T(\lambda) = 2 \int_0^{R-\Delta R} I(r) r \pi dr + 2 \int_{|R-\Delta R|}^{R+\Delta R} I(r) r \phi(r) dr \quad (6.20)$$

The prism dispersion leads to a lateral shift $y(\lambda)$ of the image with the wavelength. A lateral displacement of the fiber allows the selection of different wavelength ranges, whereas the bandwidth is proportional to the core diameter. Fig. 6.6 shows the calculated spectral bandwidths of 19 nm, 29 nm and 45 nm at FWHM for the blue, yellow and red detection channel, respectively. The steepness of the spectral filtering of the FCSpectrometer i.e. the fall-off from 90% to 10% transmission was calculated to 4–11 nm for the three detection channels. For comparison, commercial bandpass filters and dichroic mirrors achieved a cut-off within 5 nm and 15–25 nm, respectively. Here, to show the simultaneous auto and cross-correlations of two binding components, the fibers were clamped at alternate grooves and mounted the holder on an micrometer xyz translation stage. Calibration measurements were again repeated with the same dyes. The green channel was aligned to an optimum cpm for RhG of 21 kHz. The red channel had a cpm of 9 kHz for AXSA.

6.2.4 Correlation experiments with fiber array

For cross-correlation measurements, 5% biotinylated nanocontainers filled with RhG [159] were measured with AXSA to detect biotin-streptavidin complexes. Nanocontainers were prepared by dispersing amphiphilic triblock copolymers in an aqueous solution. Amphiphilic triblock copolymer (PMOXA-PDMS-PMOXA, JW 05) with an average molecular weight of around 8000 g/mol, was synthesized using an established procedure [160]. A sample droplet of RhG nanocontainers was

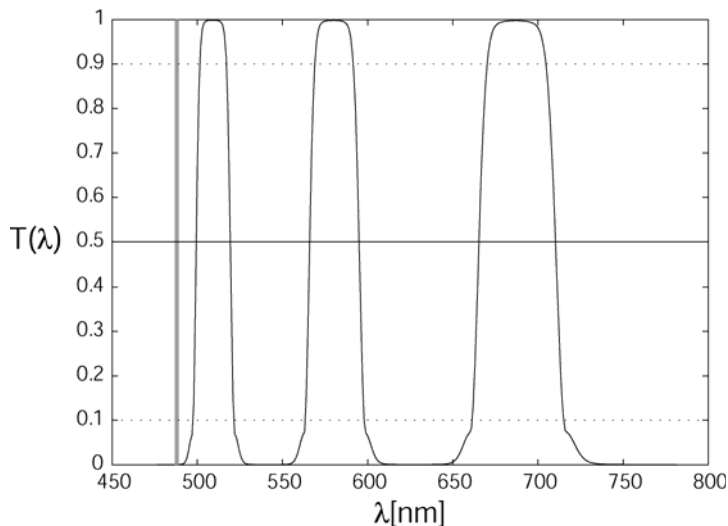


Figure 6.6: Plot of transmission $T(\lambda)$ versus wavelength shows the laser line 488 nm and the spectral bandwidths calculated for optic fibers with core diameters 105 μm with cladding and buffer diameters 250 μm .

first measured to give an autocorrelation curve in the green channel. As a negative control, all AXSA biotin-binding sites were first saturated with excess unlabeled biotin (100 μM) before pipetting a 3 μl of inhibited AXSA (30 nM) onto a 10 μl sample droplet of RhG nanocontainers (3.5 nM). Binding experiments were performed by pipetting 3 μl AXSA (30 nM) onto another sample droplet of active RhG nanocontainers (3.5 nM). 20 FCS measurements, each for an interval of 20 s, were taken during and after the titration.

6.3 Results and Discussion

6.3.1 Correlation experiments

Since there was negligible crosstalk observed from RhG into the red channel, there was no autocorrelation measured in the red channel due to RhG. For the negative control, no intensity spikes or cross-correlations were observed between the green and red channels in all the measurements (Fig. 6.7 B) despite autocorrelation curves in both green and red channels (Fig. 6.7 A). For the binding experiments, no cross-correlation was observed when the sample droplet of RhG nanocontain-

ers was initially added. When AXSA was added to the sample droplet, oligomers started forming between the nanocontainers and AXSA 170 s after mixing both solutions together. This was evident from the intensity spikes coming from single complex molecules diffusing through the observation volume and the rising CCF amplitude (Fig. 6.7 D). It was observed from the intensity traces that large intensity spikes were coming from the red channel. This is explained by the aggregation of AXSA molecules to each nanocontainer, causing also intensity spikes in the ACF of AXSA towards long diffusion times (Fig. 6.7 B, red curve). The magnitude of each intensity spike is then proportional to the number of AXSA molecules bound to each nanocontainer.

6.3.2 Design of prism spectrometer

The cpm of the fluorophores, hence a signal-to-background ratio measured on the spectrometer is lower than that measured on the FCS setup. This is partly due to the narrower spectral bandwidth of the spectrometer. This could be increased by using a focusing lens with a smaller focal length or an optic fiber with a larger core diameter to collect a wider range of wavelengths. However this is only feasible for a single optic fiber used to scan across the focus plane. Due to the non-linear dispersion of the prism, the fiber will have a larger spectral bandwidth towards longer wavelengths (Fig. 6.6). At the same time, the separation between the spectral channels increases and the fibers will no longer collect light at the peak intensities of the fluorescence emission. Other light losses also occur from reflections and scatterings at each prism and lens surface and absorption in the glass material. The signal-to-background ratio could be improved by using anti-reflective coated prism in the detection path.

Calibration measurements performed with the optic fiber array made use of bare fibers which are more susceptible to light losses than fibers protected with outer jackets. This was evident from the lowering of cpm for RhG in the green channel (26.5 kHz \rightarrow 21 kHz) and AXSA in the red channel (47.2 kHz \rightarrow 9

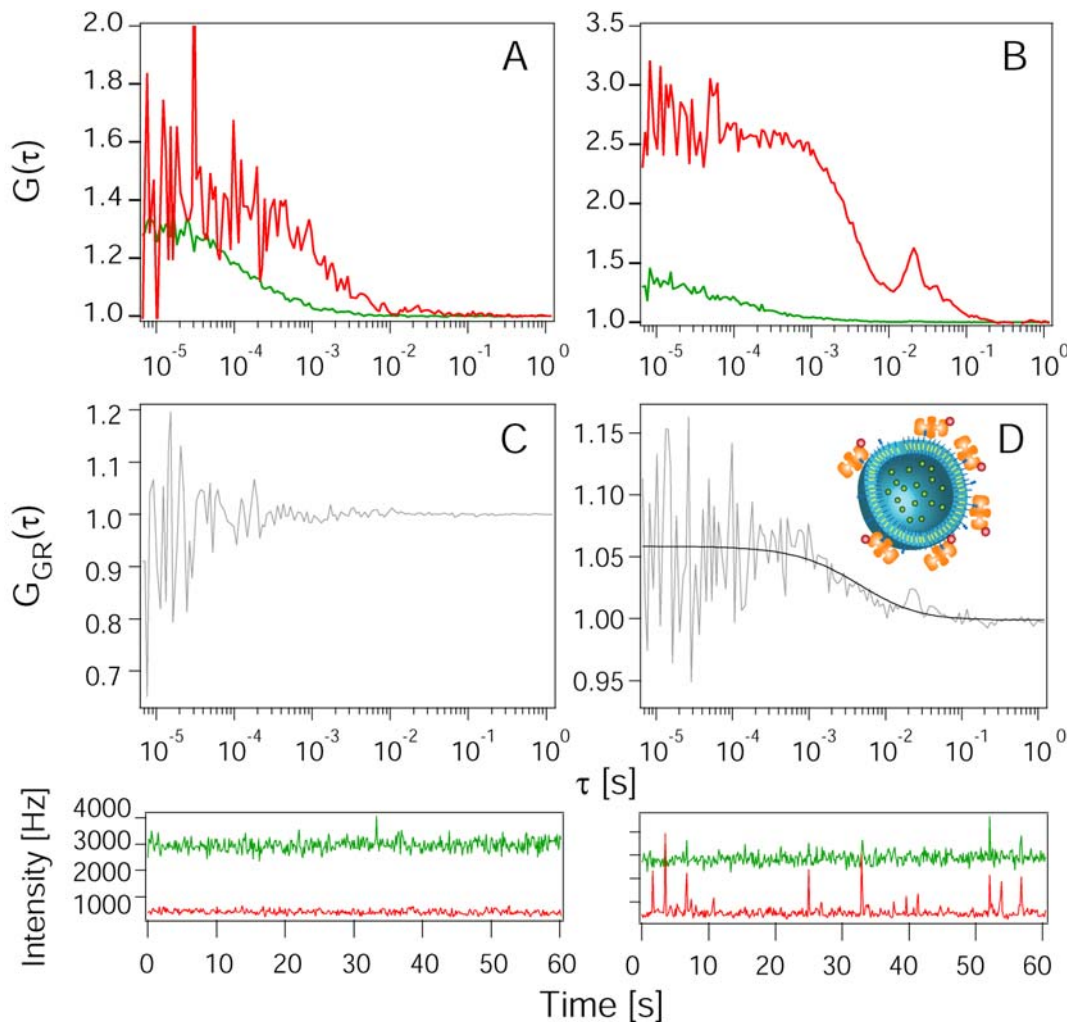


Figure 6.7: Auto- and cross-correlation curves of green and red channels. Negative control of biotinylated RhG nanocontainers and AXSA are depicted by the (A) autocorrelation curves of RhG nanocontainers (green curve) and AXSA (red curve); (C) shows no crosscorrelation or intensity spikes from binding. Binding of biotinylated RhG nanocontainers and AXSA are depicted by the (B) autocorrelation curves of RhG nanocontainers (green curve) and aggregated AXSA show up on the autocorrelation (red curve); (D) positive cross-correlation confirms binding and red intensity spikes demonstrate oligomerization of AXSA to the nanocontainers. Inset: schematic drawing of the dual-color complex. Correlations were measured for 20 times for 60 s each with laser line 488 nm at power $50 \mu\text{W}$.

kHz). Furthermore, the cpm of the dyes in both channels decreased again when both of the fibers were realigned to measure simultaneously. This is because in the simulations, the peak emission wavelengths of the fluorophores could not be positioned to exactly overlap with each of the center of the fiber cores. Hence in actual calibrations, the fibers could not collect the optimum cpm from each fluorophore in the detection channels. This constraint is due to the non-linear dispersion of the prism and the difficulty of aligning the fibers with the fixed dimensions of the core and cladding/jacket diameters. To allow the optimization of detection ranges for each fiber individually, the fibers could be fixed separately and aligned independently. However the alignment of the fibers will have to change each time a fluorophore with different emission wavelengths are used. A better alternative is to use a Silicon photodiode array of up to 76 elements (Hamamatsu, Japan) to detect the whole spectrum, then selecting the detector elements that coincide with the peak emission wavelengths for improving the cpm. A highly sensitive CCD camera could be used to combine imaging and off-line correlations [161]. A grating-based setup could also be used for the advantage of linear dispersion and has been shown to work with FCS, however detection efficiency decreases mainly due to light losses in higher diffraction orders [87]. The prism-based spectrometer presented here achieved cpm more than doubled compared with results obtained when measuring fluorophores and QDs on a grating setup.

6.4 Conclusions

This chapter shows the experimental realization of a prism-based fluorescence correlation spectrometer using a single laser excitation wavelength. The prism spectrometer selects the emission wavelengths for correlation analysis without the use of dichroic mirrors and emission filters.

Calibration of the prism setup has been performed with two fluorescent dyes, RhG and AXSA, simultaneously excited at the same laser line. The fluorescence

emission at three different wavelength ranges were detected sequentially by a single optic fiber and three autocorrelation functions were obtained. The effective observation volume determined by the calibration of RhG was found to be comparable to that measured on a typical FCS setup. However, the count rate per molecule obtained for RhG was lower because of the narrower spectral bandwidth of the prism bandpass as compared with a commercial emission bandpass filter on a FCS setup.

A fiber optic array was aligned along the dispersed foci in the image plane to measure simultaneous FCS and FCCS of several binding components. Streptavidin-biotin was used as a model receptor-ligand binding system to test the performance of the setup for detecting molecular interactions. The positive cross-correlation curve and the intensity spikes of the complexes verify the binding of biotinylated RhG nanocontainers and AXSA. This result was confirmed with the negative control showing no cross-correlation.

The spectral range and efficiency of the prism spectrometer depend on the positioning and the dimensions of the optic fibers. Difficulty was encountered in maximizing the overlap of the prism bandpass with the emission spectra. This was due to constraints arising from non-linear dispersion of the prism and the fixed dimensions of the fibers. An alternative method is to use continuous detector elements instead of a point detector, such as an APD/PMT array or a CCD camera for a more flexible selection of multiple wavelength ranges.

The results here show a novel implementation of a wavelength tunable and filter-free prism-based detection for fluorescence correlation experiments. With increasing number of fluorophores namely tandem dyes and quantum dots that can be excited with a single laser wavelength and emit at separate wavelengths, the prism-based fluorescence correlation spectrometer is a promising tool to investigate and quantify single molecule dynamics and interactions in multicomponent biological systems.

6.5 Appendix: Zemax simulations

Surf#	Type	Comment	Radius	Thickness	Class	Semi-Diameter	Conic	Par 1 (unused)	Par 2 (unused)	Par 3 (unused)
001	Standard		Infinity	Infinity		0.000000	0.000000			
010	Standard		Infinity	20.000000		5.500000 U	0.000000			
2	Paraxial			0.000000		20.000000 U		100.000000	0.000000	
3	Standard		Infinity	180.000000		5.500000	0.000000			
4*	Standard		Infinity	180.000000		10.000000 U	0.000000			
5	Standard	026-1130	61.400000	5.200000	BN7	12.700000 U	0.000000			
6	Standard	OPTOICHA	-43.253000	2.500000	SF2	12.700000 U	0.000000			
7	Standard	F100	-138.000000	0.000000		12.700000 U	0.000000			
8	Standard		Infinity	60.000000		3.696111	0.000000			
9	Coord Break			0.000000	-	0.000000		0.000000	0.000000	0.170930 V
10	Tilted	33 3300		15.529143	BN7	28.977775 U	0.000000	0.000000	0.267949	
11	Tilted	LINUS 30DEG PRISM		0.000000	-	28.977775 P	0.000000	0.000000	-0.267949 P	
12	Coord Break			40.000000	-	0.000000		0.000000	0.000000	6.170930 P
13	Standard	322309	55.432373	5.000000	BN7	12.700000 U	0.000000			
14	Standard	LINOS	-50.482104	2.200000	F4	12.700000 U	0.000000			
15	Standard	F120	-640.204866	0.000000		12.700000 U	0.000000			
16	Standard		Infinity	112.951600 V		3.120478	0.000000			
17A	Standard		Infinity			0.511593	0.000000			

Figure 6.8: Zemax software configurations for the design of the prism-based fluorescence correlation spectrometer.

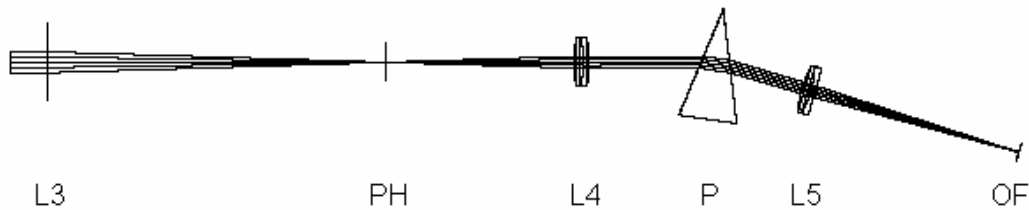


Figure 6.9: Zemax simulation of the prism-based fluorescence correlation spectrometer detection path. The fluorescence emission is focused by the tube lens L3 ($f = 164\text{mm}$) of the microscope. A pinhole PH ($50\ \mu\text{m}$) spatially filters the emission light and an achromat lens L4 ($f = 100\text{mm}$) collimates the beam onto a 30° isosceles prism. The prism chromatically disperses the fluorescence light and is focused by an achromat lens L5 ($f = 120\text{mm}$) onto the image plane where the optical fibers (OF) are positioned and coupled to avalanche photodiodes.

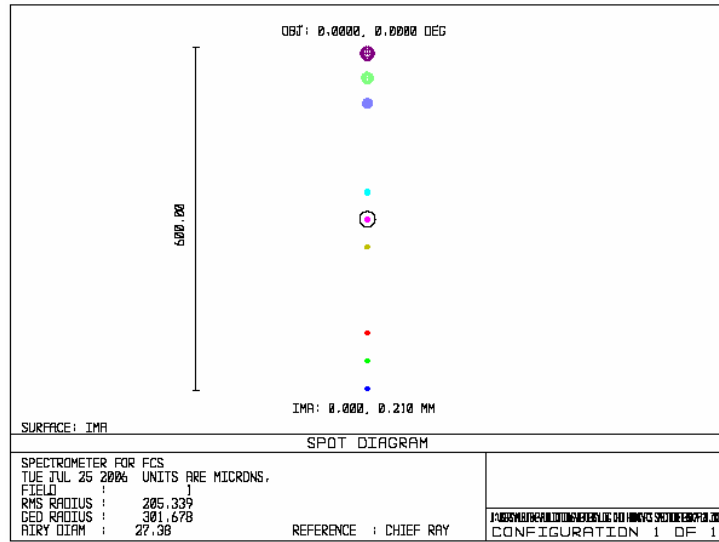


Figure 6.10: Zemax simulations of spot images produced by the prism-based FC-Spectrometer. Each spot represents the center or the edges of the fiber cores (core diameter = $100 \mu m$, buffer diameter = $250 \mu m$). The spot images are ordered from the shortest to the longest wavelengths from bottom to top. The size of the Airy disk is marked by a circle at the central reference wavelength of 580 nm.

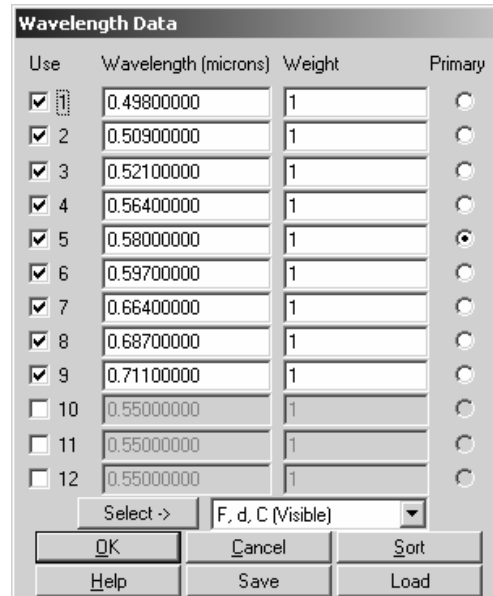


Figure 6.11: Zemax simulations of the wavelength data representing the center and limits of each fiber core as shown in the spot images. Wavelength 5 of 580 nm is the reference wavelength.

Chapter 7

Conclusions and Outlook

The objective of this thesis was to develop a fluorescence fluctuation spectroscopy method for the study of molecular interactions. This was achieved by providing the theoretical framework and experimental realization of dual- and triple-color SW-FCCS.

The optical setup of dual-color SW-FCCS was described in chapter 2 and the theory and experiments outlined in chapter 3. This section answers the question if it is possible to use a single laser wavelength for the excitation of two different fluorophore species and measure their molecular interaction by cross-correlation. With the recent advent of newly engineered fluorophores that can be excited with a single laser but emit with varying Stokes shifts, these dyes have been applied in this work for SW-FCCS. For proof-of-principle, the receptor-ligand streptavidin-biotin was used as a model binding system. Binding was shown from the cross-correlation amplitudes between green-emitting BF and red-emitting QR or QD655 conjugated to streptavidin. The changes in cross-correlation amplitudes with respect to ligand concentration was analyzed and the stoichiometry and binding constant of streptavidin-biotin were determined. Although this was several orders of magnitude far away from values obtained from conventional ensemble techniques ($K_d = 10^{-15}$ M), they were in accordance with values obtained with single molecule fluorescence techniques. One reason could be the experiments

were conducted at the concentration limit of FCS and FCCS, hence lowering the sensitivity at the detection range measured. Another likely reason is the large size of the fluorophore tag conjugated to the binding protein that could affect the steric accessibility of the binding sites [101].

The resolution of dual-color SW-FCCS to detect binding was described in chapter 4. There, the factors affecting the resolution of the technique for binding studies were analyzed and presented. Using dyes with similar spectral characteristics, TMRSA and BF, the technique was tested on its sensitivity to distinguish binding from non-binding. The experimental binding curve of streptavidin-biotin was fitted with a theoretical model incorporating a 1:4 stoichiometry and ligand and receptor impurities. The binding constant and the fraction of receptor impurities were derived from the modeling. SW-FCCS was able to resolve the positive and negative control curves with a difference of 6 standard deviations only within a certain ligand to receptor concentration ratio. Limits for the measurement of dissociation constants in dependence on sample concentration, impurities, labeling ratios and spectral cross-talk were calculated based on a dimerization reaction. Fluorophore pairs, TMRSA/BF and QR/BF, were compared and it was demonstrated that the selection of bright dyes with minimum cross-talk was important for SW-FCCS to detect interactions with good resolution.

The theory and experiments for triple-color or multicolor SW-FCCS were described in chapter 5. The optical setup of multicolor SW-FCCS was outlined. This included two dichroic mirrors after the microscope tube lens, to separate the emission wavelengths into three detection pathways. To test for the binding of three components, BF (green), BPE (yellow) and AXSA (red), were simultaneously mixed and detected. Three pair-wise cross-correlations between green \times red, yellow \times red and green \times yellow channels were simultaneously collected at different ligand/receptor concentration ratios and their binding curves obtained. The theoretical model was extended to triple-color cross-correlations. Experimental binding curves were fitted with the theoretical model to determine the dissocia-

tion constants and its upper limits. Simulations of various binding schemes were performed with different K_{ds} and binding stoichiometry. An important application of SW-FCCS is to simultaneously detect multiple molecular interactions that can occur either kinetically or at binding equilibrium. With each protein having several different functions and binding partners, it has become valuable to concurrently probe molecular assemblies, such as in signalling transduction or protein-protein interactions in live cells.

The optical instrumentation and experimental realization of a prism-based fluorescence correlation spectrometer were described in chapter 6. The single wavelength excitation FCSpectrometer used a dispersive prism for the angular dispersion of the fluorescence emission wavelengths for detection. This spectrometer addressed the instrumentation complexity of multiplex detection, where a prism was used instead of a cascade of filters to separate the fluorescence signal into its respective wavelengths. An optical fiber was scanned along the image focal plane to select the emission wavelengths for detection and autocorrelation analysis. This was performed with RhG and AXSA dyes. Cross-correlation analysis was also demonstrated by aligning a fiber optic array for the detection of binding between two components, biotinylated RhG nanocontainers and AXSA. The lower cpm recorded for the spectrometer was due to several reasons: the narrower spectral range collected by the optic fiber and light losses due to scattering and reflection from the prism, lenses and bare fibers. Detection of wavelength ranges could be improved by using a diffraction grating for linear dispersion of emission light [87] or a continuous detection element such as a silicon photodiode array or a high-speed CCD camera. However, the prism-based setup was reported here to give a higher cpm as compared to the grating-based setup.

The theoretical and experimental results show that SW-FCCS can perform simultaneous auto- and cross-correlation measurements of up to three interacting components using only a single laser line for excitation. With the development of smaller long Stokes shift dyes with narrower emission spectra that are excitable

at single laser wavelength, SW-FCCS is a promising tool for the investigation of molecular dynamics and binding processes in multicolor systems. The potential of applying fluorescent proteins fused with target molecules brings the next step of SW-FCCS into live cell environment for the study of biomolecular interactions.

The outlook of SW-FCCS will advance in three main directions. First, developments of new fluorescent probes for the application in SW-FCCS. These probes not only need a high quantum yield and long-term photostability, they require large Stokes shifts that can be excited at single laser wavelength. It is also advantageous for dyes to have narrow emission spectra for minimal cross-talk as long wavelength dyes tend to have broader emission spectra. Possible fluorophores for use with SW-FCCS include quantum dots, which are commercially available in a wide range of emission wavelengths and can be excited at the same excitation wavelength. Although quantum dots have been used in fluorescence imaging of live cells and even whole organisms, single-molecule experiments with quantum dots have been limited due to its blinking characteristics, aggregation tendency and large size, which affects the mobility (hence possibly function) of the target molecule [104]. These factors will have to be taken into account when applied to single-molecule detection. Nevertheless because of its intense brightness, low photobleaching rate and tunable emission wavelengths with broad adsorption spectra, quantum dots prove to be a promising fluorescent probe for multicolor detection in cell biology. Tandem dyes are as well potential fluorescent probes for multicolor detection. The development of tandem dyes to conjugate different red-shifted cyanine and Alexa dyes to phycobiliproteins have led to a wide selection of long-wavelength dyes. However, tandem dyes have lower photostability than quantum dots, have higher photobleaching rates and an observed loss of FRET efficiency with time. In addition, the non-negligible emission signal from the phycobiliprotein (phycoerythrin at 550–600 nm) contributes to cross-talk and lower signal-to-noise ratio. Although it has been commonly used for cell sorting in flow cytometry, its large size could as well deter biophysicists from using tandem dyes

as labels for single molecule studies. In spite of this, with its high quantum yield and long-wavelength emission, tandem dyes have shown to be valuable probes for application in SW-FCCS. Recently, long Stokes shift organic probes with small molecular weight called Megastokes dyes [89] have been introduced with chemical modifications for labeling. Although these dyes have lower count rates compared with tandem dyes and quantum dots, they show promising applications in labeling biological molecules with its small size.

The second aspect of progress for SW-FCCS is the biological application. Having demonstrated the *in vitro* measurements of receptor-ligand binding, it is natural that the next step is the *in vivo* measurements of biomolecular interactions such as protein-protein interactions. Furthermore, fluorescent proteins such as GFP, YFP and mRFP have been shown to produce reasonable count rates when excited at 488 nm, hence it is possible to apply these FPs as fluorescent tags in SW-FCCS. Recently, the study of dimerization of epidermal growth factor receptor (EGFR) and Her2 that belongs to tyrosine kinase receptor family has been carried out with SW-FCCS in our laboratory. GFP and mRFP were fused to the inactivated transmembrane proteins, EGFR and ErbB2, in CHO cells and positive cross-correlations have confirmed the spontaneous formation of homo- and heterodimers. As the signal-to-noise ratio is lower in a live cell environment, it is important to set a laser power that reduces the photobleaching and autofluorescence background yet giving a good count rate. It was difficult to attain high count rates with mRFP at an excitation wavelength of 488 nm, far away from its excitation maximum. A new FP has been developed by Miyawaki and co-workers [162] called Keima that absorbs at 440 nm and emits at 620 nm. It was coupled with CFP and shown to work with SW-FCCS in live cells to detect proteolysis by caspase-3 and the association of calmodulin and calmodulin-dependent enzyme. This is an exciting area of SW-FCCS application to be unraveled with the development of more of such FPs for multicolor detection.

The third aspect of advancement of SW-FCCS is the optical instrumentation.

Using a dispersive element in the detection pathway for flexible selection of emission wavelengths, a grating or prism-based detection for SW-FCCS is only at its infancy. With the development of faster and more sensitive detectors for array elements such as CMOS or APD array [163, 164], the instrumentation of SW-FCCS could be further improved to utilize such detection devices. SW-FCCS could also be combined with fluorescence imaging or TIRF by introducing a fast-rate CCD camera to capture multicolor images as well as perform offline auto- and cross-correlations [161]. This now provides FCS with the spatial information of the entire image that was not possible before. Other fluorescence fluctuation techniques such as PCH and FIDA could as well be combined with SW-FCCS to reveal molecular properties not accessible by F(C)CS, such as molecular brightness. Therefore, the unison of SW-FCCS and single-molecule fluorescence techniques will pave the way for multiplexing technologies in biological applications.

Bibliography

- [1] Weiss, S., 1999. Fluorescence spectroscopy of single biomolecules. *Science* 283:1676–1682.
- [2] Hovius, R., P. Vallotton, T. Wohland, and H. Vogel, 2000. Fluorescence techniques: shedding light on ligand-receptor interactions. *Trends Pharmacol Sci* 21:266–73.
- [3] Hink, M. A., T. Bisseling, and A. J. W. G. Visser, 2002. Imaging protein-protein interactions in living cells. *Plant Mol Biol* 50:871–883.
- [4] Haustein, E., and P. Schuille, 2004. Single-molecule spectroscopic methods. *Curr Opin Struct Biol* 14:531–40.
- [5] Michalet, X., A. N. Kapanidis, T. Laurence, F. Pinaud, S. Doose, M. Pflughoeft, and S. Weiss, 2003. The power and prospects of fluorescence microscopies and spectroscopies. *Annu Rev Biophys Biomol Struct* 32:161–182.
- [6] Piehler, J., 2005. New methodologies for measuring protein interactions in vivo and in vitro. *Curr Opin Struct Biol* 15:4–14.
- [7] Day, R. N., and F. Schaufele, 2005. Imaging molecular interactions in living cells. *Mol Endocrinol* 19:1675–1686.
- [8] Förster, T., 1959. Transfer mechanisms of electronic excitation. *Discuss Faraday Soc* 27:7–17.
- [9] Stryer, L., 1967. Energy transfer: A spectroscopic ruler. *Proc Natl Acad Sci U S A* 58:719–726.
- [10] Sako, Y., S. Minoguchi, and T. Yanagida, 2000. Single-molecule imaging of EGFR signalling on the surface of living cells. *Nat Cell Biol* 2:168–172.
- [11] Kapanidis, A. N., E. Margeat, T. A. Laurence, S. Doose, S. O. Ho, J. Mukhopadhyay, E. Kortkhonjia, V. Mekler, R. H. Ebright, and S. Weiss, 2005. Retention of transcription initiation factor sigma70 in transcription elongation: single-molecule analysis. *Mol Cell* 20:347–56.
- [12] Margeat, E., A. N. Kapanidis, P. Tinnefeld, Y. Wang, J. Mukhopadhyay, R. H. Ebright, and S. Weiss, 2006. Direct observation of abortive initiation and promoter escape within single immobilized transcription complexes. *Biophys J* 90:1419–31.

- [13] Gadella, T. W. J., A. V. Hoek, and A. J. W. G. Visser, 1997. Construction and characterization of a frequency-domain fluorescence lifetime imaging microscopy system. *J Fluoresc* 7:35–43.
- [14] Sytsma, J., J. M. Vroom, C. J. de Grauw, and H. C. Gerritsen, 1998. Time gated fluorescence lifetime imaging and micro-volume spectroscopy using two-photon excitation. *J Microsc* 191:39–51.
- [15] Gadella, T. W. J., and T. M. Jovin, 1995. Oligomerization of epidermal growth factor receptors on a431 cells studied by time-resolved fluorescence imaging microscopy. a stereochemical model for tyrosine kinase receptor activation. *J Cell Biol* 129:1543–1558.
- [16] Clayton, A. H. A., F. Walker, S. G. Orchard, C. Henderson, D. Fuchs, J. Rothacker, E. C. Nice, and A. W. Burgess, 2005. Ligand-induced dimer-tetramer transition during the activation of the cell surface epidermal growth factor receptor—a multidimensional microscopy analysis. *J Biol Chem* 280:30392–30399.
- [17] Orden, A. V., K. Fogarty, and J. Jung, 2004. Fluorescence fluctuation spectroscopy: A coming of age story. *Appl Spect* 58:122A–137A.
- [18] Chen, Y., J. D. Muller, P. T. So, and E. Gratton, 1999. The photon counting histogram in fluorescence fluctuation spectroscopy. *Biophys J* 77:553–67.
- [19] Kask, P., K. Palo, D. Ullmann, and K. Gall, 1999. Fluorescence-intensity distribution analysis and its application in biomolecular detection technology. *Proc Natl Acad Sci U S A* 96:13756–61.
- [20] Haupts, U., M. Rüdiger, S. Ashman, S. Tuconi, R. Bingham, C. Wharton, J. Hutchinson, C. Carey, K. J. Moore, and A. J. Pope, 2003. Single-molecule detection technologies in miniaturized high-throughput screening: Fluorescence intensity distribution analysis. *J Biomol Screen* 8:19–33.
- [21] Jager, S., L. Brand, and C. Eggeling, 2003. New fluorescence techniques for high-throughput drug discovery. *Curr Pharm Biotechnol* 4:463–76.
- [22] Eggeling, C., L. Brand, D. Ullmann, and S. Jager, 2003. Highly sensitive fluorescence detection technology currently available for HTS. *Drug Discov Today* 8:632–41.
- [23] Chen, Y., J. D. Muller, S. Y. Tetin, J. D. Tyner, and E. Gratton, 2000. Probing ligand protein binding equilibria with fluorescence fluctuation spectroscopy. *Biophys J* 79:1074–84.
- [24] Chen, Y., L.-N. Wei, and J. D. Muller, 2003. Probing protein oligomerization in living cells with fluorescence fluctuation spectroscopy. *Proc Natl Acad Sci U S A* 100:15492–7.
- [25] Kask, P., K. Palo, N. Fay, L. Brand, U. Mets, D. Ullmann, J. Jungmann, J. Pschorr, and K. Gall, 2000. Two-dimensional fluorescence intensity distribution analysis: theory and applications. *Biophys J* 78:1703–13.

- [26] Chen, Y., M. Tekmen, L. Hillesheim, J. Skinner, B. Wu, and J. D. Muller, 2005. Dual-color photon-counting histogram. *Biophys J* 88:2177–92.
- [27] Palo, K., U. Mets, S. Jager, P. Kask, and K. Gall, 2000. Fluorescence intensity multiple distributions analysis: concurrent determination of diffusion times and molecular brightness. *Biophys J* 79:2858–66.
- [28] Palo, K., L. Brand, C. Eggeling, S. Jager, P. Kask, and K. Gall, 2002. Fluorescence intensity and lifetime distribution analysis: toward higher accuracy in fluorescence fluctuation spectroscopy. *Biophys J* 83:605–18.
- [29] Laurence, T. A., A. N. Kapanidis, X. Kong, D. S. Chemla, and S. Weiss, 2004. Photon arrival-time interval distribution (PAID): A novel tool for analyzing molecular interactions. *J Phys Chem B* 108:3051–3067.
- [30] Magde, D., E. L. Elson, and W. W. Webb, 1972. Thermodynamic fluctuations in a reacting system: Measurements by fluorescence correlation spectroscopy. *Phys Rev Lett* 29:705–708.
- [31] Elson, E. L., and M. Magde, 1974. Fluorescence correlation spectroscopy. i. conceptual basis and theory. *Biopolymers* 13:1–27.
- [32] Magde, D., E. L. Elson, and W. W. Webb, 1974. Fluorescence correlation spectroscopy. II. An experimental realization. *Biopolymers* 13:29–61.
- [33] Koppel, D. E., 1974. Statistical accuracy in fluorescence correlation spectroscopy. *Phys Rev A* 10:1938–1945.
- [34] Koppel, D. E., D. Axelrod, J. Schlessinger, E. L. Elson, and W. W. Webb, 1976. Dynamics of fluorescence marker concentration as a probe of mobility. *Biophys J* 16:1315–29.
- [35] Qian, H., and E. Elson, 1991. Analysis of confocal laser-microscope optics for 3-d fluorescence correlation spectroscopy. *Appl Opt* 30:1185–1195.
- [36] Rigler, R., Ü. Mets, J. Widengren, and P. Kask, 1993. Fluorescence correlation spectroscopy with high count rate and low background - analysis of translational diffusion. *Eur Biophys J* 22:169–175.
- [37] Thompson, N. L., 1991. Fluorescence Correlation Spectroscopy, Plenum Press, New York, 337–378.
- [38] Ehrenberg, M., and R. Rigler, 1974. Rotational brownian motion and fluorescence intensity fluctuations. *Chem Phys* 4:390–401.
- [39] Aragon, S. R., and R. Pecora, 1975. Fluorescence correlation spectroscopy and brownian rotational diffusion. *Biopolymers* 14:119–138.
- [40] Kask, P., P. Piksarv, Ü. Mets, and E. Lippmaa, 1987. Fluorescence correlation spectroscopy in the nanaosecond time range: Rotational diffusion of bovin carbonic anhydrase. *Eur. Biophys. J.* 14:257–261.

- [41] Kask, P., P. Piksarv, M. Pooga, Ü. Mets, and E. Lippmaa, 1988. Separation of the rotational contribution in fluorescence correlation measurements. *Biophys. J.* 55:213–220.
- [42] Gösch, M., H. Blom, J. Holm, T. Heino, and R. Rigler, 2000. Hydrodynamic flow profiling in microchannel structures by single molecule fluorescence correlation spectroscopy. *Anal Chem* 72:3260–5.
- [43] Petersen, N., and E. Elson, 1986. Measurements of diffusion and chemical kinetics by fluorescence photobleaching recovery fluorescence correlation spectroscopy. *Meth. Enzymol.* 130:454–484.
- [44] Widengren, J., and R. Rigler, 1998. Fluorescence correlation spectroscopy as a tool to investigate chemical reactions in solutions and on cell surfaces. *Cell Mol Biol* 44:857–79.
- [45] Rauer, B., E. Neumann, J. Widengren, and R. Rigler, 1996. Fluorescence correlation spectrometry of interaction kinetics of tetramethylrhodamine alpha-bungarotoxin with torpedo californica acetylcholine receptor. *Biophys Chem* 58:3–12.
- [46] Craenenbroeck, E. V., and Y. Engelborghs, 1999. Quantitative characterization of the binding of fluorescently labeled colchicine to tubulin in vitro using fluorescence correlation spectroscopy. *Biochemistry* 38:5082–8.
- [47] Wohland, T., K. Friedrich, R. Hovius, and H. Vogel, 1999. Study of ligand-receptor interactions by fluorescence correlation spectroscopy with different fluorophores: evidence that the homopentameric 5-hydroxytryptamine type 3As receptor binds only one ligand. *Biochemistry* 38:8671–81.
- [48] Edman, L., Z. Földes-Papp, S. Wennmalm, and R. Rigler, 1999. The fluctuating enzyme: A single molecule approach. *Chem Phys* 247:11–22.
- [49] Widengren, J., and P. Schwille, 2000. Characterization of photoinduced isomerization and back-isomerization of the cyanine dye cy5 by fluorescence correlation spectroscopy. *J Phys Chem* 104:6416–6428.
- [50] Haupts, U., S. Maiti, P. Schwille, and W. W. Webb, 1998. Dynamics of fluorescence fluctuations in green fluorescent protein observed by fluorescence correlation spectroscopy. *Proc Natl Acad Sci U S A* 95:13573–8.
- [51] Schwille, P., S. Kummer, A. A. Heikal, W. E. Moerner, and W. W. Webb, 2000. Fluorescence correlation spectroscopy reveals fast optical excitation-driven intramolecular dynamics of yellow fluorescent proteins. *Proc Natl Acad Sci U S A* 97:151–6.
- [52] Llopis, J., J. M. McCaffery, A. Miyawaki, M. G. Farquhar, and R. Y. Tsien, 1998. Measurement of cytosolic, mitochondrial and golgi pH in single living cells with green fluorescent proteins. *Proc Natl Acad Sci USA* 95:6803–6808.
- [53] Meseth, U., T. Wohland, R. Rigler, and H. Vogel, 1999. Resolution of fluorescence correlation measurements. *Biophys J* 76:1619–31.

- [54] Atkins, P. W., and J. D. Paula, 2001. *Physical Chemistry*. W H Freeman, New York, 7th edition.
- [55] Kam, Z., and R. Rigler, 1982. Cross-correlation laser scattering. *Biophys J* 39:7–13.
- [56] Ricka, J., and T. Binkert, 1989. Direct measurement of a distinct correlation-function by fluorescence cross-correlation. *Phys. Rev. A* 39:2646–2652.
- [57] Brinkmeier, M., K. Dorre, J. Stephan, and M. Eigen, 1999. Two beam cross correlation: A method to characterize transport phenomena in micrometer-sized structures. *Anal. Chem.* 71:609–616.
- [58] Eigen, M., and R. Rigler, 1994. Sorting single molecules: Applications to diagnostics and evolutionary biotechnology. *Proc Natl Acad Sci USA* 91:5740–5747.
- [59] Schwille, P., F. J. Meyer-Almes, and R. Rigler, 1997. Dual-color fluorescence cross-correlation spectroscopy for multicomponent diffusional analysis in solution. *Biophys J* 72:1878–86.
- [60] Schwille, P., 2001. *Cross-Correlation Analysis in FCS*, Springer, 360–378.
- [61] Rigler, R., Z. Foldes-Papp, F. J. Meyer-Almes, C. Sammet, M. Volcker, and A. Schnetz, 1998. Fluorescence cross-correlation: a new concept for polymerase chain reaction. *J Biotechnol* 63:97–109.
- [62] Foldes-Papp, Z., and R. Rigler, 2001. Quantitative two-color fluorescence cross-correlation spectroscopy in the analysis of polymerase chain reaction. *Biol Chem* 382:473–8.
- [63] Kettling, U., A. Koltermann, P. Schwille, and M. Eigen, 1998. Real-time enzyme kinetics monitored by dual-color fluorescence cross-correlation spectroscopy. *Proc Natl Acad Sci U S A* 95:1416–20.
- [64] Rarbach, M., U. Kettling, A. Koltermann, and M. Eigen, 2001. Dual-color fluorescence cross-correlation spectroscopy for monitoring the kinetics of enzyme-catalyzed reactions. *Methods* 24:104–16.
- [65] Rippe, K., 2000. Simultaneous binding of two DNA duplexes to the NtrC-enhancer complex studied by two-color fluorescence cross-correlation spectroscopy. *Biochemistry* 39:2131–9.
- [66] Bacia, K., and P. Schwille, 2003. A dynamic view of cellular processes by in vivo fluorescence auto- and cross-correlation spectroscopy. *Methods* 29:74–85.
- [67] Bacia, K., S. A. Kim, and P. Schwille, 2006. Fluorescence cross-correlation spectroscopy in living cells. *Nat Methods* 3:83–9.
- [68] Bacia, K., I. V. Majoul, and P. Schwille, 2002. Probing the endocytic pathway in live cells using dual-color fluorescence cross-correlation analysis. *Biophys J* 83:1184–93.

- [69] Saito, K., I. Wada, M. Tamura, and M. Kinjo, 2004. Direct detection of caspase-3 activation in single live cells by cross-correlation analysis. *Biochem Biophys Res Commun* 324:849–54.
- [70] Baudendistel, N., G. Muller, W. Waldeck, P. Angel, and J. Langowski, 2005. Two-hybrid fluorescence cross-correlation spectroscopy detects protein-protein interactions in vivo. *Chemphyschem* 6:984–90.
- [71] Petersen, N. O., P. L. Hoddellius, P. W. Wiseman, O. Seger, and K. E. Magnusson, 1993. Quantitation of membrane receptor distributions by image correlation spectroscopy: concept and application. *Biophys J* 65:1135–46.
- [72] Wiseman, P. W., J. A. Squier, M. H. Ellisman, and K. R. Wilson, 2000. Two-photon image correlation spectroscopy and image cross-correlation spectroscopy. *J Microsc* 200:14–25.
- [73] Costantino, S., J. W. D. Comeau, D. L. Kolin, and P. W. Wiseman, 2005. Accuracy and dynamic range of spatial image correlation and cross-correlation spectroscopy. *Biophys J* 89:1251–60.
- [74] Petersen, N. O., C. Brown, A. Kaminski, J. Rocheleau, M. Srivastava, and P. W. Wiseman, 1998. Analysis of membrane protein cluster densities and sizes in situ by image correlation spectroscopy. *Faraday Discuss* NIL:289–305; discussion 331–43.
- [75] Wiseman, P. W., C. M. Brown, D. J. Webb, B. Hebert, N. L. Johnson, J. A. Squier, M. H. Ellisman, and A. F. Horwitz, 2004. Spatial mapping of integrin interactions and dynamics during cell migration by image correlation microscopy. *J Cell Sci* 117:5521–34.
- [76] Digman, M. A., C. M. Brown, P. Sengupta, P. W. Wiseman, A. R. Horwitz, and E. Gratton, 2005. Measuring fast dynamics in solutions and cells with a laser scanning microscope. *Biophys J* 89:1317–27.
- [77] Kassies, R., A. Lenferink, I. Segers-Nolten, and C. Otto, 2005. Prism-based excitation wavelength selection for multicolor fluorescence coincidence measurements. *Appl Opt* 44:893–7.
- [78] Winkler, T., U. Kettling, A. Koltermann, and M. Eigen, 1999. Confocal fluorescence coincidence analysis: An approach to ultra high-throughput screening. *Proc. Natl. Acad. Sci. U S A* 96:1375–1378.
- [79] Schwille, P., U. Haupts, S. Maiti, and W. W. Webb, 1999. Molecular dynamics in living cells observed by fluorescence correlation spectroscopy with one- and two-photon excitation. *Biophys J* 77:2251–65.
- [80] Berland, K. M., P. T. C. So, and E. Gratton, 1995. Two-photon fluorescence correlation spectroscopy: Method and application to the intracellular environment. *Biophys. J.* 68:694–701.
- [81] Kim, S. A., K. G. Heinze, K. Bacia, M. N. Waxham, and P. Schwille, 2005. Two-photon cross-correlation analysis of intracellular reactions with variable stoichiometry. *Biophys J* 88:4319–36.

- [82] Kim, S. A., K. G. Heinze, M. N. Waxham, and P. Schwille, 2004. Intracellular calmodulin availability accessed with two-photon cross-correlation. *Proc Natl Acad Sci U S A* 101:105–10.
- [83] Heinze, K. G., M. Jahnz, and P. Schwille, 2004. Triple-color coincidence analysis: one step further in following higher order molecular complex formation. *Biophys J* 86:506–16.
- [84] Muller, B. K., E. Zaychikov, C. Brauchle, and D. C. Lamb, 2005. Pulsed interleaved excitation. *Biophys J* 89:3508–22.
- [85] Thews, E., M. Gerken, R. Eckert, J. Zapfel, C. Tietz, and J. Wrachtrup, 2005. Cross talk free fluorescence cross correlation spectroscopy in live cells. *Biophys J* 89:2069–76.
- [86] Heinze, K. G., A. Koltermann, and P. Schwille, 2000. Simultaneous two-photon excitation of distinct labels for dual-color fluorescence crosscorrelation analysis. *Proc Natl Acad Sci U S A* 97:10377–82.
- [87] Burkhardt, M., K. G. Heinze, and P. Schwille, 2005. Four-color fluorescence correlation spectroscopy realized in a grating-based detection platform. *Opt Lett* 30:2266–8.
- [88] Weisshart, K., V. Jungel, and S. J. Briddon, 2004. The LSM 510 META - ConfoCor 2 system: an integrated imaging and spectroscopic platform for single-molecule detection. *Curr Pharm Biotechnol* 5:135–54.
- [89] Dyomics GmbH. www.dyomics.com.
- [90] Lacoste, T. D., X. Michalet, F. Pinaud, D. S. Chemla, A. P. Alivastos, and S. Weiss, 2000. Ultrahigh-resolution multicolor colocalization of single fluorescent probes. *Proc. Natl. Acad. Sci. USA* 97:9461–9466.
- [91] Quantum Dot, 2002. Qdot Streptavidin Conjugate User Manual. Quantum Dot, Hayward, C.A.
- [92] Bruchez, M., M. Moronne, P. Gin, S. Weiss, and A. P. Alivisatos, 1998. Semiconductor nanocrystals as fluorescent biological labels. *Science* 281:2013–2016.
- [93] Alivisatos, A. P., 1996. Semiconductor clusters, nanocrystals and quantum dots. *Science* 271:933–937.
- [94] Wu, X., H. Liu, J. Liu, K. N. Haley, J. A. Treadway, J. P. Larson, N. Ge, F. Peale, and M. P. Bruchez, 2002. Immunofluorescent labeling of cancer marker her2 and other cellular targets with semiconductor quantum dots. *Nat. Biotechnol.* 21:41–46.
- [95] Larson, D. R., W. R. Zipfel, R. M. Williams, S. W. Clark, M. P. Bruchez, F. W. Wise, and W. W. Webb, 2003. Water-soluble quantum dots for multiphoton fluorescence imaging in vivo. *Science* 300:1434–1436.

- [96] Nirmal, M., B. O. Dabbousi, M. G. Bawendi, J. J. Macklin, J. K. Trautman, T. D. Harris, and L. E. Brus, 1996. Fluorescence intermittency in single cadmium selenide nanocrystals. *Nature* 383:802–804.
- [97] Grecco, H. E., K. A. Lidke, R. Heintzmann, D. S. Lidke, C. Spagnuolo, O. E. Martinez, E. A. Jares-Erijman, and T. M. Jovin, 2004. Ensemble and single particle photophysical properties (two-photon excitation, anisotropy, FRET, lifetime, spectral conversion) of commercial quantum dots in solution and in live cells. *Micr. Res. and Tech.* 65:169–179.
- [98] Zhang, P., L. Li, C. Dong, H. Qian, and J. Ren, 2005. Sizes of water-soluble luminescent quantum dots measured by fluorescence correlation spectroscopy. *Analytica Chimica Acta* 546:46–51.
- [99] Korlach, J., T. Baumgart, W. W. Webb, and G. W. Feigenson, 2005. Detection of motional heterogeneities in lipid bilayer membranes by dual probe fluorescence correlation spectroscopy. *Biochim Biophys Acta* 1668:158–163.
- [100] Stavis, S. M., J. B. Edel, K. T. Samiee, and H. G. Craighead, 2005. Single molecule studies of quantum dot conjugates in a submicrometer fluidic channel. *Lab Chip* 5:337–43.
- [101] Swift, J. L., R. Heuff, and D. T. Cramb, 2006. A two-photon excitation fluorescence cross-correlation assay for a model ligand-receptor binding system using quantum dots. *Biophys. J.* 90:1396–1410.
- [102] Michalet, X., F. F. Pinaud, L. A. Bentolila, J. M. Tsay, S. Doose, J. J. Li, G. Sundaresan, A. M. Wu, S. S. Gambhir, and S. Weiss, 2005. Quantum dots for live cells, in vivo imaging, and diagnostics. *Science* 307:538–544.
- [103] Alivisatos, P., 2004. The use of quantum dots in biological detection. *Nat. Biotechnol.* 22:47–52.
- [104] Alivisatos, A. P., W. Gu, and C. Larabell, 2005. Quantum dots as cellular probes. *Annu. Rev. Biomed. Eng.* 7:55–76.
- [105] Kronick, M. N., 1986. The use of phycobiliproteins as fluorescent labels in immunoassay. *J Immunol Methods* 92:1–13.
- [106] Glazer, A. N., and L. Stryer, 1983. Fluorescent tandem phycobiliprotein conjugates. Emission wavelength shifting by energy transfer. *Biophys J* 43:383–6.
- [107] Tjioe, I., T. Legerton, J. Wegstein, L. A. Herzenberg, and M. Roederer, 2001. Phycoerythrin-allophycocyanin: a resonance energy transfer fluorochrome for immunofluorescence. *Cytometry* 44:24–9.
- [108] Waggoner, A. S., L. A. Ernst, C. H. Chen, and D. J. Rechtenwald, 1993. PE-CY5. A new fluorescent antibody label for three-color flow cytometry with a single laser. *Ann N Y Acad Sci* 677:185–93.

- [109] Berlier, J. E., A. Rothe, G. Buller, J. Bradford, D. R. Gray, B. J. Filanoski, W. G. Telford, S. Yue, J. Liu, C.-Y. Cheung, W. Chang, J. D. Hirsch, J. M. Beechem, R. P. Haugland, and R. P. Haugland, 2003. Quantitative comparison of long-wavelength Alexa Fluor dyes to Cy dyes: fluorescence of the dyes and their bioconjugates. *J Histochem Cytochem* 51:1699–712.
- [110] Viksman, M. Y., M. C. Liu, R. P. Schleimer, and B. S. Bochner, 1994. Application of a flow cytometric method using autofluorescence and a tandem fluorescent dye to analyze human alveolar macrophage surface markers. *J Immunol Methods* 172:17–24.
- [111] Lansdorp, P. M., C. Smith, M. Safford, L. W. Terstappen, and T. E. Thomas, 1991. Single laser three color immunofluorescence staining procedures based on energy transfer between phycoerythrin and cyanine 5. *Cytometry* 12:723–30.
- [112] Herzenberg, L. A., D. Parks, B. Sahaf, O. Perez, M. Roederer, and L. A. Herzenberg, 2002. The history and future of the fluorescence activated cell sorter and flow cytometry: a view from Stanford. *Clin Chem* 48:1819–27.
- [113] Szollosi, J., S. Damjanovich, and L. Matyus, 1998. Application of fluorescence resonance energy transfer in the clinical laboratory: routine and research. *Cytometry* 34:159–79.
- [114] Green, N. M., 1975. Avidin, Academic Press, New York, volume 29, 85–133.
- [115] Chaiet, L., and F. J. Wolf, 1964. The properties of streptavidin, a biotin-binding protein produced by streptomycetes. *Arch Biochem Biophys* 106:1–5.
- [116] Weber, P. C., D. H. Ohlendorf, J. J. Wendoloski, and F. R. Salemme, 1989. Structural origins of high-affinity biotin binding to streptavidin. *Science* 243:85–88.
- [117] Stayton, P. S., S. Freitag, L. A. Klumb, A. Chilkoti, V. Chu, J. E. Penzotti, R. To, D. Hyre, I. L. Trong, T. P. Lybrand, and R. E. Stenkamp, 1999. Streptavidin-biotin binding energetics. *Biomol Eng* 16:39–44.
- [118] Wilchek, M., and E. A. Bayer, 1988. The avidin-biotin complex in bioanalytical applications. *Anal Biochem* 171:1–32.
- [119] Wilchek, M., and E. A. Bayer, 1989. Avidin-biotin technology ten years on: Has it lived up to its expectations? *TIBS* 14:408–412.
- [120] Wilchek, M., and E. A. Bayer, 1999. Foreword and introduction to the book (strept)avidin-biotin system. *Biomol Eng* 16:1–4.
- [121] Wilchek, M., E. A. Bayer, and O. Livnah, 2006. Essentials of biorecognition: The (strept)avidin-biotin system as a model for protein-protein and protein-ligand interaction. *Immunol Lett* 103:27.

- [122] Gruber, H. J., G. Kada, M. Marek, and K. Kaiser, 1998. Accurate titration of avidin and streptavidin with biotin-fluorophore conjugates in complex, colored biofluids. *Biochim Biophys Acta* 1381:203–212.
- [123] Kada, G., H. Falk, and H. J. Gruber, 1999. Accurate measurement of avidin and streptavidin in crude biofluids with a new, optimized biotin-fluorescein conjugate. *Biochim Biophys Acta* 1427:33–43.
- [124] Kada, G., K. Kaiser, H. Falk, and H. J. Gruber, 1999. Rapid estimation of avidin and streptavidin by fluorescence quenching or fluorescence polarization. *Biochim Biophys Acta* 1427:44–48.
- [125] Widengren, J., R. Rigler, and Ü. Mets, 1994. Triplet-state monitoring by fluorescence correlation spectroscopy. *J. Fluorescence* 4:255–264.
- [126] Widengren, J., Ü. Mets, and R. Rigler, 1995. Fluorescence correlation spectroscopy of triplet states in solution: A theoretical and experimental study. *J Phys Chem* 99:13368–13379.
- [127] Wilson, T., and C. Sheppard, 1984. Theory and Practice of Scanning Optical Microscopy. Academic Press London, London.
- [128] Magde, D., W. W. Webb, and E. L. Elson, 1978. Fluorescence correlation spectroscopy. III. uniform translation and laminar flow. *Biopolymers* 17:361–376.
- [129] Gregor, I., D. Patra, and J. Enderlein, 2005. Optical saturation in fluorescence correlation spectroscopy under continuous-wave and pulsed excitation. *Chemphyschem* 6:164–70.
- [130] Lakowicz, J. R., 1999. Principles of Fluorescence Spectroscopy. Kluwer Academic/Plenum, New York, 2nd edition.
- [131] Bevington, P., and D. Robinson, 1992. Data Reduction and Error Analysis for the Physical Sciences. McGraw Hill, New York, 2nd edition.
- [132] Weidemann, T., M. Wachsmuth, M. Tewes, K. Rippe, and J. Langowski, 2002. Analysis of ligand binding by two-color fluorescence cross-correlation spectroscopy. *Single Mol* 1:49–61.
- [133] Thompson, N. L., A. M. Lieto, and N. W. Allen, 2002. Recent advances in fluorescence correlation spectroscopy. *Curr Opin Struct Biol* 12:634–41.
- [134] Hulme, E. C., 1992. Receptor-Ligand Interactions: A Practical Approach. IRL Press at Oxford University Press, Oxford.
- [135] Tuk, B., and M. F. V. Oostenbruggen, 1996. Solving inconsistencies in the analysis of receptor-ligand interactions. *Trends Pharmacol Sci* 17:403–409.
- [136] Aragón, S. R., and R. Pecora, 1976. Fluorescence correlation spectroscopy as a probe of molecular dynamics. *J Chem Phys* 64:1791–1803.

- [137] Schwille, P., 2001. Fluorescence correlation spectroscopy and its potential for intracellular applications. *Cell Biochem Biophys* 34:383–408.
- [138] Manders, E. M. M., F. J. Verbeek, and J. A. Aten, 1993. Measurement of co-localization of objects in dual-color confocal images. *J Microsc* 169:375–382.
- [139] Demandolx, D., and J. Davoust, 1997. Multicolor analysis and local image correlation in confocal microscopy. *J Microsc* 185:21–36.
- [140] Haustein, E., M. Jahnz, and P. Schwille, 2003. Triple FRET: a tool for studying long-range molecular interactions. *Chemphyschem* 4:745–8.
- [141] Widengren, J., U. Mets, and R. Rigler, 1999. Photodynamic properties of green fluorescent proteins investigated by fluorescence correlation spectroscopy. *Chem Phys* 250:171–186.
- [142] MacColl, R., L. E. Eisele, E. C. Williams, and S. S. Bowser, 1996. The discovery of a novel r-phycoerythrin from an antarctic red algae. *J Biol Chem* 271:17157–17160.
- [143] Berland, K. M., 2004. Detection of specific DNA sequences using dual-color two-photon fluorescence correlation spectroscopy. *J Biotechnol* 108:127–36.
- [144] Karlin, A., 1967. On the application of "a plausible model" of allosteric proteins to the receptor for acetylcholine. *J Theoret Biol* 16:306–320.
- [145] Frederix, P. L. T. M., M. A. H. Asselbergs, W. G. J. H. M. V. Sark, D. J. V. D. Heuvel, W. Hamelink, E. L. D. Beer, and H. C. Gerritsen, 2001. High sensitivity spectrograph for use in fluorescence microscopy. *Appl Spectrosc* 55:1005–1012.
- [146] Bigelow, C. E., D. L. Conover, and T. H. Foster, 2003. Confocal fluorescence spectroscopy and anisotropy imaging system. *Opt Lett* 28:695–7.
- [147] Trepte, O., 1995. An optical spectrometer for a confocal scanning laser microscope. *Scanning* 17:171–174.
- [148] Suzuki, Y., T. Tani, K. Sutoh, and S. Kamimura, 2002. Imaging of the fluorescence spectrum of a single fluorescent molecule by prism-based spectroscopy. *FEBS Lett* 512:235–9.
- [149] Hanley, Q. S., P. I. Murray, and T. S. Forde, 2006. Microspectroscopic fluorescence analysis with prism-based imaging spectrometers: Review and current studies. *Cytometry A* .
- [150] Dickinson, M. E., G. Bearman, S. Tille, R. Lansford, and S. E. Fraser, 2001. Multi-spectral imaging and linear unmixing add a whole new dimension to laser scanning fluorescence microscopy. *Biotechniques* 31:1272, 1274–6, 1278.
- [151] Hiraoka, Y., T. Shimi, and T. Haraguchi, 2002. Multispectral imaging fluorescence microscopy for living cells. *Cell Struct Funct* 27:367–374.

- [152] Zimmermann, T., J. Rietdorf, A. Girod, V. Georget, and R. Pepperkok, 2002. Spectral imaging and linear un-mixing enables improved FRET efficiency with a novel GFP2-YFP FRET pair. *FEBS Lett* 531:245–9.
- [153] Zimmermann, T., J. Rietdorf, and R. Pepperkok, 2003. Spectral imaging and its applications in live cell microscopy. *FEBS Lett* 546:87–92.
- [154] Sawyer, R. A., 1951. Experimental Spectroscopy. Prentice-Hall, New York, 2nd edition.
- [155] Williams, C. S., and O. A. Becklund, 1972. Optics: A Short Course for Engineers and Scientists. Wiley-Interscience, New York.
- [156] Born, M., and E. Wolf, 1999. Principles of Optics : Electromagnetic Theory of Propagation, Interference and Diffraction of Light. Cambridge University Press, Cambridge, 7th edition.
- [157] Bach, H., and N. Neuroth, editors, 1995. The Properties of Optical Glass. Springer-Verlag, Berlin and New York.
- [158] SCHOTT. <http://www.schott.com>.
- [159] Rigler, P., and W. Meier, 2006. Encapsulation of fluorescent molecules by functionalized polymeric nanocontainers: investigation by confocal fluorescence imaging and fluorescence correlation spectroscopy. *J Am Chem Soc* 128:367–73.
- [160] Nardin, C., T. Hirt, J. Leukel, and W. Meier, 2000. Polymerized ABA triblock copolymer vesicles. *Langmuir* 16:1035–1041.
- [161] Kannan, B., J. Y. Har, P. Liu, I. Maruyama, J. L. Ding, and T. Wohland, 2006. Electron Multiplying Charge-Coupled Device Camera Based Fluorescence Correlation Spectroscopy. *Anal Chem* 78:3444–3451.
- [162] Kogure, T., S. Karasawa, T. Araki, K. Saito, M. Kinjo, and A. Miyawaki, 2006. A fluorescent variant of a protein from the stony coral *Montipora* facilitates dual-color single-laser fluorescence cross-correlation spectroscopy. *Nat Biotechnol* 24:577–81.
- [163] Gösch, M., A. Serov, T. Anhut, T. Lasser, A. Rochas, P.-A. Besse, R. S. Popovic, H. Blom, and R. Rigler, 2004. Parallel single molecule detection with a fully integrated single-photon 2x2 CMOS detector array. *J Biomed Opt* 9:913–21.
- [164] Gösch, M., H. Blom, S. Anderegg, K. Korn, P. Thyberg, M. Wells, T. Lasser, R. Rigler, A. Magnusson, and S. Hard, 2005. Parallel dual-color fluorescence cross-correlation spectroscopy using diffractive optical elements. *J Biomed Opt* 10:054008.